UNIVERSITÀ DI PARMA

UNIVERSITA' DEGLI STUDI DI PARMA

DOTTORATO DI RICERCA IN

Scienze e Tecnologie dei Materiali

CICLO XXXIV

Functional hybrid organic-inorganic formate-based frameworks

Coordinatore:

Prof. Enrico Dalcanale

Tutore:

Prof. Lara Righi

Co-tutore:

Dr. Fabio Orlandi

Dottorando: Valentina Vit

Anni Accademici 2018/2019 – 2020/2021

“I’m an outsider,

Outsider of everything”

(The Ramones)

“Stepped out of the line,

like a sheep runs from the herd,

marching out of time,

to my own beat, now,

the only way I know.

‘Cause I wanna be the minority”

(Green Day)

INTRODUCTION

Hybrid organic-inorganic materials have attached much interest till past decades due to their chemical variability, structural diversity, and intriguing physical properties. One of the most important family of hybrid materials is the formate one, which have been deeply studied from the physical point of view for their interesting magnetic and ferroelectric properties. On the other hand, not much has been told on their chemical behaviour. Moreover, the known information on these materials refers only to single crystal analysis and not powders, making more difficult their inclusion for future applications.

This work is focused on two main formate compounds: the ammonium and hydrazinium family, which have been studied from the chemical and physical point of view using different techniques that require polycrystalline samples.

This thesis will be organized according to the following structure:

In *Chapter 1* we will begin introducing the big family of the hybrid materials then a focus on the formate compounds is discussed. In this section it will be illustrated the synthesis already known to obtain these compounds and their physical properties.

In *Chapter 2* it will be discussed the ammonium formate compounds, with a detailed overview on the literature present on this family. Then, a focus of the synthesis of polycrystalline materials will be presented. Hence, it will be detailed the successful synthesis with mechanochemical approach, applied for the first time to the formate family.

In *Chapter 3* it will be presented the hydrazine formate compounds starting from the description of the chiral and perovskite structures present in literature and their physical properties. Subsequently, we present our results related to the synthesis of the pure compounds. We studied the structural transformation between the chiral and perovskite phases performing also diffraction experiments at Elettra synchrotron of Trieste. Moreover, it will illustrated the results related the synthesis of bimetallic formate compounds and the magnetic and ferroelectric characterization on the chiral and perovskite polymorphs.

In *Chapter 4* the ionic conduction measurements will be presented. In the first section we will proceed illustrating the theory on the ionic conduction and the state of the art related to metal organic frameworks showing ionic conductivity. Our

results demonstrate, for the first time, the ionic conduction behaviour of the formate-based materials and its dependence on relative humidity conditions.

In *Chapter 6* the results related to the mechanosynthesis of Cs-based formate compound will be discussed. The experimental results on the ionic conductivity measurements aimed to disclose the behaviour of the ammine based compounds are summarized. Thus the it will be discussed a low temperature transition never reported in literature and probably related to a modulation in the structure.

In *Chapter 7* the experimental methods used to synthesize the samples and the major physical analysis techniques used in this work will be presented. Moreover, the details of the refinements performed on the samples are illustrated.

INDEX OF CONTENTS

1 STATE OF ART

1.1 Introduction to Hybrid Organic-inorganic Perovskites

Hybrid Organic-Inorganic perovskite materials derive from the inorganic perovskites family that took the name from the mineral $CaTiO_3$, the first material adopting this structure. The general formula of these compounds can be expressed as ABX_3, where A and B are metal cations with different ionic radii, instead X is an anion. The structure is formed by corner sharing BX_6 octahedra that form cavities in which the A cation is placed (Figure 1.1-1) [1].

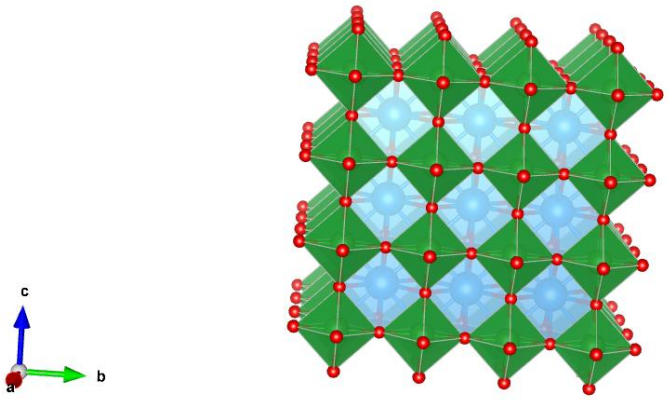

Figure 1.1-1: crystal structure of the $CaTiO_3$ perovskite; in green octahedra indicate the titanium coordination polyhedral, in blue the calcium one and the red sphere represent oxygen.

Perovskites are largely used for their physical properties that have important industrial applications [2, 3]. One of the most studied inorganic perovskites is $BaTiO_3$ which has been discovered during the 1940s to be a ferroelectric material and started a new era in which perovskites compounds have been used in electronics devices [4]. In the case of $BaTiO_3$ the Ti^{4+} ion moves from the centre of TiO_6 octahedra and induces a spontaneous polarization. During the years many others ferroelectric perovskite materials have been discovered such as $PbZr_xTi_{1-x}O_3$ ($0 < x < 1$, PZT) [5]. Another important perovskite material is $BiFeO_3$, which exhibits ferroelectric and magnetic ordering at ambient condition, and it is used in spintronics applications [6].

The synthesis of polycrystalline perovskite oxides is usually performed by solid state reactions at high temperature. In some cases, the elevated temperature can cause the loss of some volatile reactants, e.g., PbO. In these cases, sol-gel, microwave, and hydrothermal synthesis can also be used to prepare these

compounds. Physical vapour deposition or pulsed laser deposition methods are used to obtain thin films of perovskites oxides, that could be integrated into silico circuits[2].

The perovskite structure is very versatile and can accommodate different ions with different ionic radii, opening the possibility to engineer the material properties. In this scenario the Hybrid Organic-Inorganic perovskite offer even more flexibility. In fact, the A- and/or the X-site can be occupied by organic ions or molecular bitopic linkers. Using such a variety of linkers, molecules, and ions the hybrid perovskites family includes a multitude of structures like azides, cyanides, halides, formate, borohydrides and hypophosphites [7]. Methylammonium lead iodide CH_3NH_3PbI ($MAPbI_3$) is an example of hybrid perovskite which has photovoltaic properties; in this case the A site is occupied by the methylammonium cation, the B site by lead and the X site by iodine [8] (Figure 1.1-2).

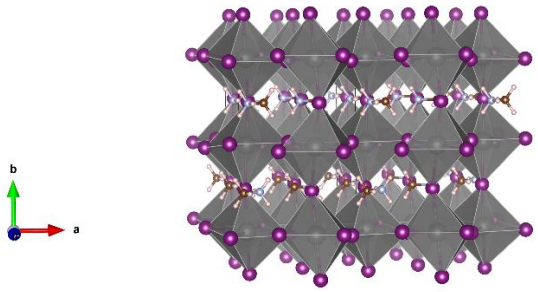

Figure 1.1-2: crystal structure of CH_3NH_3PbI.

The introduction of a bitopic organic linker in the X-site generates other variety of hybrid perovskites like metal-formate. Metal-dicyanamide. $[CH_3NH_3][Mn(HCOO)_3]$ is an example of a metal-formate hybrid perovskite, in which also the X site is substituted by an organic linker (Figure 1.1-3) [9]. The addition of an organic component gives to the structure a completely new electronic nature and flexibility to the framework, compared to the oxides. This is reflected in new functionalities for the materials that are not available with the classic perovskite oxides together with new physical properties and new strategies of synthesis.

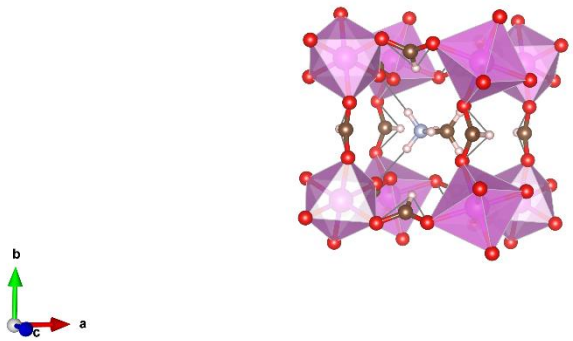

Figure 1.1-3: crystal structure of $[CH_3NH_3][Mn(HCOO)_3]$. The methylammonium cation is located inside the cavity formed by the MnO_6 octahedra.

The possible combinations of A-site cations and X-site linkers are various; the majority of the A-site cations that are used are monovalent amine, such as ammonium, methylammonium, hymidazolium and guanidinium cations, both linear and cyclic [7]. Nevertheless, also diamine cations are employed and few other organics cation like triphenylsufonium that is able to template dicyanamide (dca) perovskites (Figure 1.1-4) [10].

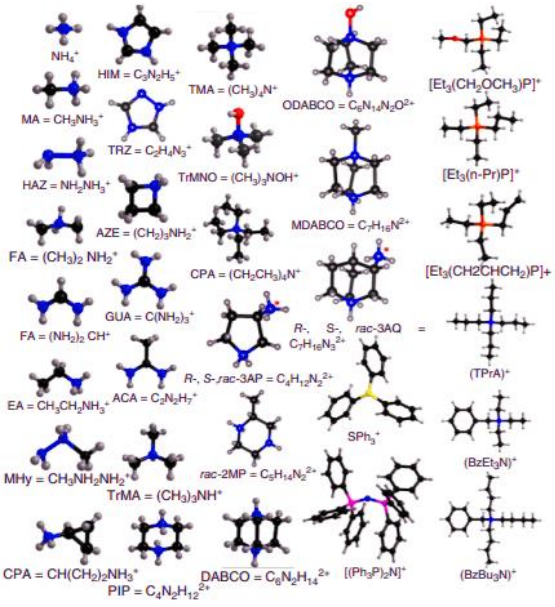

Figure1.1-4: list of the most used A-site organic cations. The picture has been taken from Ref 7.

Also the X-site linkers are usually monovalent, monoatomic, biatomic or multi-atomic groups like halide ion (Cl^-, Br^-, I^-), azide ion (N^{3-}), dicynametallate ($[Ag(CN)_2]^-$ or $[Au(CN)_2]^-$), cyanide ion (CN^-), borohydride ion (BH_4^-), formate ion ($HCOO^-$) or dicyanamide (dca) (Figure 1.1-5). Regarding the B-site, this is usually occupied by a divalent metal or a mix of monovalent/trivalent metal ions; monovalent ions are present if the A-site is occupied by a diamine cation.

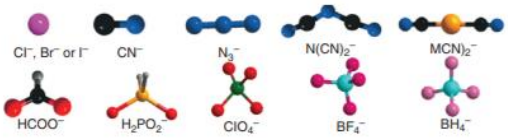

Figure 1.1-5: list of possible X-site molecule. The picture has been taken from Ref 7.

Generally, hybrid perovskites can belong to any of the seven-crystal system, due to the size and shape of the A-site cation. If the A-site is occupied by a high symmetry amine, the resulting perovskite will have high-symmetry space group. In most cases, at high temperature the A site molecule shows orientation disorder generally related to the difference between the A site and molecule point groups. As in the case of the inorganic perovskites, the composition influences the physical properties, for example halide perovskites have shown to possess optoelectrical, magnetic, ferroelectric, dielectric and multiferroic properties [7].

Even though the possibilities to build different hybrid structures are infinite, not all the matches between the building blocks are possible and, as for the inorganic perovskites, not all the ratio between the ionic sizes of the atoms/molecules are tolerated by the perovskite lattice. The range in which the structure is stable is determined by the Goldshmidt tolerance factor (t) [11]. In the case of the hybrid perovskite, the species involved are not spherical as the ions in the inorganic perovskites, so the t factor has been adjusted to the formula reported below [12]:

$$t = \frac{(r_{Aeff} + r_{Xeff})}{\sqrt{2}(r_B + 0.5h_{Xeff})}$$

r_B represents the radius of the B-site metal ion, r_{Xeff}, r_{Aeff} and h_{Xeff} are the effective radius of the X-site molecular group, the effective radius of the X-site molecular group and the height of the X-site molecular group respectively. The effective radius is calculated assuming free rotational freedom around the centre of mass and a rigid sphere model is applied to organic cations. Applying the formula to the hybrid perovskites, the obtained t values are in the 0.8 - 1.0 range, similar to what has been observed for the inorganic perovskites, indicating that this empiric rule can be

adopted. The tolerance factor can be, then, used to design new hybrid perovskites with the desired functionalities or to replace the lead-based perovskite for example by mixing mono- and trivalent metal ions leading the possibility to future industrial applications [13]. Despite the accuracy of the tolerance factor, this metric does not take in account the stability of the structure in terms of lattice energy, and special attention should be taken in using it to predict the stability of new compounds.

1.2 Hybrid Formate compounds

1.2.1 Synthesis of the different compounds

In the family of the formate hybrid perovskite the X-site is occupied by the formate molecule in its anion form $HCOO^-$; the use of a molecule as a linker, instead of a single ion (for example halide ions) allows to use larger cations in the A-site. In fact, in the halide hybrid perovskites the A-site is occupied by small molecules like methylammonium (MA) or formamidinium, instead the use of the formate gives the possibility to accommodate a wide range of ammine [9].

The formate anion is long ~ 4.5 Å and can bridge the metal sites in three possible ways: *syn-syn*, *syn-anti* and *anti-anti* (Figure 1.2.1-1) [9].

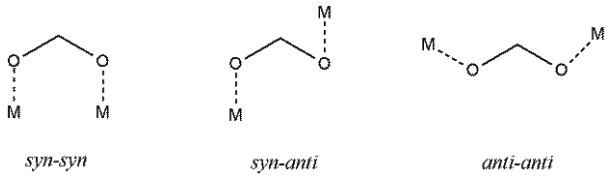

Figure 1.2.1-1: coordination mode of $HCOO^-$ anion.

In most of the hybrid perovskites the preferred coordination observed is *anti-anti*, but also there are also example with *syn-anti* and *syn-syn* [14]; the formate coordinates the metal with the two oxygens forming a MO_6 octahedra and cubic or pseudo-cubic cavities are formed in which the ammine cations are located. The ammine allowed to fill those cavities should have an effective radii from 1.46 to 2.92 Å [7, 15, 12].

Alkali metal ions, ammonium cation (NH_4^+) or organic amine are the three species that can be found in the A-site of the formate hybrid perovskites. The alkali family compounds can be synthesized by using mild reaction condition. For example, $CsCo(HCOO)_3$, $RbMn(HCOO)_3$ and $KMn(HCOO)_3$ are obtained by mixing a methanol solution of formic acid, the alkali metal formate salt and the transition metal salt; in a few days crystals can be collected with a good yield [16, 17,

[18]. On the contrary, $KCo(HCOO)_3$ can be obtained by recrystallization of its chiral polymorph in few weeks. The ammonium and hydrazinium family can be synthesized in both mild and strong condition, which will be explained in Chapter 2 and 3 of this work respectively. For what concerns larger organic amine cations, the methylammonium-template formates are obtained by mixing the transition metal salt, methylamine, and formic acid, using methanol as solvent [9, 19, 20]. The obtained compounds are $[MA][M(HCOO)_3]$ with $M = Mn^{2+}, Cu^{2+}, Zn^{2+}, Ni^{2+}$ and Mg^{2+}, instead for $M = Co^{2+}$ a hydrothermal reaction is required, using a stoichiometric water-methylformamide solution of cobalt salt, sodium formate and methylammonium chloride [21]. The ethylammonium formate compounds are similarly obtained in mild condition by mixing formic acid and the transition metal salt in methanol [9, 22, 23]. For other formate compounds, such as the formamidinium family, the synthesis procedures require stronger conditions, in which the amine cation is generate by the hydrolysis of the formamide at high temperatures. For example the solvothermal reaction is made at moderate temperature mixing the metal salt, formamide and cyclobutene-1,10-dicarboxilic acid [24, 25, 26]. Methylhydrazine compounds (MHy) are synthesized by layering a methanol solution of the metal salt on another methanol solution of formic and methylhydrazine [27], whereas the dimethylammonium cation formate family is usually synthesized in solvothermal conditions, using DMF-water mixture as source of dimethylammonia; hydrothermal and mild operating conditions are less used [28, 29, 19, 30].

It is interesting to note that all the synthesis described above are performed in methanol; in fact, the use of a non-coordinating solvent is crucial for the success of the reaction. Moreover, small amounts of water coming from the metal salts or from the air moisture can be detrimental for the synthesis and often leads to the formation of the metal formate hydrate compound ($M(HCOO)_2 \times 2H_2O$) as by-product. Nevertheless, when Guanidinium cation (GUA) is used, the reaction must be done in water or in a water-methanol mixture [19, 25, 31]. Azetidine compounds are also prepared using formic acid, the transition metal salt and methylamine [9, 32, 33]. Slowly diffusion method is also used to obtain formates with imidazole cation in the A-site (HIM); the synthesis requires a methanol solution of imidazole and formic acid in which another methanol solution of the metal salt is added [34, 35]. It's interesting to note that also in this case it is possible to replace methanol with a water solution of imidazole and formic acid. Also mixed-organic amine cations in the A-site are possible, for example mixing aziridinium with methylammonium or hydroxylamine [36, 37].

1.2.2 Symmetries and Crystal structures

The way in which the formate anion is bonded is crucial for directing the architecture of the final formate hybrid compounds. An *anti-anti* coordination leads to the perovskite architecture and this allows to insert in the cavity large amine cations [15]. The formate group can also be present in the *syn-anti* coordination for example in $[NH_4][Cd(HCOO)_3]$, $KMn(HCOO)_3$, $KCo(HCOO)_3$ and $RbMn(HCOO)_3$ [16, 17, 18, 38]. In these cases, the asymmetric coordination of the formate molecule reduce the atomic distances and consequently the volume of the cavity is reduced, hence, only small cations like K^+ or NH_4^+ can enter. $[NH_4][Cd(HCOO)_3]$ and $RbMn(HCOO)_3$ are present in the perovskite structure, instead for $KCo(HCOO)_3$, the resultant structure consists on $M(HCOO)_3^-$ framework network topology with hexagonal channels along the *c*-axis in which the A cation is located. Different is the case of $KMn(HCOO)_3$ in which the Mn atoms are linked to the K atoms through three oxygens atoms belonging to three formate molecules, the potassium atom is located on a rotation axis parallel to the *b* axis and is coordinated with four oxygen atoms.

On top of the formate bridge geometry, the crystal symmetry and all the host-guest interactions are, in first approximation, determined by the shape, size, and nature of the A-site cation. The non-spherical nature of the organic cation leads to lower-symmetry crystal structures at room temperature with respect to the oxides perovskite counterparts. The use of the tolerance factor (TF) gives a range between ~0.784 and 1.040 in which the perovskites structure can be found [7]. Nevertheless, compounds like $KMn(HCOO)_3$, $KCo(HCOO)_3$ and $RbMn(HCOO)_3$, containing an high spherical alkali metal with *syn-anti* coordination mode of the formate bridges, crystallize in the perovskite structure with an orthorhombic or monoclinic space group with a TF between ~0.6 and 0.7 [16, 17, 18], demonstrating that the organic components in these structures give a complex lattice matching difficult to rationalize. As an example methylammonium and ethylammonium cation in the manganese-formate based, give a orthorhombic perovskite, instead, only with dimethylammonium the crystal lattice changes to trigonal [9]. Moreover, the size of the A-cation influences the packing and the volume of the cavity that increases as the size of the amine increase, going from 57 A^3 for the methylammonium to 94 A^3 for the azetidinium cation, also increasing the TF factor that changes from ~0.859 to 0.993 [9].

For what concerns the B-site, ionic radii and orbital order influence the crystal structure symmetry. Taking the guanidinium family as an example, $[GUA][M(HCOO)_3]$, compounds with manganese, iron, cobalt and nickel crystallize all in the *Pnna* space group with decreasing unit cell volume with M following the

ionic radii trend [31]. In particular, the cavity volume shrinks from 80 A^3 for manganese to 66 A^3 for nickel due to the shrinking of the M-O bond lengths and the increasing of the C-O bond lengths in the formate anion [31]. As well as the inorganic counterpart, also the hybrid organic-inorganic perovskites show the influence on the magnetic structure of the Jahn-Teller distortions due to the *3d* metals. This can easily be seen in the guanidinium family comparing the structure with Zn^{2+} to the one with Cu^{2+}. The crystal structure with copper is still orthorhombic, but the space group lowers to $Pna2_1$ [31]. In fact, even if the ionic radii of the two metals are similar (0.74 *vs* 0.73 Å) their coordination is different. The ZnO_6 octahedra possess Zn-O bond lengths between 2.086 and 2.127 Å with a trivially distorted geometry, instead in the Cu compound two Cu-O lengths are significantly elongated (2.360 and 2.383 Å) with respect the other four (from 1.852 to 2.000 Å) due to the Jahn-Teller effect. This ~10% shrink of bond lengths causes different changes in the host-guest interactions between the framework and the organic cation.

It is also interesting to underline how the hydrogen bond between the amine and the framework influence the physical properties of the hybrid perovskites. In fact, the hydrogen of the amine function as an H-donor, instead the oxygen of the formate anion act as H-acceptor [7, 15]. Different amine can modulate strength and geometries of the hydrogen bonds; for example, in methylammonium and ethylammonium compounds, bond strengths are normally weaker as expected [9] and increasing the number of H-donor such as using $(CH_3)_2NH_2^+$, hazetidinium or hydrazinium cation, the bond interactions are stronger due to the multiple H-bond donor [39, 24]. Finally, is worth stressing that the hydrogen bonds can influence the crystallization and the thermal stability. In fact, the [GUA][$M(HCOO)_3$] family of compounds can crystallize in water and the higher thermal stability and resistance to moisture support the hydrogen-bond effect. Nevertheless, also the metal in the B-site have an effect on the hydrogen bond, for example changing the B-O lengths and consequently the H···O lengths. This effect can easily be seen comparing [GUA][$Zn(HCOO)_3$] and [GUA][$Cu(HCOO)_3$] which is effected by Jahn-teller distortion.

1.2.3 Physical properties

1.2.3.1 Phase transition

The highest symmetry allowed for the hybrid perovskites is the cubic space group $Pm\bar{3}m$. Nevertheless, other distorted structures with low symmetry are present. Generally, the structural distortions in perovskites are caused by the displacement of either the A or B sites or by a tilting of the BX6 octahedra. When the X ion is replaced with an organic molecule, such as the formate anion, the octahedra are no more corner sharing and more complex octahedral tilting schemes

can be expected with respect to the inorganic perovskites; in the case of the formate anion the rigidity of the molecule is strong enough to mediate the tilting of the octahedra, extending the possible tilting schemes with respect to the inorganic perovskites. In fact, the flexibility of the anion molecule can add additional degrees of freedom like: columnar shifts [40], unconventional tilts [41, 42] and multipolar order [43, 44]. The first two of these belong to the rigid-units modes (RUMs) [45], for example the phonon modes which propagates into the structure without deforming the BX6 coordination geometries [46, 47]. The additional flexibility is, thus, reflected in a large number of RUMs. In contrast, the presence of multipolar degrees of freedom is related to the reorientation of the non-sphericity of the A-site cation [43, 44, 8]. In 2018 Bostrom et.al analysed all these types of distortions related to the hybrid perovskites [48] and show how these structural degrees of freedom can be combined to obtain inversion symmetry breaking and thus to establish new rules to design acentric molecular perovskites. The classification of the possible distortion is reported in Figure 1.2.3-1 48 that summarize the different degrees of freedom available for the hybrid perovskites.

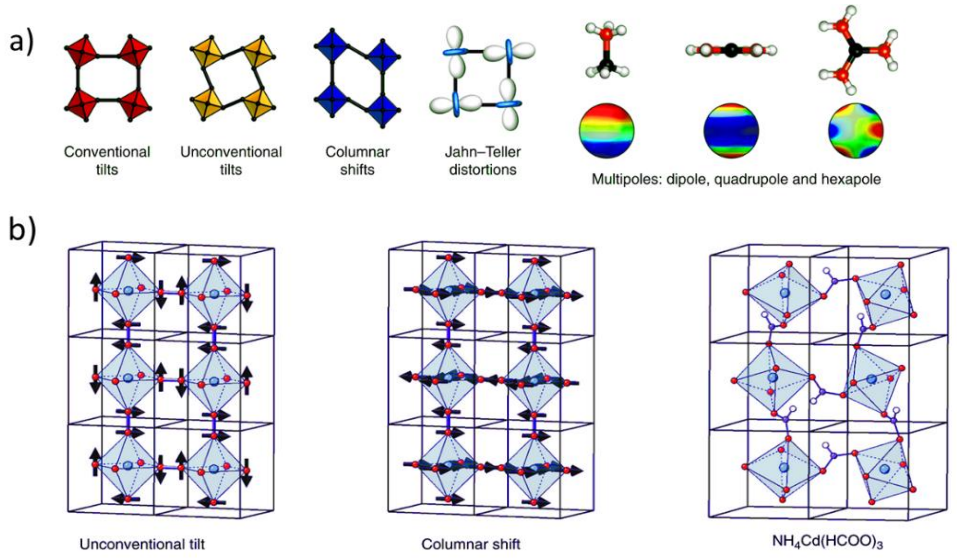

Figure 1.2.3.1-1: possible degrees of freedom of the hybrid perovskites. a) possible degrees of freedom accessible to hybrid perovskites; b) combination of two distortions: unconventional tilt (left) + columnar shift (centre), that causes the distortion of the $NH_4Cd(HCOO)_3$ hybrid perovskite (right).Pictures taken from the Ref 48.

Regarding the distortions of the A and B sites, the off-centre displacements are similar to the inorganic perovskites, but due to the presence of an organic cation and not a single atom, the situation is more complicated. Indeed, in various instances the A site molecules are disordered over two or more position and usually a symmetry breaking order-disorder transition is observed on cooling [49]. The synergic combination of displacements, order-disorder and octahedra tilting, usually generates complex transitions. Moreover the hydrogen bonds between the by the A-site cation, which usually is a polar molecule, can induce a spontaneous polarization [50, 49]. Hence, the strengths of the hydrogen bonds and the dipole moments of the A-site cation can influence the ferroelectric or anti-ferroelectric ordering.

For example $[(CH_3)_2NH_2][Mn(HCOO)_3]$ undergoes a phase transition at 190 K, with a behaviour typical of hybrid compounds due to the order-disorder of the A-site cation. In this compound, at high temperature (HT), the dimethylammonium (DMA) cation is equally distributed over three positions, instead al low temperature it orders choosing only one site. The HT symmetry is trigonal $R\bar{3}c$ and the symmetry-breaking process leads to a monoclinic Cc space group. During the transition a change of the hydrogen bonding occurs, and together with the order-disorder of the DMA cation, the MnO_6 octahedra tilts, resulting in a ferroelectric-ferroelastic transition. The polar DMA cation facilitate this process by forming at LT hydrogen bonds that give rise to the ferroelectricity. This mechanism is different from the known B-site displacement in the ferroelectric perovskites oxides.

1.2.3.2 Magnetic Properties

Due to the high versatility of the perovskite framework, able to accept various species on the A and B-site, hybrid perovskites exhibits many physical properties, such as dielectric, magnetic, ferroic, caloric, mechanical and combination of them [7].

Magnetism has been the first property explored in the formate-based hybrid perovskites, and their magneto-structural relationship have been largely studied [7, 15]. The formate linker can mediate only weak exchange couplings, due to its length, and so the materials exhibit long-range magnetic ordering at low temperatures usually below 50 K. The tilting of the MO_6 octahedra, linked through the *anti-anti* formate, leads to exchange pathways that, in most of the cases, results in canted anti-ferromagnetism and weak ferromagnetism [51]. The magnetic behaviour of the formate family has been studied since 2004 for compounds with different A-site cation: MA, ethylammonium (EA), DMA and azetidinium (AZE) [9] which show long-range anti-ferromagnetism below 9K with a slight non-collinear arrangement of the moments (Figure 1.2.3.2-1).

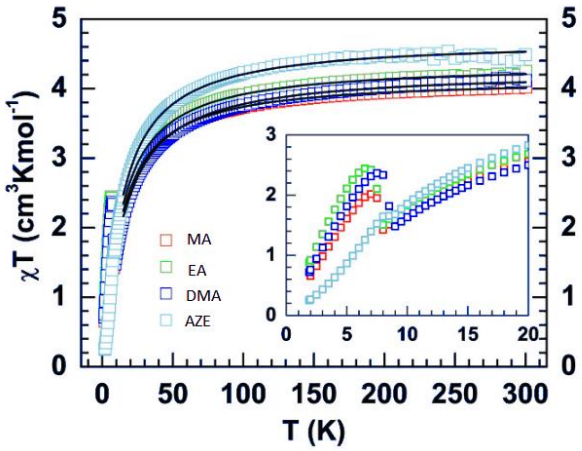

Figure 1.2.3.2-1: XmT versus T for different manganese-formate compounds with A = MA, EA, DMA AZE. Picture taken from Ref 9.

The magnetic coupling through the formate linked in *anti-anti* mode is <-0.5 J/cm and quite weak [9]. The weak ferromagnetic moment arises from the anti-symmetric exchange between adjacent M^{2+} sites via the formate bridges that is confirmed by alternating current (AC) measurements. When the B-site is substituted with different magnetic metals having larger spins, the spin canting angles of formate perovskites increase and the spontaneous magnetization becomes larger. In the $[DMA][M(HCOO)_3]$ family when the B-site changes from Mn^{2+}, Co^{2+} and Ni^{2+} the compounds show canting angles of ~0.08°, 0.5° and 0.6° respectively[52].

1.2.3.3 Dielectric properties

The role of the organic cation in the A-site influences also the ferroelectric and dielectric properties in the formate perovskites [50]. As the polarizability of dielectric materials strongly depends on the structure degrees of freedoms, it is possible to manipulate the dielectric properties by varying the dynamic motions of the electric dipole in the lattice. In fact, the order-disorder transition of the A-site amine can be utilized to develop new dielectric materials [7].

The first attempt has been done using the azetidinium cation (AZE) in $[AZE][M(HCOO)_3]$ with M = Mn^{2+}, Cu^{2+}, Zn^{2+} [32, 33, 52] by exploiting its conformational order which switches to a non-polar and planar configuration at high temperatures. The structural analysis shows a first-order structural phase transition when the AZE cation passes from a bended position to flattened (Figure 1.2.3.3-1).

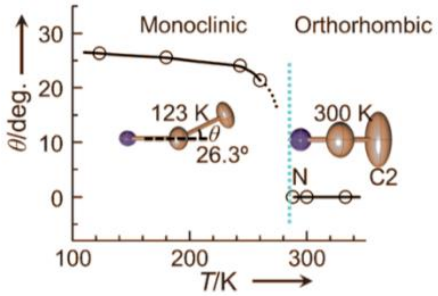

Figure 1.2.3.3-1: different conformation of the AZE cation at low and high temperature. Image taken from Ref 34.

AZE compounds showed large dielectric permittivity (ε') higher than 10^4 above room temperature [32]; moreover, they showed a strong frequency dependence of about two orders of magnitude. These values have been already found in polarizable perovskite oxides, for example in $BaTiO_3$ [4]. This example shows how the conformational instability and the puckering dynamic of the AZE cation are important to the colossal dielectric anomaly observed across the phase transition. Further ^{1}H-NMR proved how the high susceptibility of the potential curve may be a reason for the onset of these giant dielectric anomalies near phase transition temperature [33].

By mixing different amine in the A-site it is possible to obtain a solid solution of hybrid formate compound. The resulting crystal structure, with a new distorted framework and dipole rearrangement strongly influence the dielectric properties. As an example, the solid solution $[(HAZ)_x(MA)_{1-x}][Mn(HCOO)_3]$ shows a decrease of the critical temperature with decreasing the HAZ content.

1.2.3.4 Ferroelectricity

The first reported formate-hybrid perovskite that shows ferroelectricity is the $[DMA][M(HCOO)_3]$ (M = Mn, Fe, Co, Ni, Zn) family of compounds [30, 49]. The first studied structure has been $[DMA][Zn(HCOO)_3]$ for which single-crystal x-ray diffraction showed disorder at ambient condition for the amine cation. Successively analysis suggested a phase transition, due to the ordering of the DMA cation at 160 K. The $[DMA][Mn(HCOO)_3]$ also shows a phase transition at about 190 K triggered by the switching of the DMA cation from three possible orientation to one [53]. The symmetry of the compound changes from non-polar trigonal $R\bar{3}c$ to polar monoclinic Cc, but it has not been possible to obtain a clear ferroelectric loop. A clear evidence

of a switching of the spontaneous polarisation has be obtained only successively on the deuterated compound [DMA][Co(DCOO)$_3$].

In this case the same transition occurs at about 151 K caused by the order-disorder transition of the A-site cation (Figure 1.2.3.4-1) [54].

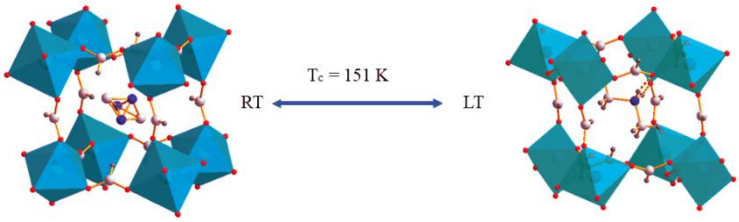

Figure 1.2.3.4-1: crystal structure of deuterated [DMA][Co(DCOO)$_3$] above and below the ferroelectric phase transition. Image taken from Ref 50.

In Figure 1.2.3.4-2 are reported the ferroelectrics loop obtained for deuterated [DMA][Co(DCOO)3]; the spontaneous polarization is saturated at about 1.02 μC cm-2 five times higher than Rochelle's salt (0.2 μC cm-2) [54].

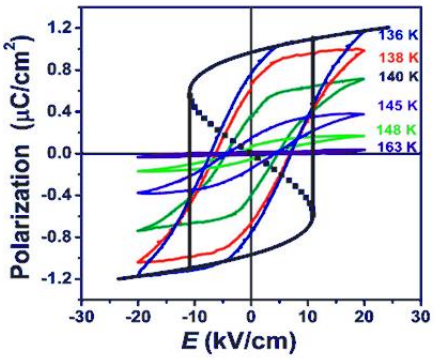

Figure 1.2.3.4-2: hysteresis loops obtained for deuterated [DMA][Co(HCOO)$_3$] below the T_c. Image taken from Ref 51.

This example shows the potential for ferroelectricity in the hybrid perovskites and opens new road to investigate other ferroelectrics perovskites also by computational methods [55, 56, 57, 58]. Taking as example the DMA family of compound, it is possible to replace the first row transition metal in the B-site with Mg^{2+}, this increases the transition temperature of the material to ~270 K, making this composition promising for applications [59]. This behaviour is due to the higher Lewis acidity of Mg^{2+} compared to the other metals. Thus, the Mg-O bond is more localized

causing a stronger H-bonds network between the DMA cation and the framework, leading to higher transition temperatures.

1.3 Polymorphs of the formate compounds

Beside the perovskite structures, formate compounds can be also present in other polymorphic phases (see Chapter 2) [39, 60]. One of the most studied polymorphs is the chiral or channel one [39, 60, 61, 62] which possess the same atom arrangement and same stoichiometry of the perovskite, but different framework. In fact, these structures possess channels along the *z* direction, not present in the perovskite phases. Chiral phases are detected both for the hydrazine and ammonium-based compounds even if with some differences. They have attached attention due to their interesting magnetic properties; moreover, the hydrazine-based compounds are predicted as ferroelectric materials [39] and the ammonium-based have shown experimentally a ferroelectric behaviour [61, 62] (see Chapter 2 and 3 for more details).

1.4 Aim of this work

Due to high potential of the hybrid formate perovskites material, we decided to focus our work on the ammonium family with general formula $[NH_4][M(HCOO)_3]$ and the hydrazinium family, with general formula $[NH_2NH_3][M(HCOO)_3]$. As the majority, if not all, of the physical measurements included the ferroelectric one, are performed on single crystals, making the material less available for application, one of the aims of this thesis was performing physical measurements on polycrystalline materials. This process required the adjustment of some synthesis reported in literature to obtain single phase powders and the deeper investigation of different behaviours of the material not yet studied, for example their general instability in air and the relation between different known polymorphs. To perform ferroelectric measurements on polycrystalline material it has been necessary to develop a new device to perform ferroelectric tests on the tablets of the sample, also tested on $BaTiO_3$ tablets. Moreover, for what concerns the ammonium family, a new mechanochemical synthesis approach has been developed allowing us to obtain single phases of the samples using simple reagents. In parallel to these attempts, due to the already known ionic conductor behaviour of MOFs and porous material, we performed ionic conductor measurements on all our samples.

2 AMMONIUM COMPOUNDS

2.1 Crystal structure

Ammonium formate compounds have general formula $[NH_4][M(HCOO)_3]$, where M is usually a divalent *3d* transition metal, an alkaline-earth metal or a post transition divalent cation [62, 61, 63, 64, 65]. At room temperature, all the compositions possess the $P6_322$ space group with the only exception of M=Cu which shows an orthorhombic structure with $P2_12_12_1$ symmetry due to a strong Jahn-Teller distortion of the Cu^{2+} coordination polyhedral [63]. The divalent metal is octahedrally coordinated by six oxygen atoms that belongs to the formate anion. The latter can bridge between the metals sites in three ways as shown in Figure 2.1-1. In the case of the $[NH_4][M(HCOO)_3]$ compounds all the formate are bonded in *anti-anti* configuration. The formate bridges create an anionic framework with hexagonal cavities that are filled with NH_4^+ (Figure 2.1-1).

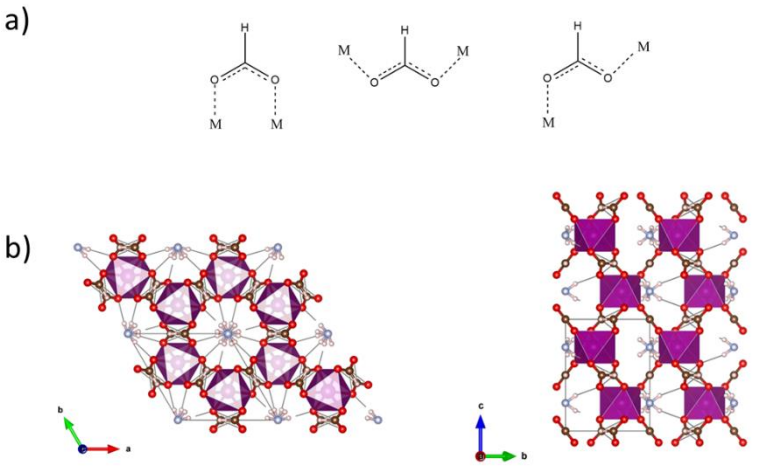

Figure 2.1-1: a) three types of coordination for the formate anion. From the left: anti-anti, syn-syn, syn-anti. b) crystal structure of [NH4] [Mn(HCOO)3] viewed along the z axis (left) and along the a direction (right).

At room temperature the ammonium cation is disordered and possess two preferential orientations as shown in Figure 2.1-2.

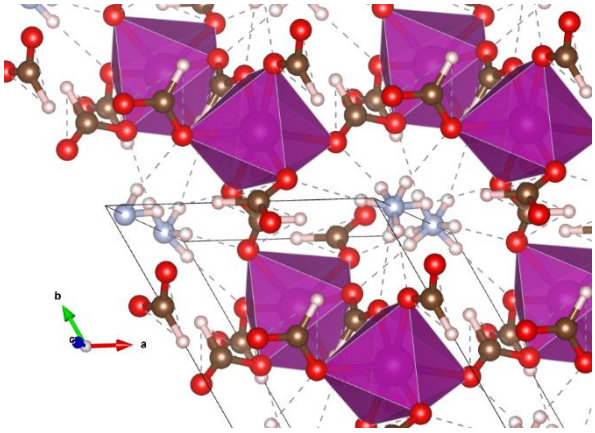

Figure 2.1-2: perspective view along z of the channel structure in $[NH_4][Mn(HCOO)_3]$. In dashed are reported the N-H···O and the H···O hydrogen bonds between the NH_4^+ cation and the formate molecules. Crystal structure taken from Ref 62.

The crystal structure is chiral due to the presence of only one enantiomer of the formate molecule that forms three triple helixs with a pitch of 3 times *c* with a repetition of six metal ions [62]. The channels have a diameter of about 3.1 A (not including van der Waals radii) in which the organic cation is located; NH_4^+ is anchored at the framework through four hydrogens bonds: two N···O (one weak and one strong) and two N-H···O (one weak and one strong). By comparing the structures with different metals, it is possible to observe a correlation between the ionic radii of the metals and the M-O lengths (Figure 2.1-3 and Table 2.1-1). The different ionic radii cause a contraction in the lattice parameters and as consequence in the M-M distances [62].

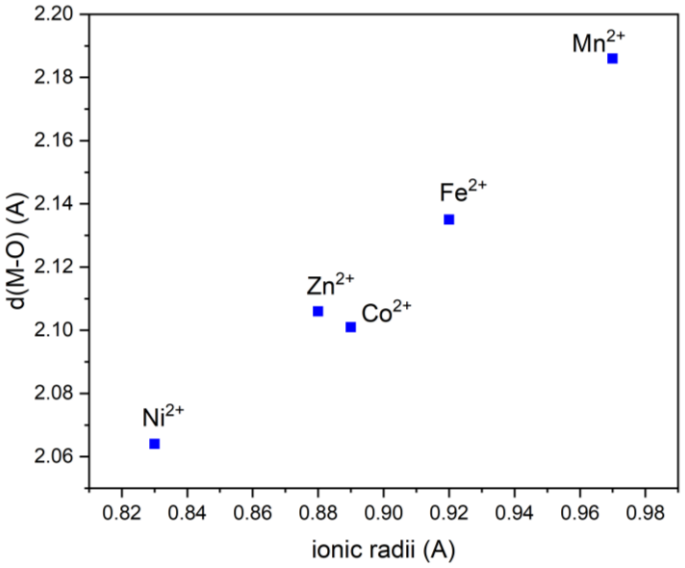

Figure 2.1-3: correlation between ionic radii of Mn^{2+}, Fe^{2+}, Zn^{2+}, Co^{2+} and Ni^{2+} and the M-O distances in the $[NH_4][M(HCOO)_3]$ structure. On the right is reported the table with the effective values.

Table 2.1-1: ionic distances and M-O lengths for each structure with different divalent metal [62,61]

Metal ione	Ionic radii	d(M-O)
Mn^{2+}	0.97	2.186(1)
Fe^{2+}	0.89	2.101(1)
Co^{2+}	0.83	2.064(1)
Zn^{2+}	0.87	2.106(1)
Ni^{2+}	0.92	2.135(1)

The M = Cu^{2+} compound present an orthorhombic structure with the $P2_12_12_1$ space group from 94 to 353 K. At 353 K a phase transition occurs, and the crystal lattice changes to the hexagonal $P6_322$ [63, 66]. With the help of Raman spectroscopy, Shang *et al*. recently discover another phase transition at 220 K not visible with XRD diffraction. This analysis indicate the presence of the Jahn-Teller active Cu^{2+} as the main difference between $[NH_4][Cu(HCOO)_3]$ and the other ammonium-formate. Indeed, the Jahn-Teller effect causes distortion in the CuO_6 octahedra which

eventually leads to the symmetry reduction. Moreover, the distortion modifies the lengths of the axes and most importantly the H-bonds of the ammonium cation and its position in the cavity [63]. In fact, this distortion that occurs for $[NH_4][Cu(HCOO)_3]$ causes differences between the length of the apical and basal bonds; this difference is around 0.45 Å at LT (120 K) and 0.17 Å at HT; for all the other ammonium formate compound this difference is less than 0.03 Å. In Table 2.1-2 are reported the basal and apical bonds for M = Mn^{2+}, Fe^{2+}, Co^{2+}, Ni^{2+}, Zn^{2+} and Cu^{2+} [61, 63].

Table 2.1-2: M-O bonds lengths for basal and apical bonds in $[NH_4][M(HCOO)_3]$ at 290 K [61, 63].

Metal	Basal length	Apical length
Mn^{2+}	2.185(1)	2.185(1)
Fe^{2+}	2.135(1)	2.135(1)
Co^{2+}	2.102(1)	2.102(1)
Ni^{2+}	2.064(1)	2.064(1)
Zn^{2+}	2.016(1)	2.016(1)
Cu^{2+}	1.963(1)-1.987(1)	2.399(2)-2.419(2)

2.2 Known synthesis protocols to obtain ammonium-formate compounds

The synthesis of the $[NH_4][M(HCOO)_3]$ (M = Fe^{2+}, Mn^{2+}, Co^{2+}, Zn^{2+}, Ni^{2+}) formate's are performed by a mild chemistry approach; usually a methanol solution of ammonia and formic acid is prepared in a glass tube. Later a methanol solution of the metal (generally obtained from chlorides or perchlorates salts) is gently layered on the top of the ammonia and formic acid solution. The tube is then sealed and left undisturbed; after one day it is possible observe the formation of single crystals of different colours, for example with M = Fe^{2+}, Mn^{2+}, Co^{2+}, Zn^{2+} the obtained crystals are pale green, pale pink, deep pink and colourless respectively [62, 61]. The reaction can also be performed using a methanol solution of NH_4HCOO and HCOOH in which the methanol solution of the metal is layered on the top [62]. The yield of the reaction varies from 60 % to 80%. In addition to these classic methods, it is possible to use other reagents, for example ammonium formate as source of ammonium [61, 63] or using dimethylformamide (DMF) in methanol as source of formate in solvothermal conditions [67]. For what concerns the source of metal, the reactant is generally a chloride or perchlorate [68]. In all these types of synthesis it has been noticed that the presence of small amount of water during the crystallization, as humidity or in the metal salts, often leads to the formation of $M(HCOO)\cdot 2H_2O$ as spurious phase, and also the use of a non-coordinating solvent, as it is methanol, is crucial. Nevertheless, in literature examples of synthesis done with hydrated salts are

present. [62, 61]. In some cases, the synthesis procedures reported in literature lack of details [69]. Indeed, the quantity of the reagents and the molar ratio are not always clearly stated. For example, it is mentioned that small amount of water could lead to the formation of the hydrated form of the metal formate, but this issue has never been investigated deeply, mostly because the metal salt used as reagents are already hydrated and none of the liquid reagents is actually dehydrated. Moreover, the molar ratio between ammonia, metal and formic acid is not very clearly reported and in most synthesis ammonia and formic acid are added in excess respect to the metal [69, 62].

2.3 Material characterization

To characterize the $[NH_4][M(HCOO)_3]$ formate family it is possible to use different techniques. The most used are single crystal XRD, thermal analysis, IR and Raman spectroscopy, Uv-Vis spectroscopy, and dielectric, magnetic and ferroelectric characterizations. Moreover, the structures with M = Co, Mn, Fe, Ni have been characterized by neutron diffraction.

2.3.1 Single crystal characterization

For what concerns the single crystal characterization, it has been used by Kurmoo *et al.* to determine in 2007 the structure of $[NH_4][M(HCOO)_3]$ with M = Co, Mn, Ni [62], then in 2010 Song Gao *et al.* reported the structure of M=Zn [61], Fe [62] and Cu[3].

2.3.2 Thermal characterization

In general, for M = Co, Mn, Ni, Zn, differential scanning calorimetry (DSC) and thermogravimetric analysis (TGA) show different loss of weight belonging to the loss of one ammonia and one formic acid per formula that leads to the formation of $M(HCOO)_2$ and then the decomposition occurs in the 553-603 K temperature range (except for $[NH_4][Cu(HCOO)_3]$ for which the decomposition temperature is lower (110°C)) [70]. The literature describes accurately only the data for M = Co, Mn, Ni [62], instead for M = Zn the thermal properties were investigated only to determine the heat capacity of the compound, but the traces showed the same trend as the other compounds [71].

Thermal properties have been helpful to determine phase transitions that occurs for the compounds with M = Co, Ni, Mn, Zn, Fe, for which in a range between 191 and 254 K there is a phase transition from the $P6_322$ space group to the polar $P6_3$ which allows for a spontaneous polarization [61]. Different is the case for $[NH_4][Cu(HCOO)_3]$, which shows a structural transition at 359 K from the $P2_12_12_1$ space group to the $P6_122$ [63, 66].

2.3.3 Raman spectroscopy

Raman spectroscopy has not been largely used to study these materials. The first study from Kurmoo et al. analysed the compounds with M = Mn, Co, Ni [14] and then Hanuza et al, studied the samples with M = Mg, Co, Fe, Mn, Zn [63]. In the latter works they performed a temperature-dependent study which correlates the transition temperature observed from the XRD diffraction and the splitting of some specific modes; they also found a correlation between the phase transition temperature and the activation energy of re-orientation motions of NH_4^+. They proved that these transitions are governed by the bond's strength between the ammonium cation and the formate frameworks.

2.3.4 Dielectric, magnetic and ferroelectric characterization

Many studies have been conducted on the dielectric and magnetic properties of these materials, especially for M = Co, Mn, Fe and Ni. Magnetometry measurements [62, 61, 63] show different behaviours depending on the magnetic cation at low temperature; in fact, the Mn compounds is antiferromagnetic [62], whereas Co, Ni and Fe possess a weak ferromagnetic behaviour [62]. In particular for M=Co two magnetic phase transitions have been observed around 9 and 6 K [62]. The weak ferromagnetic moment is due to the antisymmetric exchange that occurs via the noncentrosymmetric HCOO bridges and the single-ion anisotropy in Co and Ni enhanced this behaviour.

$[NH_4][M(HCOO)_3]$ compounds with M = Mn, Fe, Co, and Zn have shown to be ferroelectric; S. Gao *et al*. [61] reported a paraelectric to ferroelectric transition in a single crystal of $[NH_4][Zn(HCOO)_3]$ at a critical temperature of 191 K. Later the same group reported a similar behaviour also for single crystals of the other compounds, with a T_c of 256 K (Mn), 170 K (Fe), 193 K (Co). [62] The ferroelectric properties were investigated through dielectric permittivity and polarization measurements, which revealed a ferroelectric behaviour when an electric field is applied along the *c* axis below the phase transitions temperatures and an increasing spontaneous polarization with the decreasing of the temperature. The structural changes at the ferroelectric transition involves an elongation of the *c-axis* and an ordering of the NH_4^+ cations from trigonal antiprism to ordered tetrahedral. This phase transition lowers the symmetry form $P6_322$ at HT to the polar $P6_3$ at LT.

For $[NH_4][Cu(HCOO)_3]$ dielectric and magnetic investigations have also been performed [70]. Magnetic measurements showed a long-range antiferromagnetic behaviour at low temperature with a Nèel temperature of 2.9 K, the lowest of the ammonium-formate family [62].

2.4 Synthesis of $[NH_4][M(HCOO)_3]$ M = Mn, Fe, Co

In this work the formate with M = Fe^{2+}, Mn^{2+} and Co^{2+} have been synthesized with a liquid approach. 2 mmol of metal salt ($FeCl_2$, $MnCl_2$ x $4H_2O$, $Co(NO_3)_3$ x $6H_2O$) were dissolved in methanol, then this solution was carefully layered on the top of a solution made mixing ammonia and formic acid in methanol (see Experimental Methods). The resulting solution is colourless for the compound with Mn, pink for Co, and grey/blue, for Fe. After some hours it is possible to observe the formation of a precipitate on the bottom of the tube and some little crystals at the interface of the two solutions for the compound with Mn and Co. The obtained crystals of Mn and Co are not sufficiently large to be use for ferroelectric characterizations, and they are also formed by cluster of crystal which are difficult to separate. Furthermore, it is not a purpose of this thesis trying to characterize single crystal of these materials, so the grow of large crystal has not been a priority.

The synthesis of the M=Fe compound has been more challenging. During the stratification of the metal solution, we observed the formation of a brown sticky precipitate that is probably due to the formation of iron hydroxide that turns brown when the oxidation state of Fe increases. Despite this problem, it has been possible to obtain $[NH_4][Fe(HCOO)_3]$ by separating the brown precipitate from the formate.

In Figure 2.4-1 are reported the powder x-ray diffraction data (PXRD obtained with Thermo X'TRA diffractometer, see Experimental Methods) of the three obtained pure phases compared to the calculated ones. It is possible to note that in the pattern of $[NH_4][Fe(HCOO)_3]$ the phase has some non-identified impurities due to the difficulty explained to obtain a pure sample.

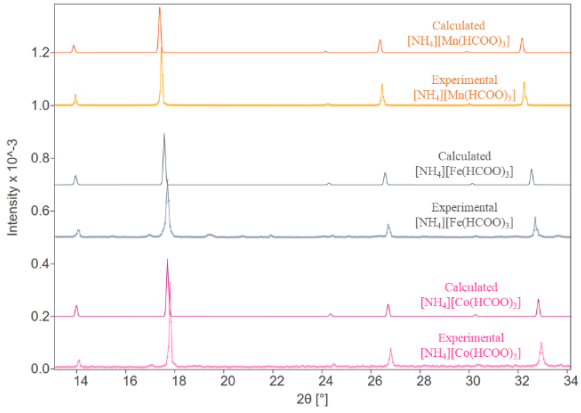

Figure 2.4-1: experimental and simulated (top) PXRD patterns of $[NH_4][M(HCOO)_3]$ obtained from the liquid synthesis. Data are collected with Thermo X'TRA diffractometer. From the top M = Mn, Fe, Co.

In Figure 2.4-2 is reported a Le Bail fitting of $[NH_4][Mn(HCOO)_3]$ and in Table 2.4-1 the obtained cell parameters compared to literature [62]. Even though the fitting confirms the presence of the main phase, often in the PXRD measurement is present a peak at about 2θ = 16.7º that we have not been able to assign; it doesn't belong both to the reagents and to the product or to the metal formate hydrate.

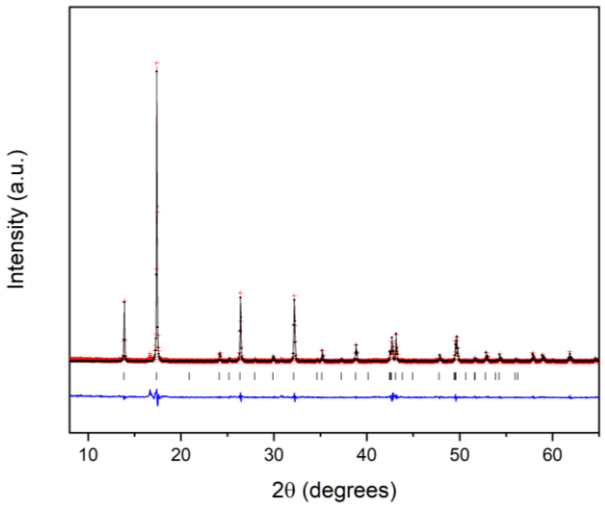

Figure 2.4-2: Le Bail fitting of [NH4][Mn(HCOO)3]. Black crosses, red line and blue line indicates the observed, calculated and difference data respectively, whereas the tick marks indicate the Bragg position of the main phase.

Table 2.4-1: cell parameters of $[NH_4][Mn(HCOO)_3]$ obtained from Le Bail fitting compared to literature.

Axis	Lengths (This work) Å	Lengths (Literature) [1] Å
a	7.370(1)	7.356(2)
b	7.370(1)	7.356(2)
c	8.496(3)	8.478(2)

We have observed that for the synthesis of the Mn and Fe compounds was difficult to obtain a pure phase due to the presence of the $M(HCOO)_2 \times 2H_2O$ impurity (variable from wt% = 64 to wt% = 10% in the case of $Fe(HCOO)_2 \times 2H_2O$ instead $Mn(HCOO)_2 \times 2H_2O$ is present in a percentage between wt% = 20 and wt% = 50%).

In the synthesis reported in literature there is no indication of such issue, and we suspect that these problems are caused by the presence of water both in the solvent and in the starting hydrated reagent [64]. Saines and co-workers performed neutron diffraction analysis on the ammonium-formate family with M = Mn, Fe, Co, Ni, and, as we observed, they found difficult to obtain a pure phase of the samples due to impurities caused by the water present in the reaction mixture [64]. Moreover, also in this case the diffraction pattern of the sample with Fe shows a significant amount of an unknown impurity. An important remark is that the analysis conducted in the past were done on single crystals [62, 61], while P. J. Saines [64] and in this work the analysis are performed on powder samples.

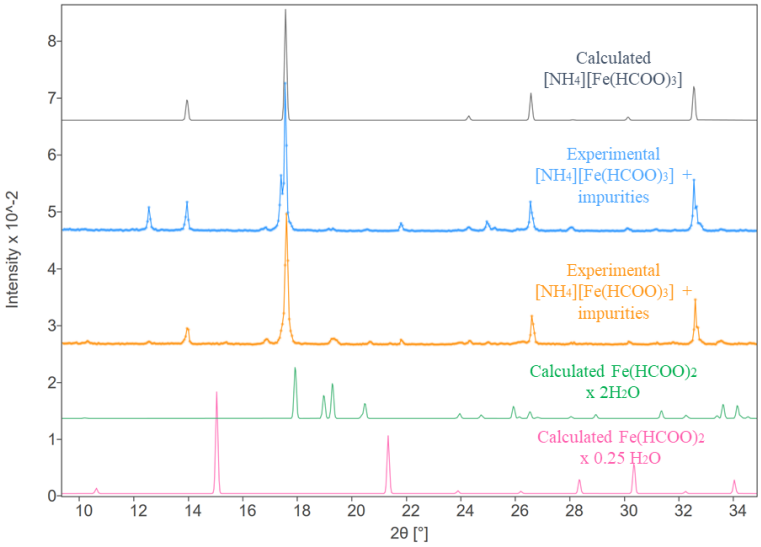

Figure 2.4-3: PXRD patterns obtained with Thermo X'TRA diffractometer of two batches of $[NH_4][Fe(HCOO)_3]$ compared to the simulated pure phase and iron formate impurities with different quantity of water molecules (respectively from the top $2H_2O$ and $0.25H_2O$).

Figure 2.4-3 reports the PXRD data for $[NH_4][Fe(HCOO)_3]$, showing the presence of various impurities. The major impurity that have been individuated are $Fe(HCOO)_2 \times 2H_2O$ and in minimal quantity $Fe(HCOO)_2 \times 0.25H_2O$. Not all the extra-peaks have been assigned to a known impurity even though we suppose the presence of some oxide/hydroxide of iron, due to the predisposition of the iron to oxide at Fe^{3+} (Figure 2.4-4).

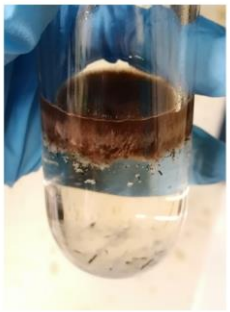

Figure 2.4-4: photo of the obtained reaction mixture for the synthesis of $[NH_4][Fe(HCOO)_3]$. On the top is visible the brown layer due to the formation of Fe impurities; attached on the side and on the bottom of the vessel there are very few dark crystals of the product and a colourless precipitate ($Fe(HCOO)_2 \times 2H_2O$).

Despite the issues previously discussed during our experiments we noticed the formation of an unknown product when $[NH_4][Mn(HCOO)_3]$ was left for four days in a vial inside a desiccator. This new phase, it turned out to be a polymorph of $[NH_4][Mn(HCOO)_3]$ and we found correspondence with the phase detected for the first time by P. J. Saines [64]. The crystal structure of this polymorph has been detected at 150 K and it shows $Pna2_1$ space group with an orthorhombic lattice. The formate anions are bonded to the Mn^{2+} in a *syn-anti* mode and not as usually observed in *anti-anti* mode. This kind of structure has been observed also for $[NH_4][Cd(HCOO)_3]$ [64]. The particularity of this polymorph is that the octahedra are heavily distorted, but, most importantly, there are two types of channels in the structure along the *a* direction. In one the hydrogen of the formate molecules is directed towards the channels, hindering the possibility to host the ammonium cation; the second type of channels, on the contrary, are large enough to be doubly occupied by ammonium molecules to maintain the ABX_3 stoichiometry (Figure 2.4-5).

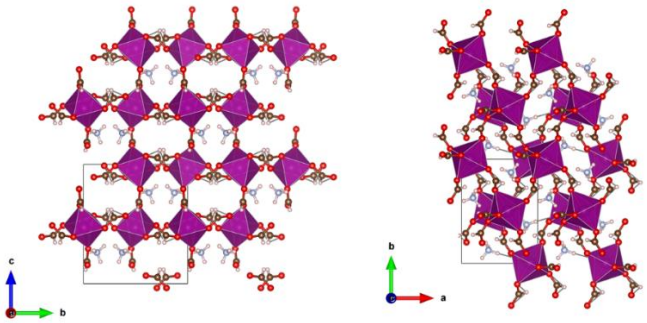

Figure 2.4-5: crystal structure of the perovskite-like polymorph of $[NH_4][Mn(HCOO)_3]$. On the left viewed along the x axis in which are visible the two types of channels; on the right viewed along the z axis.

In Figure 2.4-6 are reported the calculated PXRD pattern of $[NH_4][Mn(HCOO)_3]$ in the $P6_322$ space group, our experimental pattern and the calculated pattern of the polymorph of $[NH_4][Mn(HCOO)_3]$ with the $Pna2_1$ space group. The comparison confirms the presence of the perovskite-like polymorph in our experimental pattern together with traces of the first polymorph.

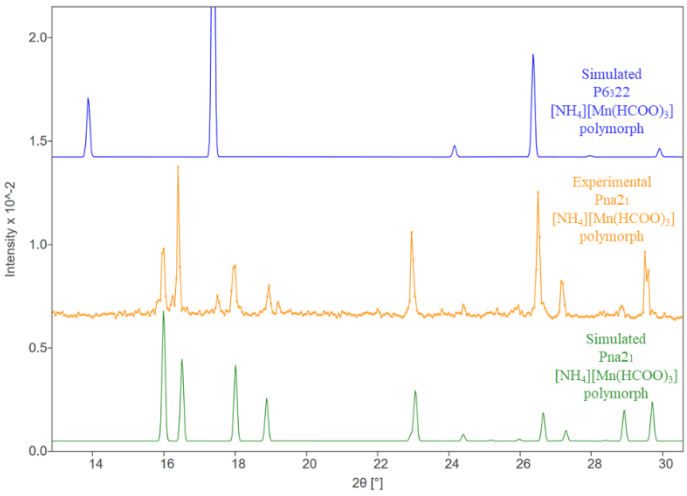

Figure 2.4-6: Comparison of the experimental pattern (middle) with the $[NH_4][Mn(HCOO)_3]$ in chiral polymorph $P6_322$ (top) and the second polymorph $Pna2_1$ (bottom). the patterns were collected using Thermo X'TRA diffractometer.

The comparison confirms the presence of the same phase detected in literature for this polymorph of $[NH_4][Mn(HCOO)_3]$ with P$na2_1$ space group [8].

2.5 Mechanosynthesis

2.5.1 State of the art

With the word "mechanosynthesis" it is identified a large field in synthetic chemistry, and it refers to the use of mechanical energy to perform a reaction. This energy could be provided in different ways as for example impact or compression. Most of the time, mechanosynthesis refers to the synthesis of compounds through hand grinding or milling; in particular the manual grinding is done with the use of a mortar and pestle, whereas milling is performed with the help of ball milling, shaker, or twin-screw extruders.

Grinding is the term used to describe the mechanical action that occurs during the synthesis starting from powders reagents, but this does not mean exclude the possibility to have liquid phases. Indeed, a small amount of liquid can be added

to the reaction mixture to accelerate the reaction by increasing the mobility of the reagents, such type of reactions are called “liquid assisted grinding” (LAG). Solvents can also be present in the starting reagents, for example if the materials are hydrated salts or molecular solvates, or in the atmosphere which aid the reaction; moreover, liquids like water or acetic acid may be generated as condensates 11. Despite this method, reactions could be performed also using the ILAG (ion-and-liquid assisted grinding) approach, in which a catalytic amount of liquid containing traces of salts additives is added to accelerate the reaction. In general, liquid assisted grinding (LAG) is required when the mobility of some components, related with the diffusion coefficients of the ionic species in solution (i.e., Cs+ shows high solubility in water), is a fundamental prerequisite for the expected mechanical synthesis.

The synthesis mechanism is not completely understood, but it is accepted that the continuous exposure of “fresh” area of sample help the formation of the product [12]. The theoretical study of mechano-synthesis has been difficult because the reactions occur in non-equilibrium thermodynamic conditions. Moreover, as the temperature increases during the reaction, due to the impacts and the dimensional confinement, the materials are exposed to extreme local conditions.

During the years the devices developed to perform mechanosynthesis reaction have changed, going from the early pestle and mortar to the mechanical grinding. The use of pestle and mortar is still common nowadays, but, despite it is very easy to set up and perform, the power used is not quantifiable which makes the reproducibly of the reaction difficult. In 1922 Andrew Szegvai invented the first ball milling apparatus and the following year Retsch [72] invented the first motorized ball milling. Only in 1961 the Fritsch company developed the first motorized planetary ball mill (Figure 2.5-1 left); this was a great achievement for the studies in mechanochemistry. The early grinding process worked only with the impact of the sphere (made of ceramic or inox steel) and the energy was not very high, and so the advent of the planetary ball mill allows to obtain higher energy impacts. This is obtained thanks to the simultaneous opposite circular movement of the jars respect to the platform (Figure 3.1-1 right). This technique allows very high milling energies and permit to obtain a high level of grinding also for hard and abrasive materials. Nowadays, electrically-powered ball milling is predominantly used in mechanochemical synthesis; the sealing of the jars could be airtight so there is the possibility to work under inert atmosphere filling the jars in an inert glovebox. The jars are usually made of high-hardness materials like agate, zirconia or corundum, but stainless steel is also used. Also, plastic jars can be used in particular conditions.

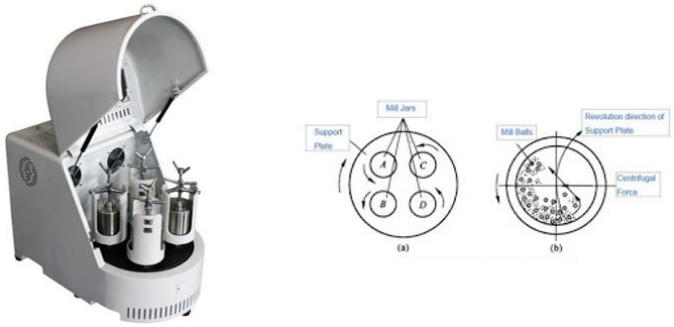

Figure 2.5-1: planetary ball milling with jars (left) and a schematic representation of the movements of the entire mill (right a) and grinding process in the jar with balls (right b).

The mill used in the present work, is a FRITSCH Mini-Mill PULVERISETTE 23, which has a spherical jar that guarantees a perfect mix and homogenization of the powders (Figure 2.5-2).

Figure 2.5-2: photo of FRITSCH Mini-Mill PULVERISETTE 23 used in this work with a steel jar.

The recognition of the mechanochemistry has started in 1929 with Wilhelm Ostwal and then Flavitsky in 1949 used a mechanochemical method to identify specific anion and cationic species [73]. The mechanochemistry applied to the synthesis of compound developed significantly in ’80s and ‘90s especially in the molecular mechanochemistry of co-crystallization [74, 75, 76]. Only during the twenty-first century it has been used for organic reactions and with these also metal-organic and supramolecular synthesis have broadened the type of reactions performed [77, 78].

Focusing on the world of the mechanochemistry applied to inorganic chemistry, MOFs (metal-organic-frameworks) have attracted the attention of the research community in the last years, and, together to the hybrid perovskites, are the most similar families of compounds to the formate studied in this work. In fact, the synthesis of MOFs requires strong reactions conditions such hydrothermal or solvothermal techniques, large amount of organic solvents and long reaction time.

Synthesis conducted with mechanochemical methods, can be performed at room temperature (or without extra heat), avoiding extra solvents and requiring from 10 to 60 minutes. As precursors for the reactions, metal oxides can be used. For example ZnO is rarely used as reagent for the synthesis in solution due to the poor solubility in organic solvents, but in mechanochemistry it is employed as precursors to obtain zeolite imidazolate frameworks (ZIFs) [65] a large family of MOFs compounds with high thermal and chemical stability formed by tetrahedral metal ions connected through imidazolate molecules [66]. In 2007 James and co-workers reported for the first time the synthesis of microporus MOFs only by grinding for 10 minutes isonicotinic acid and copper(II) acetate monohydrate; the obtained product was then heated to eliminate water and acetic acid to leave the pores empty in the structure [77]. LAG was employed in 2009 by the Fábián's group for the synthesis of coordination polymers using ZnO and fumaric acid, giving the possibility to obtain the product with one, two or three dimensions framework as the solvent changes from water, methanol or ethanol [79].

For what concerns more deeply the field of the hybrid perovskites, the synthesis condition of the well-known $CH_3NH_3PbI_3$ plays an important role in the physical and chemical properties of the material [80]. In general, to obtain $MAPbI_3$ (MA = methyl-ammonium cation) different approaches can be used, such as solvothermal, high temperatures, solid state reactions, chemical and physical vapour deposition, mechanochemical reactions, single crystal growth from a melt or solutions- based methods [67, 81]. In some cases, mild chemistry approach have been adopted [82, 83] and in these cases, the grinding of appropriate precursors allows to obtain more efficient homogenization of the starting mixture, but the process still requires a thermal annealing step to get the pure phase. In 2015 J. Lewinki's group reported the synthesis of $MAPbI_3$ by simply mixing a stoichiometric amount of the reagents in an electric ball mill for 30 minutes [67].

2.5.2 *Synthesis of ammonium formate compound $[NH_4][M(HCOO)_3]$ with M = Mn^{2+}, Co^{2+}, Ni^{2+}, Zn^{2+}, Cu^{2+} through mechanosynthesis*

Due to the issues noticed in the liquid synthesis of the ammonium formate compounds, we tried to apply the mechanosynthesis method. As the liquid synthesis does not require strong reaction conditions, this means that the construction of the framework is quite easy to reach. This has been confirmed by some observations during our synthesis. Firstly, we noticed that the formation of the product occurs immediately after the mixing of the two solutions, and the order of mixing of the solutions does not influence the final result. Due to these evidence, and the known possibility to synthesize halide perovskites and MOFs using the mechanochemical approach, we decided to try this new way of synthesis.

Similar compounds have been synthesized using the mechanochemical approach, for example, the photovoltaic hybrid methylammonium lead halides ($MAPbI_3$) [67].Moreover, recently different research efforts have demonstrated that this unconventional approach for the preparation of solid compounds can be successfully applied with a series of advantages with respect to the conventional solvent-based methods. For example, the mechanosynthesis can be achieved without the use of solvents providing an environmentally sustainable route, scalable and with limited costs. Hence, we applied mechanochemistry to the synthesis of compounds with general formula $[NH_4][M(HCOO)_3]$ M = Mn^{2+}, Co^{2+}, Cu^{2+}, Zn^{2+}, Ni^{2+} .

As the general formula of the ammonium formate is $[NH_4][M(HCOO)_3]$, the easiest reagents that could be employed are NH_4HCOO (ammonium formate) and $M(HCOO)_2$ x $2H_2O$ (M = Mn^{2+}, Cu^{2+}, Co^{2+}, Zn^{2+}, Ni^{2+}) (general metal formate) in stoichiometric amount (Figure 2.5.2-1).

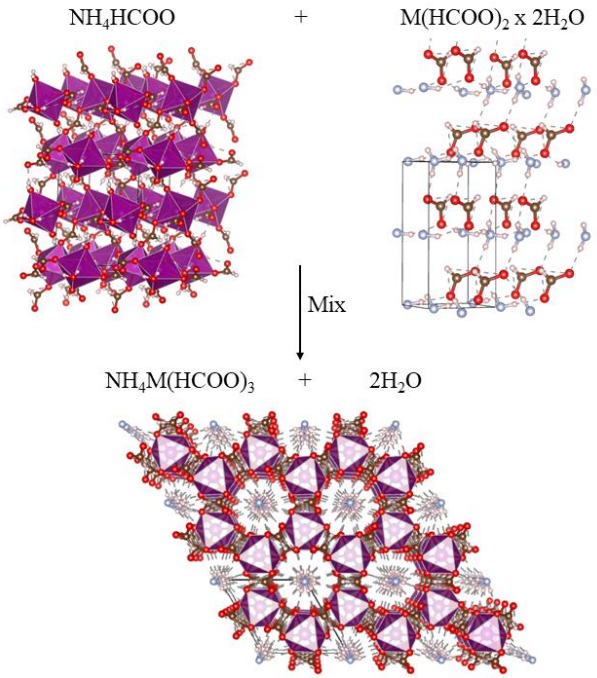

Figure 2.5.2-1: schematic representation of the mechanochemical reaction between NH_4HCOO and $Mn(HCOO)_2$. Legend of atoms: brown = C; blue = N; red = O; pale pink = H; pink = Mn.

The first attempt of synthesis has been made using the reagents without any pre-treatment; the time and the energy were arbitrary, considering the previous experiments done on similar compounds using the same mill [25].

The reaction has been done by using stoichiometric amount of the reagents and mixing them in the jar for 5 minutes at 40 Hz. The PXRD collected with the Thermo X'TRA diffractometer after this grinding confirms the presence of the product. Synthesis performed increasing the grinding time did not show an increase of desired product. In Figure 2.5.2-2 are reported the PXRD patterns of the reaction with NH_4HCOO and $Mn(HCOO)_2 \times 2H_2O$; the first experimental diffractogram from the bottom (orange colour) has been recorder after 5 session of grinding of 5 min at 40 Hz each, the second after two more grinding, in the same conditions (light blue colour).

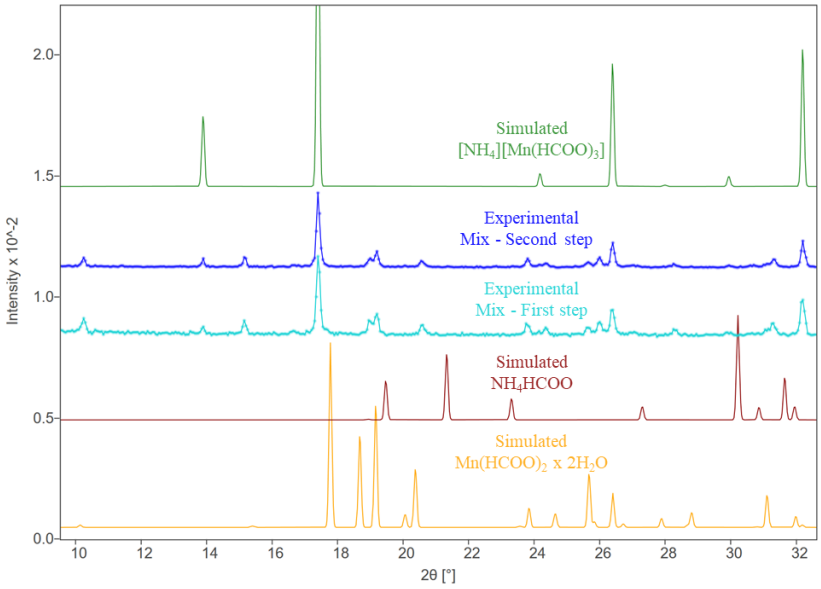

Figure 2.5.2-2: calculated and experimental PXRD patterns for the reaction with NH_4HCOO and $Mn(HCOO)_2 \times 2H_2O$. PXRD patterns were collected using Thermo X'TRA diffractometer.

In order to determine the role of the absorbed water in the synthesis process all reagent were treated in oven before the mechanosynthesis. Figure 2.5.2-3 shows the sequence of experimental PXRD collected during the synthesis of $[NH_4][Mn(HCOO)_3]$ after having pre-treated the reagents for 40 min at 80°C; the first pattern is collected after 3 times by 5 min of grinding at 40 Hz, the second after two more 5 min grindings at 40 Hz and the third after one more 5 min at 40 Hz. It is possible to observe that the pre-treatment of the reagents is useful to promote the reaction, in fact by increasing the grinding time, the peaks that belongs to the reagents decrease in intensity. The grinding time of the two syntheses, with and without pre-treatment, are very similar and it is easy to observe that the pre-treatment helps the formation of the product.

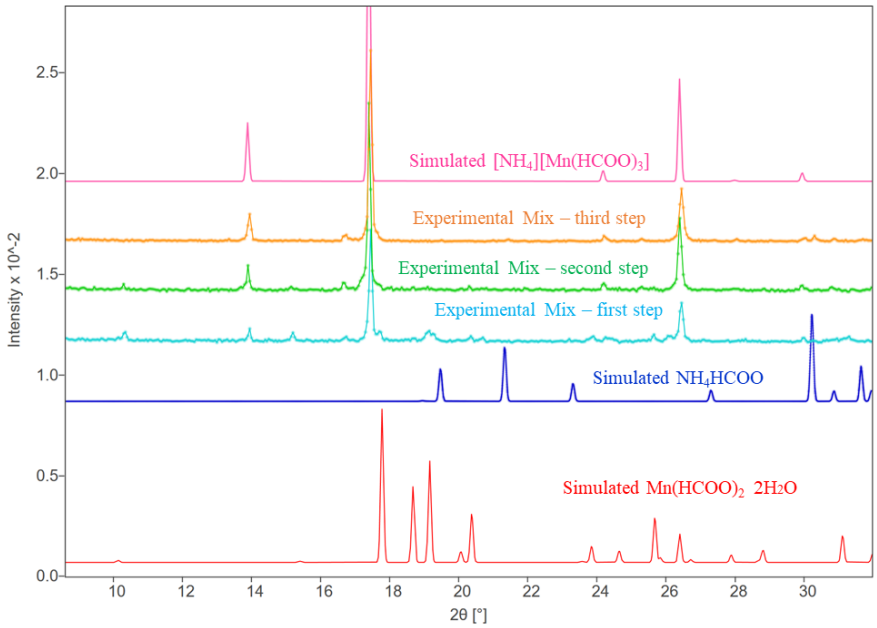

Figure 2.5.2-3: PXRD patterns for the synthesis of $[NH_4][Mn(HCOO)_3]$ conducted in three steps and simulated patterns of ammonium formate, manganese formate and $[NH_4][M(HCOO)_3]$. PXRD patterns were collected using Thermo X'TRA diffractometer.

We observed that the successful mechanosynthesis of the different ammonium formate compounds (AMF) is closely related to the relative content of adsorbed water in the reactants. We noticed that being both the starting reagents hygroscopic, the mechanical treatment without the pre-heating in oven at 353K of the starting reagents did not provide the successful synthesis of the AMF and residual amounts of starting reagents are still present even after prolonged sessions of mechanosynthesis.

This is partially explained by the lack of the 1:1 molar ratio necessary to assure the correct stoichiometry. Nevertheless, the pre-heating process reduces mechanosynthesis reaction time for all the compositions explored. The role of the absorbed water in defining the conditions in terms of energy and time required for the solid state synthesis via milling of hybrid organic-inorganic materials was addressed by D. Tsvetkov *et al.* [81]. The authors reported that during the grinding for the formation of $CsPbI_3$ a certain percent of adsorbed water constitute a favourable condition for the interaction of the starting materials CsI and PbI_2. In that case, the yield incremented as a function of the degree of humidity.

Conversely, the synthesis of the formate compounds is strongly hindered by the presence of adsorbed water and heat treatment aimed to dry the $HCOONH_4$ and $M(HCOO)_2 \times 2H_2O$ powders is required to obtain a high yield in a reasonable milling duration.

After having establish that the absorbed water is detrimental for the formation of the product, the following natural step is to investigate the role of the crystallization water present in the reagents. The role of water, in ruling the evolution of the mechanosynthesis, is particularly evident considering that the decomposition temperature of the hydrated metal formates correlates with the time necessary for the complete mechanosynthesis in all the investigated AMF compounds.

As illustrated in Figure 2.5.2-4a the milling time required for the complete reaction span from few minutes for Cu^{2+} to 125 min for Ni^{2+} with an exponential dependence with the dehydration temperature of $M(HCOO)_2 \cdot 2H_2O$ precursor [71, 84]. Particularly, for the Cu-based compound, the milling frequency must be reduced from 40Hz to 20Hz in order to avoid the melting of the mixture and the consequent failure of the synthesis process. Thus, the rate-limiting step, likely ruling the kinetics of the reaction, is related to the removal of the crystallized water molecules in the hydrated metal formates. It is worth to stress that all the $M(HCOO)_2 \cdot 2H_2O$ compounds used are isostructural.

Typically, the orthorhombic crystal structure of hydrated metal formates possesses two independent sites for the M^{2+} ions showing the classical octahedral coordination [85]. In the first site, the metal ion shows close interactions with oxygen from six formate groups whereas in the second one the coordination is completed with the oxygen of four water molecules. The metal sites surrounded by only formate ligands are linked by *anti-anti* arrays whereas the units involving the water molecules show *sin-anti* arrangement as evidenced in Figure 2.5.2-4b.

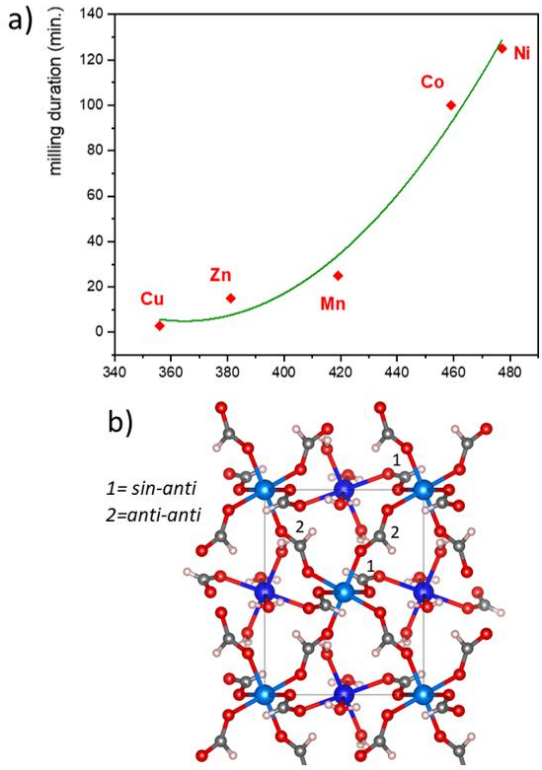

Figure 2.5.2-4: a) milling duration versus metal formate de-hydration temperature for the synthesis of $[NH_4][M(HCOO)_3]$. b) perspective view of the orthorhombic structure of $M(HCOO)_2\ 2H_2O$ compounds. Dark and bright blue spheres indicate the two symmetrically independent metal sites showing a different environment. The dark blue site is linked with four water molecules and is connected with other sites with sin-anti mode of formate ligand.

The dehydration process promoted by the mechanosynthesis induces the substitution of the water molecules in the coordination sphere of the M^{2+} ions with the formate ions provided by NH_4COOH. The increased number of ligands available to connect the different metal sites contributes to the anionic framework formation characterized by channels accommodating the NH_4^+ cations.

The construction of hexagonal cavities of the AMF constituted with *anti-anti* bridging of the formates groups requires the global rearrangement of the metal formate network with the breaking of selected M^{2+}-O interactions. Hence, the critical step is represented by the endothermic transformation of the hydrated metal formates, and the thermal stability of such reactants determines the milling duration. In this context the presence of absorbed water obviously inhibits the dehydration process of the metal formates.

Interestingly, the relation between the mechanosynthesis time and the metal specie corresponds to the Irving-Williams series [86]. This classical sequence represents the trend of the M^{2+} metals in relations to crystal field theory and provide a plausible explanation for the different thermal stability of the hydrated metal formates. As pointed out in several mechanosynthesis studies [87] the increase of the vibration frequency corresponds to a sensible decrease of the milling time.

Nevertheless, in formate-based compounds, the increment of the vibration frequency does not allow for a fine control of the energy required to promote the mechanosynthesis avoiding the melting of the reactive powders. This is particularly evident for the formation of $[NH_4][Cu(HCOO)_3]$, being $Cu(HCOO)_2$ very sensitive to the experimental conditions. The role of humidity and crystallization water in deciding the successful mechanosynthesis of hybrid materials has received increasing attention [88].

Dehydration processes promoted by mechanosynthesis are described as a useful step to the readily establishment of multidimensional coordination polymers through polymerization of small molecular units [89]. By adopting mechanochemical methods, the hydration or dehydration of hybrid materials can be rationally conceived through the control of the degree of humidity.

The different AMFs synthetized by the novel mechanosynthesis process were thoroughly characterized by structural, thermal, and microstructural analyses. For each composition obtained by mechanical milling PXRD measurements indicated the presence of the hexagonal hybrid MOF as single phase except for the Cu^{2+} variant. In the latter case we obtained the expected orthorhombic phase featuring the AMF combination with Cu^{2+} [70]. The crystal structure of this compound is characterized by a distorted lattice displaying pseudo-hexagonal cavities where NH_4^+ are distributed. This distorted framework is originated by the strong Jahn-Teller distortion of the Cu^{2+}. Figures 2.5.2-5a-b reports the crystal structures corresponding to M^{2+}=Mn, Ni, Co, Zn and M^{2+}=Cu respectively.

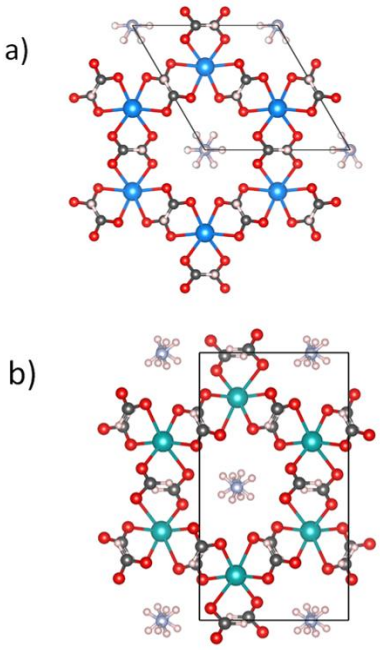

Figure 2.5.2-5 a) View along the c axis of the hexagonal structure of $[NH_4]M(HCOO)_3$ M= Mn,Co,Zn and Ni. b) View along the c axis of the orthorhombic structure of $[NH_4][Cu(HCOO)_3]$.

Rietveld plots for the polycrystalline product obtained are reported in Figure 2.5.2-6 and in Table 2.5.2-1 are reported the crystal data obtained by refining all the structural parameters comprising atomic coordinates and the atomic displacement parameters (ADP)(see Experimental Methods Table 7.9-1, 7.9-2, 7.9-3, 7.9-4). Crystal data of $[NH_4][Mn(HCOO)_3]$ differently to what set for the other compounds, was obtained by a Le Bail fitting of the diffraction data. As already remarked in literature [64], the Mn based compound is unstable and therefore the collection of high resolution diffraction data for Rietveld refinement was not possible.

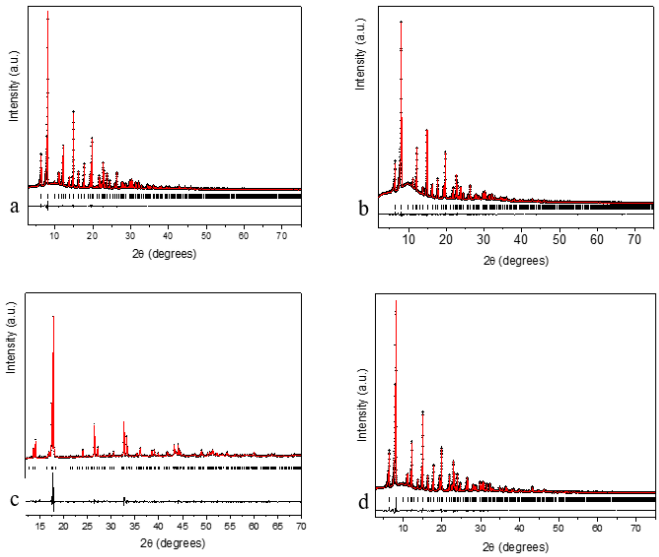

Figure 2.5.2-6: a) Rietlved plot of the diffraction data collected with Cu Kα source for the [NH4][Cu(HCOO)3]. b)Rietlved plot of the diffraction data collected with Mo Kα1 source in transmission geometry for the NH4Co(HCOO)3. c) Rietlved plot of the diffraction data collected with Mo Kα1 source in transmission geometry for the NH4Zn(HCOO)3, d) Rietlved plot of the diffraction data collected with Mo Kα1 source in transmission geometry for the NH4Ni(HCOO)3. For all panels Black crosses, red line and blue line indicates the observed, calculated and difference data respectively, whereas the tick marks indicate the Bragg position of the main phase.

Table 2.5.2-1: crystal data for [NH4][M(HCOO)3] with M=Mn, Ni, Co, Zn , Cu.

M^{2+}	Mn	Zn	Co	Ni	Cu
Space Group	$P6_322$	$P6_322$	$P6_322$	$P6_322$	$P2_12_12_1$
System	hexagonal	hexagonal	hexagonal	hexagonal	orthorhombic
Z	2	2	2	2	4
a (Å)	7.355(8)	7.32098(1)	7.30467(3)	7.27439(2)	7.1732(4)
b (Å)	7.355(8)	7.32098(1)	7.30467(3)	7.27439(2)	12.9562(8)
c (Å)	8.480(2)	8.1675(7)	8.1849(1)	8.05852(4)	8.1475(6)
α β γ (°)	90 90 120	90 90 120	90 90 120	90 90 120	90 90 90
V(Å^3)	397.3599	378.578(7)	379.630(4)	368.596(6)	757.21(4)
Density (g/A^3)	0.90	1.95	1.89	1.94	1.90
source	Cu Kα	Mo Kα1	Mo Kα1	Mo Kα1	Cu Kα
reflections		200	136	227	126
parameters		15	15	15	13
Rp, Rwp (%)	9.23 12.23	3.07 2.37	1.71, 2.23	2.09 2.33	7.19 9.45

In Figure 2.5.2-7a are graphically reported the cell parameters of the compounds to better understand the correlation between ionic radii of the metal and cell parameters. The panel shown in Figure 2.5.2-7b illustrates the M-O bond lengths of regular octahedral environment for hexagonal structures. The distorted coordination the Cu^{2+} is characterized by four basal Cu-O bond lengths of ~ 1.98 Å and two apical bonds lengths of ~2.4 Å.

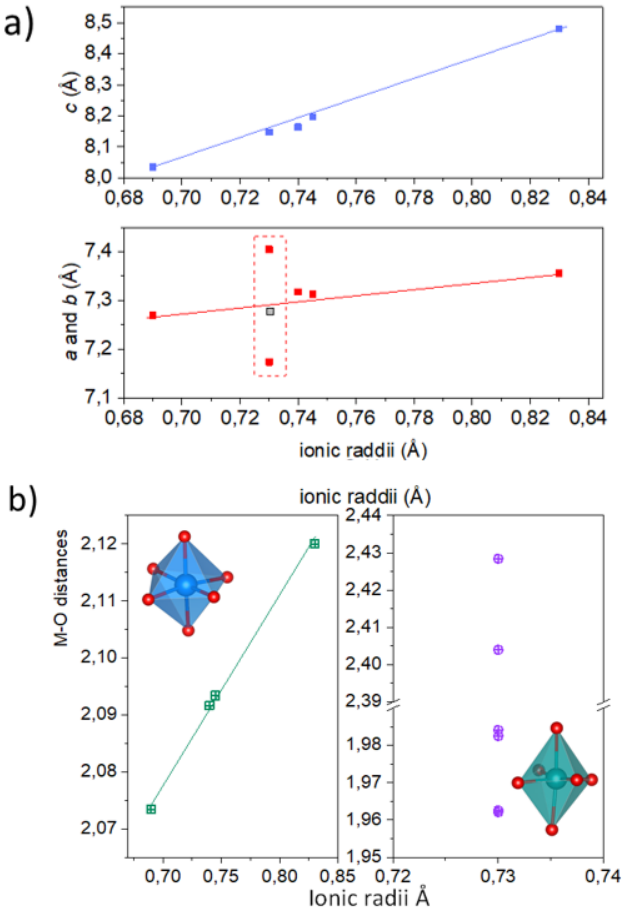

Figure 2.5.2-7: a) unit cell constants obtained from the Rietveld refinements plotted against the ionic radii of each M^{2+} ion (the series is Ni Cu Zn Co Mn); the dotted lines highlight the unit cell parameters of the distorted Cu-based crystal structure transformed by applying the matrix reported (bottom), the grey symbol indicates the average value. The new unit cell constants a_m b_m and b_m, calculated by applying thematrix, defines a monoclinic lattice showing γ angle of 118° with pseudo-hexagonal symmetry. b) M-O distances for the hexagonal (left) and orthorhombic (right) symmetry versus ionic radii of the divalent M^{2+} ions. The size of the symbols exceeds the e.d.s of the cell parameters.

The lattice constants reported in Table 2.5.2-2 of the hexagonal crystal structures, whose values are in agreement with those previously published, increase as the ionic radii of the divalent metal increases (we used the values for each divalent M^{2+} ion appeared in the Shannon tables [90] and summarized in Table 3.2-2).

Table 2.5.2-2: Ionic radius for the M^{2+} ions from the Shannon-Prewitt Crystal Radii tables.

M^{2+}	Ionic radius (Å)
Ni	0,69
Cu	0,73
Zn	0,74
Co	0,745
Mn	0,83

To compare the unit cell constants of the Cu^{2+} compound with the rest of AMFs we transformed the unit cell by applying the conversion matrix indicated below.

$$\begin{bmatrix} a_m \\ b_m \\ c_m \end{bmatrix} = \begin{bmatrix} -1 & 0 & 0 \\ 1/2 & -1/2 & 0 \\ 0 & 0 & 1 \end{bmatrix} \begin{bmatrix} a \\ b \\ c \end{bmatrix}$$

Table 2.5.2-3 shows for the conventional orthorhombic unit cell and the calculated monoclinic cell for the $[NH_4][Cu(HCOO)_3]$. The new lattice has a pseudo-hexagonal monoclinic symmetry showing γ=118°. The panel shown in Fig. 3.2-7b illustrates the M-O bond lengths of regular octahedral environment for hexagonal structures. The distorted coordination the Cu^{2+} is characterized by four basal Cu-O bond lengths of ~ 1.98 Å and two apical bonds lengths of ~2.4 Å.

Table 2.5.2-3: unit cell constants for the conventional orthorhombic unit cell and the calculated monoclinic cell for the $[NH_4][Cu(HCOO)_3]$.

	Orthorhombic unit cell	Pseudo-hexagonal unit cell
a (Å)	7.1732	7.1732
b (Å)	12.95	7.4046
c (Å)	8.1475	8.1475
α (°)	90	90
β (°)	90	90
γ (°)	90	118.97
V (Å^3)	757.21	378.59

The ammonium compounds were also characterized by Raman spectroscopy. In Figure 2.5.2-8 the Raman spectra of selected isostructural compositions (with Mn, Co, Ni and Zn) are shown. The overall spectra is that expected for hybrid organic-inorganic formate-based frameworks [63, 60, 91]. The Co containing sample has no correspondence in literature; its spectra is intermediate between the previous ones, with a number of peaks similar to Ni and Zn samples, but with small bandwidth, as the Mn sample. The sharpness of the Raman peaks can be a sign of a better order or a higher harmonicity of the lattice. The position and attribution of the Raman bands for the four samples is reported in Table 2.5.2-4a and 2.5.2-4b. The attribution was made in agreement with the literature [63, 60, 91]: some of the bands are readily assigned as their position corresponds to the wavenumbers typical of formate and ammonium ions [91, 92]. It is possible to observe the most intense peaks in the region 1300-1400 cm^{-1}, due to the C-O symmetric stretching mode (ν2) of formate ions. The presence of multiple peaks in this region is due to the lowering of the formate ions symmetry, from C2v to C2. In some cases, a further splitting can be caused by the presence of non-equivalent formate units in the structure, as has been observed for Mg-frameworks [91] and in the Mn-framework shown in this work. Other typical formate vibrations are visible in the regions 750-810 cm^{-1} (COO symmetric deformation, ν3), 1050-1070 cm^{-1} (ν6), 1570-1595 cm^{-1} (C-O anti-symmetric stretching, ν4). In the high wavenumber region, 2600-3200 cm^{-1}, the strongest peak is attributed to the C-H stretching (ν1) of formate ions. The wavenumber of this mode increases with the lowering of C-H distance [91] and this is well reflected by the increase of the ionic radius of the metal ions (Mn^{2+}> Co^{2+}> Zn^{2+}> Ni^{2+}). The same trend is shown by the O-C-O bending mode (ν3), even in presence of splitting. In the high wavenumber region, different weaker vibrations

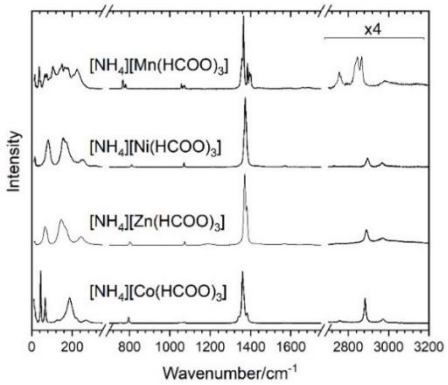

Figure 2.5.2-8: Raman spectra of the AFM obtained by mechanosynthesis. The high-wavenumbers part is magnified X4.

due to the N-H symmetric and antisymmetric stretching modes (ν1 and ν3) of ammonium ions are visible. The ammonium N-H symmetric and antisymmetric bending modes are observed in the ranges 1430-1450 (ν3) and 1600-1700 (ν2) cm^{-1}. The splitting of the ν2 modes indicates the lowering of the NH_4^+ symmetry to D3 due to the crystal field. The ammonium ion vibrational modes are generally very weak in the Raman spectra, and indeed some of them are barely visible or not detected (especially in the Co containing sample). No evident Raman modes characteristic of water or OH^- ions have been detected, even by extending the Raman analysis up to 4000 cm^{-1} with low-wavelength excitations (532 nm), which are more efficient for the analysis in the high-wavenumber region.

In the low wavenumber region, between 15 and 330 cm^{-1}, a large number of overlapping bands is observed. The latter region is typical of translations and librations of the ions (metals, formate and ammonium). The different contributions are very difficult to discriminate. Librations have the largest Raman signals and are expected in the 130-220 cm^{-1} ($HCOO^-$) and 300-480 cm^{-1} (NH_4^+) regions. The translations of the divalent metal ions usually have very low Raman signals, often not visible in the Raman spectra. Detailed attempts to attribute the different bands in some MOF are present in literature [63, 60, 91]. A very small Raman peak is present in all the samples at 2140 cm^{-1} (not reported in Fig. 4), usually attributed to CO adsorbed on the MOF.

Table 2.5.2-4a: Wavenumbers (cm^{-1}) of the Raman peaks of the four perovskite samples and their attributions.

$[NH_4][Ni(HCOO)_3]$		$[NH_4][Co(HCOO)_3]$		$[NH_4][Zn(HCOO)_3]$		$[NH_4][Mn(HCOO)_3]$		Attribution
position	(cm^{-1})	position	(cm^{-1})	position	(cm^{-1})	position	(cm^{-1})	
15.0	m	16.1	w	15.7	s	14.6	m	NH_4^+ and $HCOO^-$ translations and librations
						37.0	s	
		44.2	vs			44.5	w	
						58.2	w-sh	
		66.6	s	63.6	s	64.7	m	
				73.0	m-sh	74.1	m	
80.7	s					87.3	w-sh	
		91.6	vw			105.0	s	
		125.9	w	119.9	w-sh	114.6	m-sh	
						140.6	m-sh	
155.5	s	176.9	m-sh	145.1	s	150.8	s	
173.8	s	188.8	s	169.9	m-sh	163.3	s	
187.3	m-sh	204.5	m-sh			178.7	s	
						203.4	m.sh	
		222.1	w			223.5	s	
251.3	m	269.9	w	244.8	m	237.9	m-sh	
				275.7	w-sh			
314.2	vw			322.0	vw			

Table 2.5.2-4b: Wavenumbers (cm^{-1}) of the Raman peaks of the four perovskite samples and their attributions.

$[NH_4][Ni(HCOO)_3]$	$[NH_4][Co(HCOO)_3]$	$[NH_4][Zn(HCOO)_3]$	$[NH_4][Mn(HCOO)_3]$	Attribution
position (cm^{-1})	position (cm^{-1})	position (cm^{-1})	position (cm^{-1})	
	755.0 vw	801.3 w	767.4 w	$\nu_3(HCOO^-)$ sym. def. COO
810.8 w	796.2 w	804.2 w	780.7 w	
	1048.5 vw		1057.8 w	$\nu_6(HCOO^-)$
			1069.0 vw	
1070.7 w	1072.9 vw	1073.6 w	1073.2 w	
1348.5 vw-sh	1340.8 w	1345.2 w	1356.9 m	ν_2 ($HCOO^-$) str. sym. CO
1367.2 m-sh				
1373.1 vs	1359.9 vs	1371.2 vs	1365.4 vs	
1378.3 m-sh	1366.6 m-sh	1382.2 s	1384.6 m	ν_5 ($HCOO^-$)
	1382.5 w		1394.4 m	
			1401.4 m	
1436.7 vw		1435.6 vw	1446.1 vw	ν_4 NH_4^+
1569.6 w	1594.9 vw	1569.4 w	1569.0 vw	$\nu_4(HCOO^-)$ as. str. CO
1663.5 vw		1605.6 vw	1656.2 vw	ν_2 NH_4^+
		1680.6 vw	1686.1 vw	
	2658.9 vw			ν_1 and ν_3 NH_4^+ str. NH
	2757.6 vw	2744.7 vw	2757.5 vw	
	2785.7 vw		2842.8 w	
2895.6 w	2883.6 w	2890.8 w	2866.9 w	ν_1 (HCOO-) str. CH
2969.0 vw	2971.3 vw	2946.5 vw-sh	2979.7 vw	ν_1 and ν_3 NH_4^+ str. NH
	3030.3 vw	2970.9 vw	3028.1 vw-sh	
		3014.8 vw-sh	3132.0 vw-sh	
		3139.0 vw-sh	3221.5 vw-sh	

The new mechanochemical synthesized compounds were also characterized by thermal analysis with DSC and TGA. The TGA analysis, depicted in Figure 2.5.2-9 shows for all the compounds a subtle decrement of weight around 373K that is attributed to the removal of the adsorbed water [93, 94, 61]. We noticed, in all the composition explored, two main weight losses.

The first decomposition step is related to the formation of the metal formate $M(HCOO)_2$ [69, 61] from the AMF structure, whereas the second steps is related to the decomposition into the final metal oxides. TGA analysis for the AMF compound with Cu provides a singular thermal decomposition with a drop of weight corresponding to the 50% of the initial mass. This could indicate a different decomposition path with respect the rest of AMFs analysed.

Figure 2.5.2-9: TGA traces for the compounds obtained via mechanosynthesis.

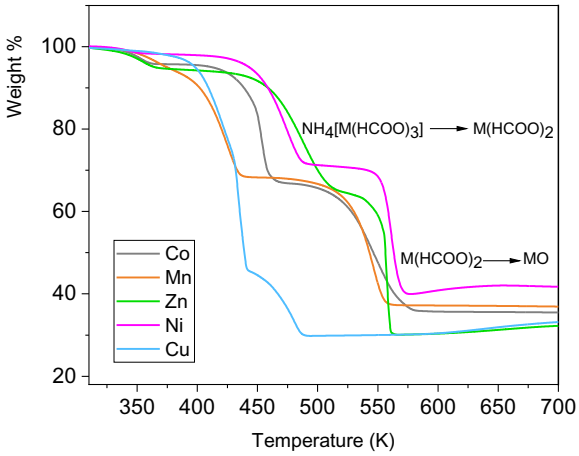

The DSC analysis, depicted in Figure 2.5.2-10 a) and b) show for all the compounds a peak around 373 K (362 for Co, 372 for Mn, 333 for Zn and 367 K for Ni) that is attributed to the removal of adsorbed water [93, 94, 61] together with sharp endothermic peaks corresponding to the different decomposition steps indicated by TGA. In the case of Mn and Ni the two decrements of weight in TGA are closely contiguous and the corresponding DSC traces reveals a single thermal event probably related to the concomitant transformations. When the two decomposition steps show well separated temperatures, two distinct DSC peaks are observed as in the case of Co and Mn. DSC analysis for the AFM compound with Cu provides a singular thermal evolution with an intense and sharp endothermic peak preceding a second strong exothermic thermal event, that, as observed in the TGA traces, could indicate a different decomposition path from the other AFMs analysed compounds.

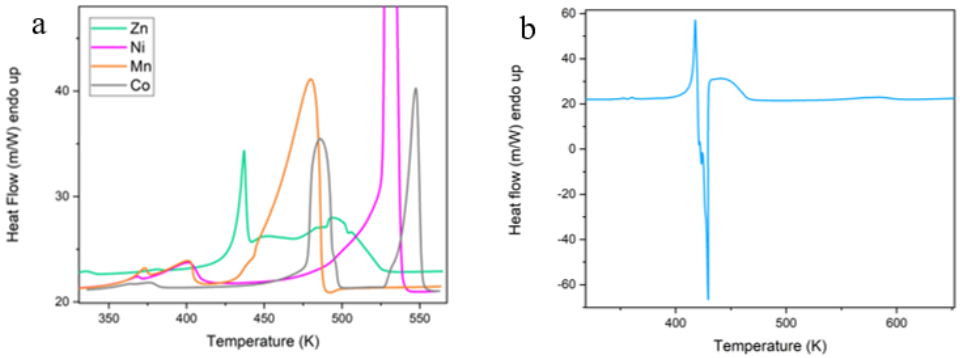

Figure 2.5.2-10: a) DSC of the ammonium-formate compounds obtained via mechanosynthesis with M = Mn^{2+}, Zn^{2+}, Co^{2+}, Ni^{2+}; b) DSc of the ammonium-formate compound with M = Cu^{2+}.

The AMF phases present a good degree of crystallinity as indicated by the PXRD measurements performed both in reflection and transmission geometries. To ascertain the impact of milling duration on the crystal morphology, SEM micrographs) were collected on $[NH_4][Zn(HCOO)_3]$ (Figure 2.5.2-11 a), b)) and $[NH_4][Co(HCOO)_3]$ (Figure 2.5.2-11 c) and d)) obtained after 15 and 100 minutes of milling treatments respectively. We note that, under vacuum and electron beam, the crystalline phases tend to modify their habits seemingly indicating the occurrence of degradation processes. It is therefore worth to highlight that MOF are very sensitive to low pressure conditions sometimes inducing collapse of the porous frameworks [95]. As it is evidenced in Figure 2.5.2-11 a) and b), the Zn-based compound is characterized by aggregated rounded particles with dimensions spreading from few microns to tens of nanometres. Conversely, $[NH_4][Co(HCOO)_3]$ is composed by squared crystals with regular shapes and larger polydispersity. Since the vibrational energy was unvaried and the milling was interrupted after 5 minutes for each session it is reasonable to suppose that the different morphology is related to the different behaviour of the metal formates in reacting under mechanical impulse. Further studies aimed to characterize the mechanical synthesis by in-situ XRD or micro-Raman experiments could unravel the conversion mechanism of the metal formates.

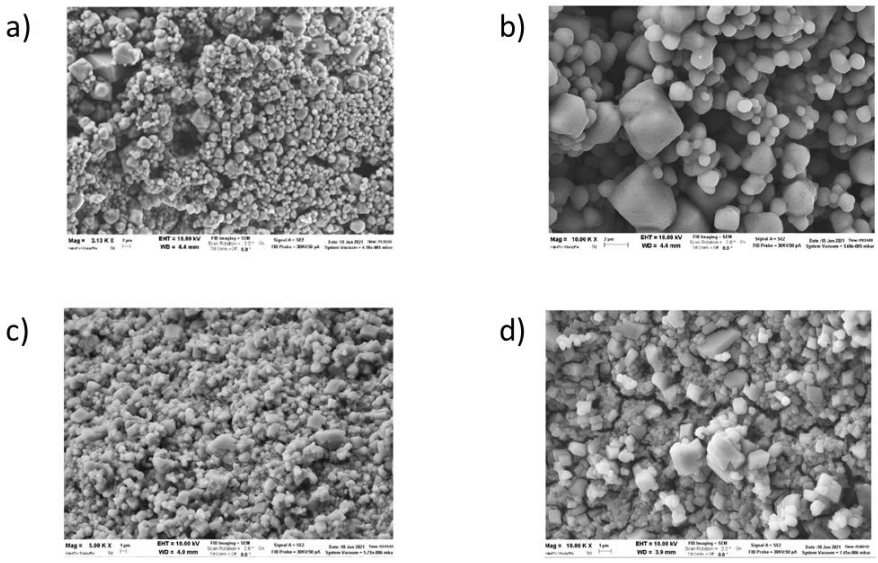

Figure 2.5.2-11: a), b) SEM images collected on $[NH_4][Zn(HCOO)_3]$; c), d) SEM images collected on $[NH_4][Co(HCOO)_3]$.

In conclusion, we developed a new strategy of synthesis for the ammonium-metal formate compounds via mechanochemical approach; the synthesis can be easily performed starting from the ammonium and hydrated metal formates. Our studies demonstrated that the absorbed water can negatively influence the synthesis, in fact, we noticed a correlation between the milling time and the dehydration temperature of the metal-formate hydrate used as reagents. Our diffraction experiments and with the SEM analysis revealed a great grade of crystallinity of the samples and the absence of lattice strains. This new approach to synthesize the AMF compounds can be considered as a straightforward synthetic strategy pointing out the opportunity to design novel formate-based complex perovskite-like hybrids encompassing electric and magnetic properties. Moreover, this solvent-free method can be an alternative to the classical liquid synthesis employed for the synthesis of formate-based framework where the solubility of the metal salt or the inclusion of the solvent in the cavity of the structure could be a limit.

2.6 Attempts of polarization on $[NH_4][M(HCOO)_3]$, M = Mn^{2+}, Fe^{2+}, Co^{2+}

Due to the ferroelectric behaviour found for crystals of ammonium-formate family [61, 62], we tried to perform attempts of polarization of the powder, in particular of the compounds with M = Mn^{2+}, Fe^{2+}, Co^{2+} and Ni^{2+}. Test were performed both on the samples coming from the liquid synthesis and from the mechanosynthesis.

In the first case the powders were dried under N_2 flux and then pressed to make tablets, in the second case the powders coming from the mechanosynthesis were just pressed to make suitable tablets. Test were performed both at RT and low temperature after the metallization of the tablets with Ag paste. Table 2.6-1 reports the resistance value found for the compounds at RT and at LT.

Table 2.6-1: resistance found at LT and RT for the ammonium-formate compounds with M= Mn^{2+}, Fe^{2+}, Co^{2+} and Ni^{2+}.

Compound	R RT (Ω)	R LT (Ω)
$[NH_4][Mn(HCOO)_3]$	10^{10}	10^9 (100 K)
$[NH_4][Co(HCOO)_3]$	10^5	-
$[NH_4][Ni(HCOO)_3]$	10^6	10^9 (100 K)
$[NH_4][Fe(HCOO)_3]$	10^6	10^{11} (80 K)

During our attempts we observed a conductive behaviour for $[NH_4][Fe(HCOO)_3]$ at RT with R ~ 10^6 – 10^7 Ω that disappear at LT where, instead, it shows a dielectric behaviour and an increasing of the resistance (R ~ 10^9 – 10^{10}). As shown in Figure 2.6-1a, at RT current is proportional to the applied voltage, and, following the Ohm's law (I = V/R), with the increasing of the voltage, the current increase, showing a conductive behaviour of that sample. On the other hand, at 78 K, as the voltage is constant in time (Figure 2.6-1b), the resulting current is proportional to the variation of the voltage; this indicates a predominantly capacitor behaviour. Note that also at RT capacitor behaviour is present, but the conductive one is higher and dominates (Figure 2.6-1a).

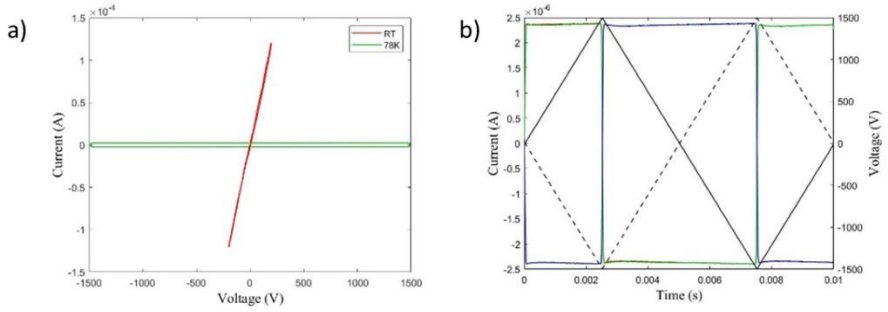

Figure 2.6-1: ferroelectric measurements on $[NH_4][Fe(HCOO)_3]$; 2a) current VS voltage recorded at RT and 78 K, 2b) current VS time at 78 K.

Generally, the increasing of the resistance comes with the increasing of the applied tension, this means that the conductive phenomenon appears at low tension (0.5 V – some volts) and does not increase linearly with the applied tension. Moreover, after the cooling of the sample at 78 K and the heating at RT, the resistance drastically decreased till 10^3 Ω with the formation of condensation on the sample; after four days the resistance assumes the initial value.

Unfortunately, we have not been able to observe polarization on our samples; in our opinion this behaviour is due to the polycrystallinity of the material, also known in literature for thin films samples of MOFs [96, 97]. In fact, if a single crystal of the material has only two opposite polarizable directions, to achieve the maximum polarization the sample should be well oriented in that directions. The application of an electric field along the polar axes inverts the polarization of all the sample and it is possible to observe the characteristic hysteresis loop.

Different is the case of a polycrystalline material; in this case the domains in the grains that form the material are randomly organized (Figure 2.6-2a). Polarization can be reached usually at high temperatures by applying strong electric field (10 – 100 kV cm^{-1}). Though this process called "poling" it is not possible to orient the grains, but it is possible to orient the domains within individual grains along the field direction (Figure 2.6-2b) [97]. As seen in polycrystalline thin films [96] not just there are only two opposite polarizable directions, but also the material is polycrystalline, thus, only a small portion of the domains is polarized even after the "poling" process. The resulting macroscopic polarization is too weak or can be detected only as a limited piezoelectric response.

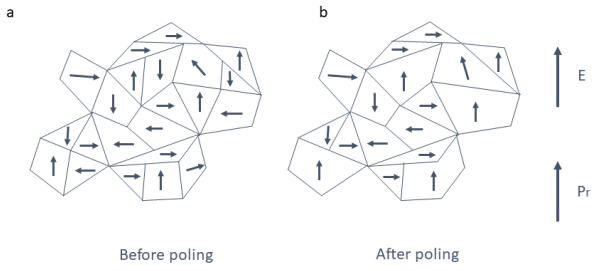

Figure 2.6.2: polycrystalline ferroelectric with random orientation of the grains. a) Before the poling process, b) after the poling process, for which the net remnant polarization is nonzero.

3 HYDRAZINUM COMPOUNDS

3.1 General description of the crystal structures

Hydrazine-formate compounds have general formula $[NH_2NH_3][M(HCOO)_3]$ with M = Mn^{2+}, Fe^{2+}, Co^{2+}, Mg^{2+}, Zn^{2+} [39, 60]. They can be found in two polymorphs: the "perovskite" and the "chiral" or "channel" structure. In both structures the metal is octahedrally coordinated with six oxygen belonging to the formate anion. Each octahedra is linked to another by the formate molecule that is bonded in *anti-anti* mode. The framework formed by the metal and the formate anions creates cavities that have different shapes depending on the type of structure (chiral or perovskite) in which the hydrazine cation ($NH_2NH_3^+$) is located and anchored to the framework by hydrogen bonds with the oxygen of the formate anions.

The chiral structure is formed by an anionic framework that generates hexagonal cavities in which the hydrazine cation is located. Chiral structures are observed for M = Co^{2+}, Mg^{2+}, Mn^{2+}, Fe^{2+}, Zn^{2+} [39, 60]. They possess a high temperature (HT) hexagonal structure with space group $P6_3$ in which the $NH_2NH_3^+$ cations in the hexagonal cavities is disordered over two positions. In the low temperature phase (LT) the $NH_2NH_3^+$ cations orders occupying only one of the two positions of the HT phase dictating symmetry reduction. The LT phase possess the $P2_12_12_1$ space group for all metals except for the Mn compound which adopt the $P2_1$ space group. The phase transition from the non-polar orthorhombic $P2_12_12_1$ to the polar hexagonal $P6_3$ occurs at different temperatures (summarized in Table 3.1-1) depending on the metal and so at room temperature each compound is present in a specific phase.

Table 3.1-1: Critical temperature (Tc) for the HT-LT transition of the chiral polymorph depending on the d-metal.

Compound	T_c (K)
$[NH_2NH_3][Co(HCOO)_3]$	380
$[NH_2NH_3][Mg(HCOO)_3]$	348
$[NH_2NH_3][Fe(HCOO)_3]$	344
$[NH_2NH_3][Mn(HCOO)_3]$	293
$[NH_2NH_3][Zn(HCOO)_3]$	365

In the cavity the hydrazine cation is anchored to the framework by various hydrogen bonds. In the HT phase all the compounds are isomorphic and the disordered hydrazinium cation is anchored by multidirectional N-H···O and N-H···N bonds; in particular, the NH_3^+-end and the NH_2-end are anchored by three and one N-H···O bond [39, 60] respectively and the strengthening of some N-H···O could play a role during the HT-LT phase transition [60]. In particular the NH_3^+-end in the Fe compound forms three strong N-H···O bonds and a weak N-H···N bond, instead for Mn there are two strong N-H···O and a weak N-H···N bond. In both the Fe and Mn compounds the NH_2-end forms three N-H···O bonds of which one strong and two weak. The bond lengths are slightly larger for Mn compared to Fe, suggesting a weaker bond between the NH_2-end in the Mn compound, which joined with the weaker H-bonds of the NH_3^+-end might explain the lower transition temperature (see Table 3.1-1). In Table 3.1-2 are summarized all the H-bonds made by $NH_2NH_3^+$ for the chiral polymorphs (space group $P6_3$) of Mn, Fe and Co. The compounds are also isomorphic in their LT structure (with the exception of the compound with manganese). In the LT phase for what concerns the NH_3^+- end, two of its N-H donors form four N-H···O bonds, whereas the last N-H donor points towards the NH_2-end ion pair, but this last deserves further investigations. On the contrary, the LT monoclinic $P2_1$ structure of Mn possess four unique hydrazinium cations that forms the H-bonds network. Of the four NH_3-NH_2^+ cations, three are ordered, instead one is disordered in three orientations. Moreover, each metal octahedra is distorted with different M-O and C-O bond lengths [60].

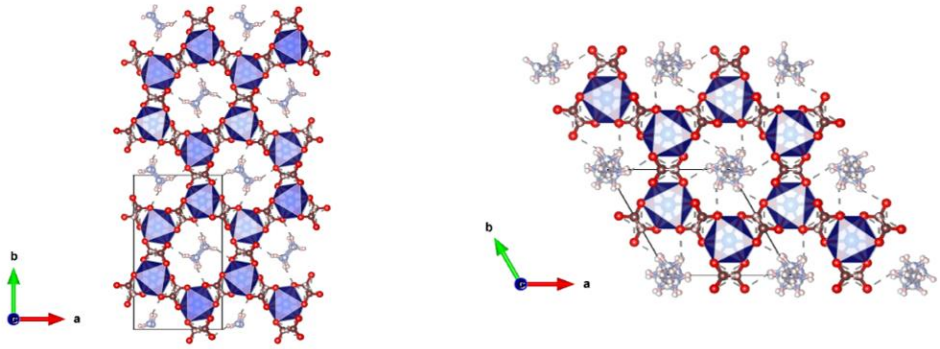

Figure 3.1-1: View along the z axis of $[NH_2NH_3][Co(HCOO)_3]$ at 290 K (left) in $P2_12_12_1$ space group and 405 K (right) in the $P6_3$ space group.

Table 3.1-2: Correlation between the H-bonds for chiral polymorph of Co, Fe, Mn at 290, 360 and 310 K respectively and their transition temperatures between the HT and LT phases.

Compound	N-H···O	N-H···N	T_g
	Number of bonds	Number of bonds	
Co [1]	6 (NH_3-end) + 2 (NH_2-end)	1	380
Fe [1]	3 (NH_3-end) + 3 (NH_2-end)	1	344
Mn [2]	2 (NH_3-end) + 3 (NH_2-end)	1	293

The compounds that are known in literature with the perovskite-like structure are $[NH_2NH_3][Mn(HCOO)_3]$, $[NH_2NH_3][Fe(HCOO)_3]$ and $[NH_2NH_3][Zn(HCOO)_3]$ [39, 60]. In all the perovskites polymorphs both at LT and HT, the structures are orthorhombic and shows a phase transition from the polar $Pna2_1$ space group at LT to the centrosymmetric *Pnma* at HT. At RT all compounds possess the $Pna2_1$ space group, and the phase transition occurs at 400, 350, 375 K for M = Mn, Fe, Zn respectively. In Figure 3.1-2 are reported the crystal structures of $[NH_2NH_3][Mn(HCOO)_3]$ at LT and HT that are isostructural to $[NH_2NH_3][Fe(HCOO)_3]$ and $[NH_2NH_3][Zn(HCOO)_3]$. The LT structure is characterized by an anionic framework of formate anion linked to each other in *anti-anti* mode; in the cavity are located the hydrazium cations anchored by several H-bonds and aligned along the longest body-diagonal of the cavity. The dimension of the cavity is different depending on the metal present in the framework, in particular the volume are 44.4 and 40.1 A^3 for Mn and Zn respectively, which are in agreement with the ionic radii trend of the metals (0.97 A for Mn and 0.87 for Zn).The NH_3^+-end anchors the $NH_2NH_3^+$ cation to the framework forming two N-H···O bonds, one strong and one weak, with the oxygen that belongs to the formate framework. The NH_2-end forms only one weak H-bond, and, as it is loosely bonded, it has more liberty motion at HT, moreover it is positioned oblique to one side of the cavity, leaving the rest available to form alternative bonds [39].

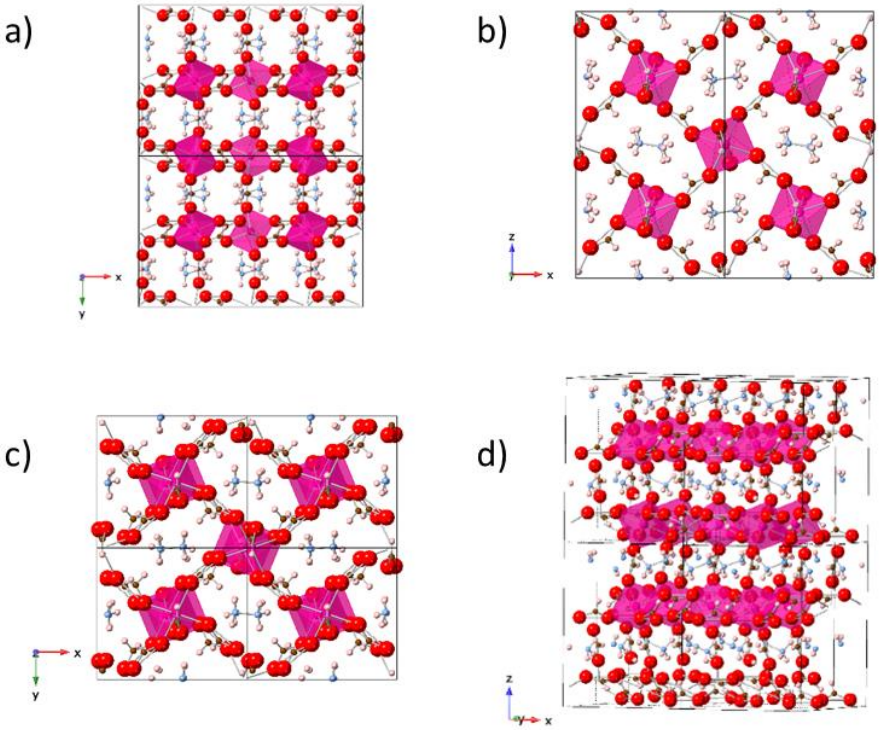

Figure 3.1-2: Crystal structure of $[NH_2NH_3][Mn(HCOO)_3]$. In a) and b) are shown the perspective view along the z and y axis respectively, at 290 K; in c)and d) are reported the structure at 400 K along the z and y axis respectively.

The transition between the LT and HT structures is due to an order-disorder transitions of the $NH_2NH_3^+$ cations. The HT phase has *Pnma* symmetry and the the mirror plane along b induces the cation disorder. In fact, the $NH_2NH_3^+$ cation possess two orientations for the NH_2-end on the two sides of the latter mirror plane. On the contrary, the NH_3-end is anchored by six N-H···O H-bonds. The fact that at HT the NH_2-end is free to move in two particular directions, instead at LT it has only one orientation, is similar to the behaviour found by Huang and co-workers for 4-Methoxyanilinium-Tetrafluoroborate-18-crown-6 for which they discover ferroelectricity due to the different orientation of the methyl group al LT [98].

S. Gao and co-workers have been the first group to synthesize the hydrazinium-formate cation with M = Mn^{2+}, Zn^{2+}, Co^{2+}, Mg^{2+} [1]. They propose a unique synthetic procedure for all the compounds using a mild chemistry approach in which a metal salt, for example $Mn(ClO_4)_2$ x $6H_2O$, is dissolved in methanol and then added to an another methanol solution obtained by mixing formic acid and an aqueous solution of hydrazine. After two days the obtained crystals are collected and washed with ethanol.

Using this procedure, they obtain compounds with Mn and Zn in the perovskite polymorph, instead Co and Mg were obtained in the chiral polymorph.

Later, A. Pikul and co-workers synthesized the chiral polymorph compounds with Mn, Fe, Zn and the perovskite polymorph with Fe [60]. They also synthesized the perovskite polymorph of Mn and Zn and a new perovskite compound with Fe using a similar procedure to the one used by S. Gao *et al.* [39], but they used as source of metal the chloride salts. To obtain the chiral polymorphs of Mn and Zn, Pikul *et al.* reported a procedure in which they use the method previously described for the other *d*-metals but replacing methanol with 1-methyl-2-pyrrolidinone. The synthesis of the chiral Fe polymorph, using only 1-methyl-2-pyrrolidinone was not successful, so the authors used as solvent a 1:1 mixture of 1-methyl-2-pyrrolidinone and methanol. From this synthesis they obtained the chiral phases of Zn and Fe with the $P2_12_12_1$ space group instead Mn with the $P6_3$ space group at RT. It is interesting to note that, as previously remarked, S.Gao and co-workers found the existence of both the perovskite and chiral polymorphs for M=Fe using their usual synthesis procedure, without employing any extra solvent.

In Table 3.1-3 are summarized the LT and HT space group for each polymorph of each compound.

Table 3.1-3: T_c and space group for the transition of the chiral and perovskites polymorphs of the hydrazine-formate compound with M = Mn, Fe, Co, Zn, Mg.

Compound	T_c (K)	LT space group	HT space group
Chiral Mn	293	$P2_1$	$P6_3$
Perovskite Mn	400	$Pna2_1$	$Pnma$
Chiral Fe	334	$P2_12_12_1$	$P6_3$
Perovskite Fe	350	$Pna2_1$	$Pnma$
Chiral Co	380	$P2_12_12_1$	$P6_3$
Chiral Zn	365	$P2_12_12_1$	$P6_3$
Perovskite Zn	350	$Pna2_1$	$Pnma$
Chiral Mg	348	$P2_12_12_1$	$P6_3$

The chiral and perovskite polymorphs have been discussed separately for clarity, but they are strongly related to each other. Literature reports that the chiral phase is obtained when the organic cation present in the cavity is small such as NH_4^+ or CH_3OH, instead when bulky and large ammine are employed (like triethylamine, dimethylamine or propylamine) the formation of porous coordination material with general formula $[M_3(HCOO)_6]\cdot$solvent (M = Mn^{2+}, Fe^{2+}, Co^{2+}, Zn^{2+}) is preferred. This structure has a diamond-like shape formed by octahedrally coordinated divalent metals [69]. The resultant framework possesses channels that are usually occupied by a solvent that be removed without damaging the crystallinity of the structure; once the solvent is removed, the cavity can be again filled by other guests molecules [98, 69]. When middle-size ammines are used, for example methylamine, dimethylamine, ethylamine or cyclotrimethyleneamine, the most stable structure is the perovskite polymorph [69]. The case of NH_2NH_3 is quite different due to its intermediate size.

The stability of organic-inorganic frameworks has been calculated by Cheetham and co-workers using the tolerance factor (TF) approach, usually applied for inorganic perovskites compounds. In those cases, the TF considers the effective radius of the components of the framework (X-site and A-site molecular group and B-site ion) and gives an idea about the tolerability by the perovskite lattice, of the match between the building blocks that constitute the framework (see Introduction Chapter). They conclude that $[NH_2NH_3][M(HCOO)_3]$ (M = Mn^{2+}, Zn^{2+}, Co^{2+}, Mg^{2+}) perovskites are stable in a range of TF = 0.81-1.0 [12, 99]. Nevertheless, the same authors observed that the experimental TF values for the hydrazine compounds are in the range of 0.814-0.845, concluding that the stability of these structures cannot be related to its TF alone [100]. Moreover, based on DFT calculations, they concluded that, due to higher contribution of vibrational entropy, the chiral polymorph becomes more stable than the perovskite one at high temperatures. For Zn, for example, the perovskite is the stable polymorph at RT due to this additional energy contribution. The study has been carried out taking as representative compounds the one with Zn and Mg, and, as the H-bonds in Mg are weaker, this leads to a lower crossover temperature, thus, at RT the compound crystallizes in the chiral polymorph. These theoretical calculations have been tested experimentally by replacing Zn^{2+} and Mg^{2+} with larger metal such Mn^{2+} and Fe^{2+} that possess weaker H-bonds[2]. But, contrary to the predictions, the synthesis results show the presence of the perovskite polymorph for both Mn and Fe at RT. the authors conclude that the vibrational entropy contribution for these compounds is too small to shift the crossover to RT or below.

Cheetham et al. [100] also suggest that small changes in reaction kinetics might control the formation of the two polymorphs. They obtained the Zn chiral polymorph by using triethylamine (TEA) as a template agent, hydrazinium monochloride as source of hydrazine and a mixture of methanol-water (1.3:1) as solvent [100].

With the aim to investigate the role of the template agent to obtain the chiral phase, Pikul and co-workers obtained the chiral phases of Mn and Fe using 1-methyl-2-pyrrolidinone and methanol as solvents. The authors report that, thanks to the higher viscosity (1.65 cp at 25°C) compared to methanol (0.54-0.59 cp at 25°C), 1-methyl-2-pyrrolidinone slow down the ion diffusion rate and facilitates the formation of the chiral polymorph. Moreover, they noticed that when the Fe chiral polymorph was left in air transforms faster than the same compound left closed in a glass container, validating the hypothesis that water vapour have an important role in the transformation [100]. They also observed that even if the Mn chiral polymorph was kept in a close container, its transformation rate was very high. They speculate that the large size of Mn^{2+} increases the channels dimension and this, joined with the higher hygroscopicity[2], might explain the faster transformation. High-pressure Raman studies confirmed the lower density of the chiral polymorph compared to perovskite, and, even under pressure, the transformation does not occur. This confirms this event is due to kinetic reasons [60].

3.2 Results

In this thesis only $[NH_2NH_3][Mn(HCOO)_3]$, $[NH_2NH_3][Fe(HCOO)_3]$ and $[NH_2NH_3][Co(HCOO)_3]$ were synthesized. We used the protocol reported by Pikul and co-workers [60]; first, an acid-base solution is prepared in a glass tube mixing 2 mL of HCOOH (98% purity) with 0.5 mL of hydrazine monohydrate in 10 mL of methanol. In a becher 2 mmol of metal salt ($MnCl_2$ x $4H_2O$, $FeCl_2$, $Co(NO_3)_2$) are dissolved in 15 ml of methanol and then gently layered on the top of the acid-base solution (see Experimental Methods). The aim of the synthesis was to prepare a powder sample, so all the precipitate was collected, filtered and washed with methanol, then dried in air.

The synthesis of $[NH_2NH_3][M(HCOO)_3]$ M = Mn^{2+}, Fe^{2+}, Co^{2+} is carried out using the above procedure; the two layered solutions are colourless/pale pink, yellow/orange and pink for Mn, Fe and Co respectively. After one day crystals were grown at the interface and on the bottom of the vessel, together with a precipitate (Figure 3.2-1).

If you are not interested in the crystals the precipitate could be obtained by simply pouring the metal solution into the acid-base solution and mixing; the precipitation is immediate.

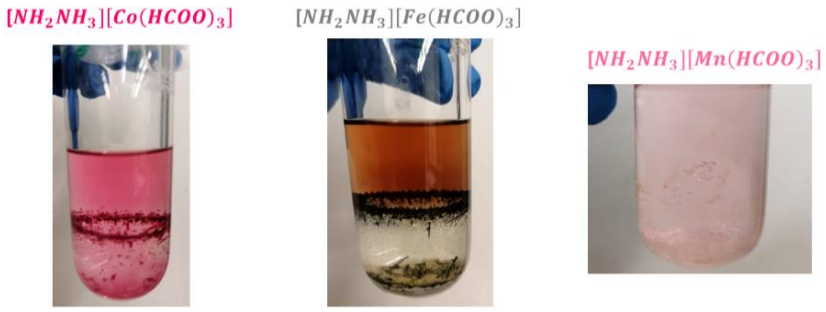

Figure 3.2-1: photo of the reaction mixture of $[NH_2NH_3][M(HCOO)_3]$with M = Mn^{2+}, Fe^{2+}, Co^{2+}.

The first attempts to obtain the product were made collecting the precipitate after one day. The PXRD showed the presence of the perovskite in P*na*2_1 polymorph for Mn and Fe, instead the $P2_12_12_1$ polymorph was observed for Co confirmed by the Rietveld refinement (Figure 3.2-2). In Table 3.2-1 are reported the relative cell parameters. The atomic coordinations are reported the Experimental Methods on Table 7.9-5.

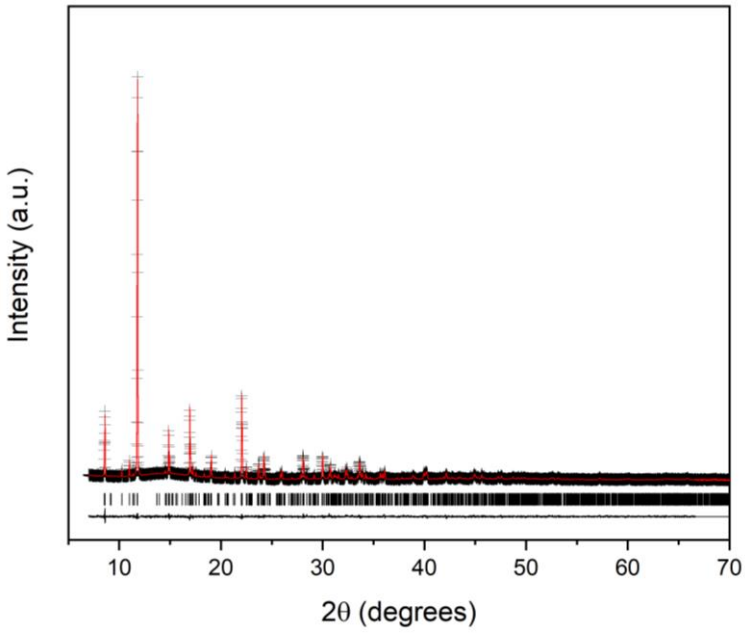

Figure 3.2-2: Rietveld refinement (wRp = 3.68 %) of the perovskites polymorph of $[NH_2NH_3][Co(HCOO)_3]$ the data are recorded at Elettra, synchrotron (Trieste) with wavelength λ = 1.0332 . Black crosses, red line and black line represent the observed, calculated and difference data respectively. The black tick marks indicate the Bragg reflection of the main phase.

Table 3.2-1: experimental cell parameters for perovskites $[NH_2NH_3][M(HCOO)_3]$ M = Mn^{2+}, Fe^{2+}, Co^{2+}.

Axis	$[NH_2NH_3][Mn(HCOO)_3]$	$[NH_2NH_3][Fe(HCOO)_3]$	$[NH_2NH_3][Co(HCOO)_3]$
a	8.9245(8)	8.801764(9)	7.3438(9)
b	7.8357(7)	7.775250(4)	13.8700(1)
c	11.7588(8)	11.64720(7)	7.9474(1)

Obtaining the pure perovskite polymorph of Mn and Fe was quite challenging. In fact, other synthesis attempts showed the presence of other two phases: $M(HCOO)_2$ x $2H_2O$ and the chiral polymorph of $[NH_2NH_3][M(HCOO)_3]$. Figure 3.2-3 shows the PXRD pattern, recorded at the Elettra synchrotron (Trieste), of a perovskite $[NH_2NH_3][Mn(HCOO)_3]$ samples containing $Mn(HCOO)_2$ x $2H_2O$ (27%wg). The percentage of manganese formate hydrate was variable, but always below 50% in weight. The same situation was observed for the Fe compound.

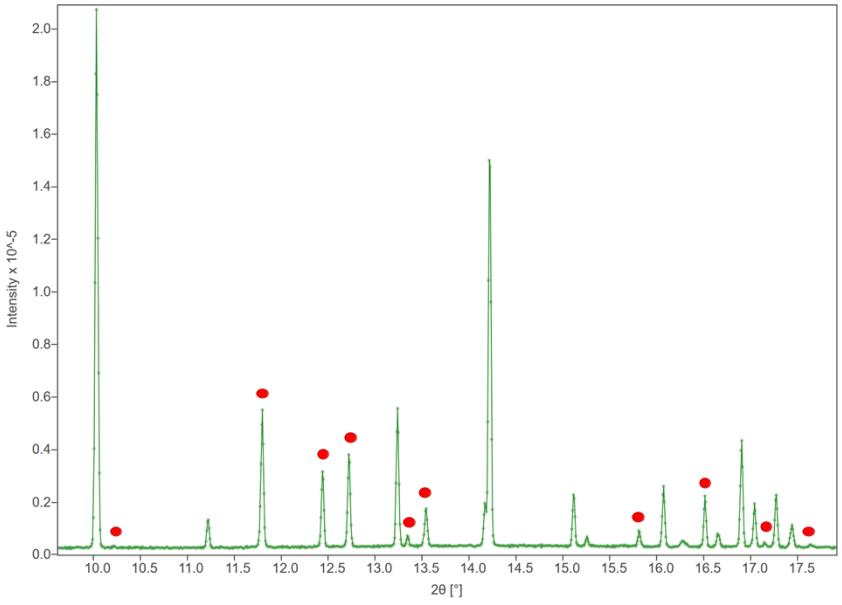

Figure 3.2-3: experimental pattern of perovskite $[NH_2NH_3][Mn(HCOO)_3]$ in which are pointed the peaks of the $Mn(HCOO)_2 \times 2H_2O$ secondary phase.

As we were interested in obtaining the chiral polymorph, due to its probably ferroelectric properties [1], we tried to modify the synthesis procedure considering the literature. By analysing the structure of 1-methyl-2-pyrrolidinone we noticed that, as it is an amide, it is weakly basic, less than the alkyl ammine. Alkyl ammine are basic molecules, and the basicity depends on how much the electron doublet on the nitrogen is available to bond. For diethylamine and butylamine the pKa is 11.1 and 10.4 respectively, as the electron acceptor force of the carbon chain is very low. However, when to the carbon chain are bonded electron attractor groups, such as carbonyl, halogen atom or amide group, the nitrogen doublet is delocalized and so the basicity of the amine decreases. This effect is even higher if resonance is present. In fact, 1-methyl-2-pyrrolidinone is a cyclic amide capable to do resonance, so its basicity is lower than the other amides. For example, the pKa of the pyrrolidine is 11.27; adding a carbonyl group increases the pKa to 14.7, whereas adding a methyl group in 1-methyl-2-pyrrolidinone should not change the pKa significantly due to the low electron attractor effect of the methyl. So, it is safe to assume that its pKa is around 14.7, which means that it is a weak basis. These observations let us to suspect that the effect of 1-methyl-2-pyrrolidinone in stabilizing the chiral form is due to its basicity, instead of the high viscosity.

To prove this point, we decided to synthesize the chiral polymorphs of Fe and Mn from a solution at higher pH. In our previous synthesis, following Pikul *et al.* [60], the measured pH was around 5 and we have increase it to 6/7. Experimentally this was achieved by decreasing the quantity of formic acid keeping constant the hydrazine. The PXRD analysis for the synthesis of the Mn and Fe compounds showed the presence of the pure chiral phase immediately after the synthesis. This synthesis clearly showed the role of the pH in selecting the obtained polymorph. On top of the pH effect we also need to consider the fact that in the latter synthesis the quantity of formic acid present in the solution was significantly less which can also explain the lower content of $M(HCOO)_2 \times 2H_2O$ as impurity in the final product. It is also worth stressing that we still observe the presence of $M(HCOO)_2 \times 2H_2O$ as impurity at low level which we think might be related to the presence of water in the mixture, that facilitates the formation of the metal formates, as already noticed for the $[NH_4][M(HCOO)_2]$ compounds. In Table 3.2-2 are reported the cell parameters found for chiral polymorph of $[NH_2NH_3][Fe(HCOO)_3]$ and $[NH_2NH_3][Mn(HCOO)_3]$ obtained by Le Bail fitting.

Table 3.2-2: cell parameters for the chiral polymorph of $[NH_2NH_3][Fe(HCOO)_3]$ and $[NH_2NH_3][Mn(HCOO)_3]$.

axis	Chiral $[NH_2NH_3][Fe(HCOO)_3]$	Chiral $[NH_2NH_3][Mn(HCOO)_3]$
a	7.966564(3)	8.046561(7)
b	7.966078(0)	8.046561(0)
c	7.565904(9)	7.779900(2)

3.2.1 Transformation from chiral to perovskite polymorph

For M= Zn [100], Mn, Fe [60] in literature are reported both the perovskite and the chiral polymorphs. [39, 60]. To date, these two polymorphs have been discussed separately, except for M=Zn for which it has been reported that over time or upon grinding a transformation from the chiral to the perovskite polymorph occurs [100]. This behaviour has not been deeply studied in literature and the same transition from the chiral to the perovskite polymorph have not been reported other for the other d-metal compounds. During our studies we noticed that the chiral polymorph with Mn and Fe were not stable over time; in fact, we observed a transformation of the chiral polymorph into the perovskite over time. This occurred for sample obtained using both synthesis procedures: without any template agent and with the increased pH. Moreover, we noticed that this transformation occurs both keeping the sample in solution or dry.

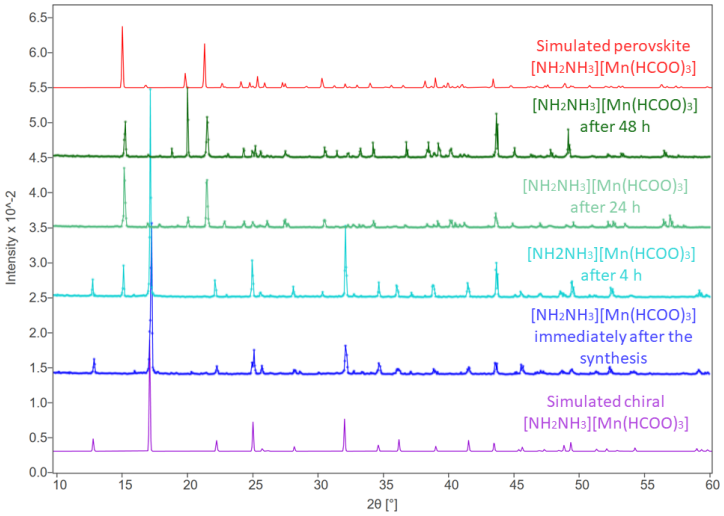

Figure 3.2.1-1: Sequence of PXRD from chiral to perovskite polymorphs of $[NH_2NH_3][Mn(HCOO)_3]$ together with the simulated patterns of the two polymorphs. The extra peaks belongs to the $Mn(HCOO)_2 \times 2H_2O$ impurity.

In Figure 3.2.1-1 are reported the PXRDs of $[NH_2NH_3][Mn(HCOO)_3]$ immediately after the synthesis and at different times until the transformation was completed. A similar behaviour has been observed for the chiral Fe polymorph where the transformation is often accompanied by the presence of $Fe(HCOO)_2$ x $2H_2O$ as impurity. This transition has not been observed for the Co compound, for which the chiral polymorph is stable within the observation time used in this work. The transition has different rates depending on the *d*-metal and on the relative humidity of the environment. In fact, the transformation is always faster for Mn than for Fe, and its rate increases with increasing the environment humidity. The transformation for the Mn chiral polymorph is completed between one and five days (depending on the environment humidity), instead the Fe phase transforms in almost three days. Mn is not new to give unstable phases, in fact, also for $[NH_4][Mn(HCOO)_3]$, the chiral $P6_3$ phase evolves with time into the orthorhombic polymorph with $Pna2_1$ space group which has a perovskite-like architecture. This suggest that the chiral polymorph, both for ammonium and for hydrazine, are not stable and tends to evolve into a more stable perovskite-like architecture.

The rate of the transition is also influenced by the environment humidity. We observed that this transformation has different rates when the samples are synthesized at different relative humidity. Our observations suggest that humidity can accelerate the transition, which for Mn can occur in one day when the relative humidity is around 35%. To confirm that humidity can favour the transition, we decided to expose the chiral Fe polymorph to controlled relative humidity and follow the transition thanks to the different colour of the two polymorphs (the chiral Fe polymorph is light blue, whereas the perovskite one is dark purple almost black). The experimental set up is shown in figure 3.2.1-2. The N_2 insufflate in the first flask gurgled into some water, then, the N_2 flux enriched of water goes to the second flask and enters in contact with the samples. The powder of $[NH_2NH_3][Fe(HCOO)_3]$ was mixed frequently, so all the sample could be in contact to the flux.

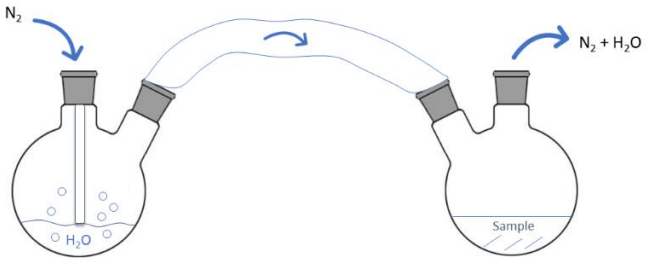

Figure 3.2.1-2: experiment set up used to expose the sample of chiral $[NH_2NH_3][Fe(HCOO)_3]$ to humidity in N_2 atmosphere.

At the beginning of the experiment the powder was light blue, in the chiral polymorph, after few minutes its colour changes to light violet. After 2.5 hours the colour of the powder was dark pink, after a day violet and black when the transformation was completed. In Figure 3.2.1-3 are reported the photos of the transition showing the changes of colour of the sample.

Figure 3.2.1-3: samples of $[NH_2NH_3][Fe(HCOO)_3]$ during the transition to chiral (left) to perovskite (right) when exposed to N_2 and humidity.

The same experiment was performed using dry O_2, and we found that the chiral phase is stable for about 9 hours, then it started to become red, probably due to the oxidation of iron to Fe^{3+}; the PXRD shows the presence of the chiral phase and $Fe(HCOO)_2 \times 2H_2O$.

To follow the transformation from the chiral to the perovskite polymorph, we decided to perform a time resolved diffraction experiment on the MCX beam line at the Elettra synchrotron (Trieste). The entire experiment lasted 7 h, but unfortunately, we have not been able to see the full transformation and the percentage of perovskite polymorph was low. Nevertheless, during the experiment we observed a clear shift of the Bragg reflections of the chiral polymorph phase (see Figure 3.2.1-4) due to an initial anisotropic distortion that will eventually leads to the perovskite polymorph.

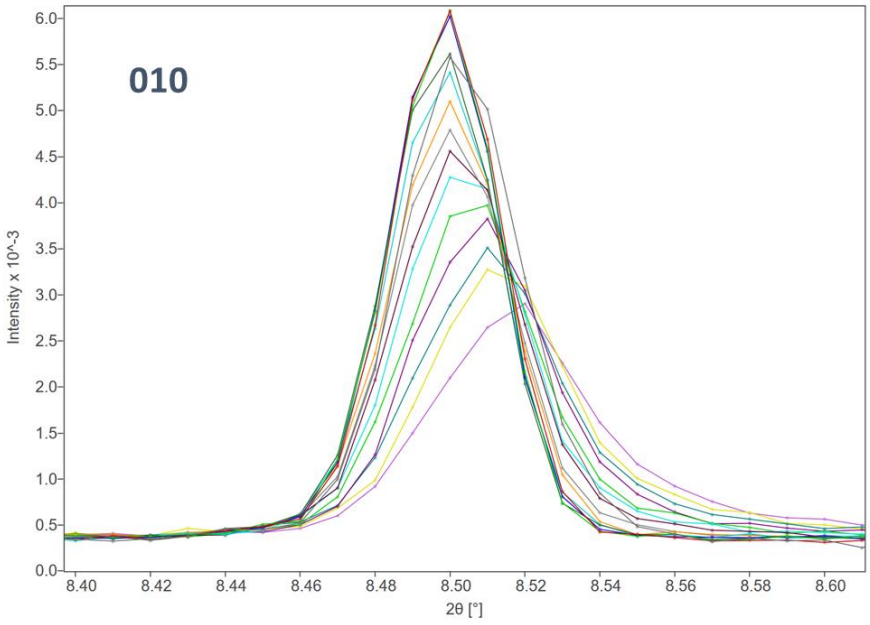
010
Intensity x 10^-3
6.0
5.5
5.0
4.5
4.0
3.5
3.0
2.5
2.0
1.5
1.0
0.5
0.0
8.40
8.42
8.44
8.46
8.48
8.50
8.52
8.54
8.56
8.58
8.60
2θ [°]

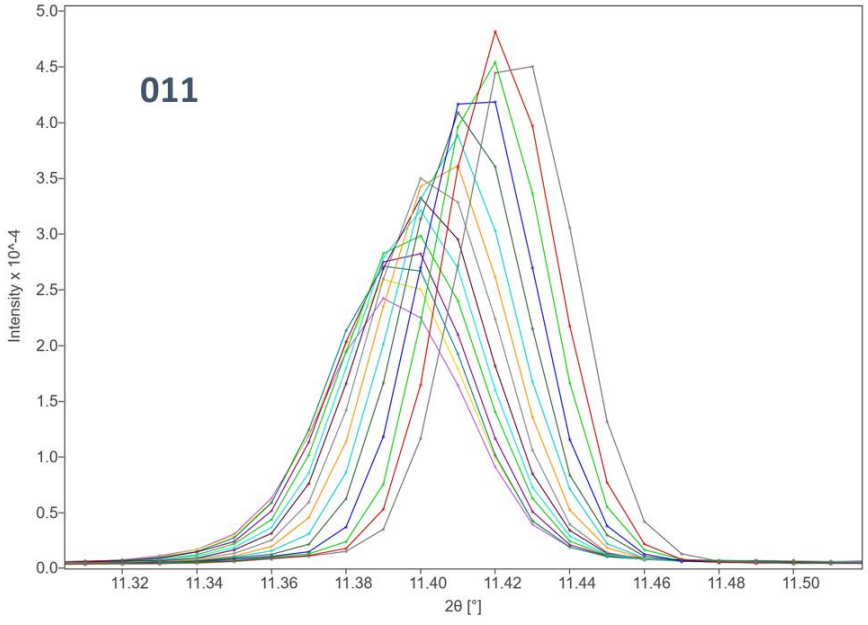
011
Intensity x 10^-4
5.0
4.5
4.0
3.5
3.0
2.5
2.0
1.5
1.0
0.5
0.0
11.32
11.34
11.36
11.38
11.40
11.42
11.44
11.46
11.48
11.50
2θ [°]

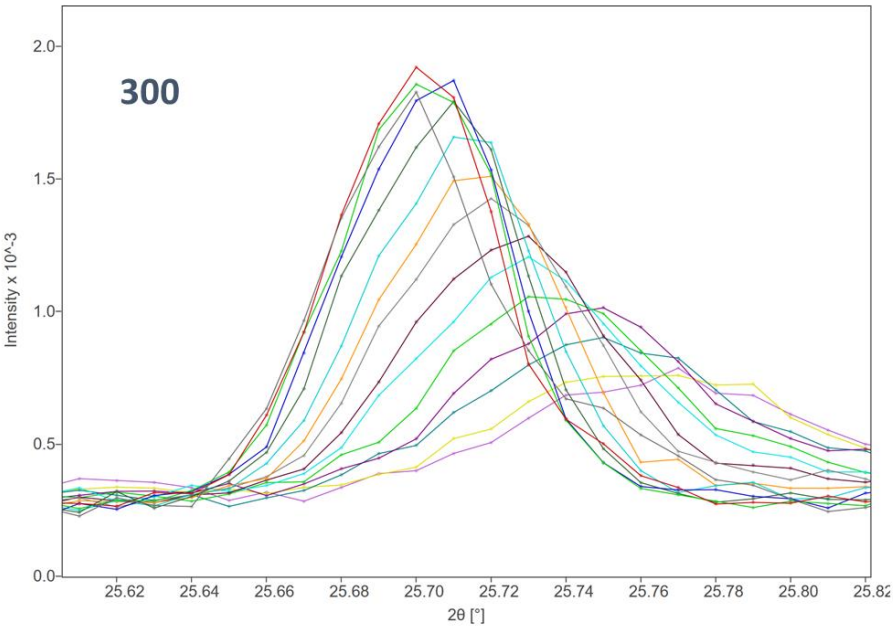

Figure 3.2.1-4: shift of the main peaks for chiral [NH_2NH_3][$Mn(HCOO)_3$] polymorph. For 010 and 300 there is a shift to higher angles, instead for 011 to lower angles.

In Figure 3.2.1-5 are reported the cell parameters of the chiral polymorph over time obtained from a LeBail fitting of the data, around 2.5 h there is a step change in the cell parameter lengths. We suspect that, due to the lack of humidity, the transition rate was very slow, so in another attempt we recorded the PXRD patterns by exposing the sample to humidity, by gurgling N_2 in water and then pointing it towards the sample. The results were not satisfactory, in fact, the PXRD shows the presence of $Mn(HCOO)_2$ x $2H_2O$ that increased in time with the exposure to humidity.

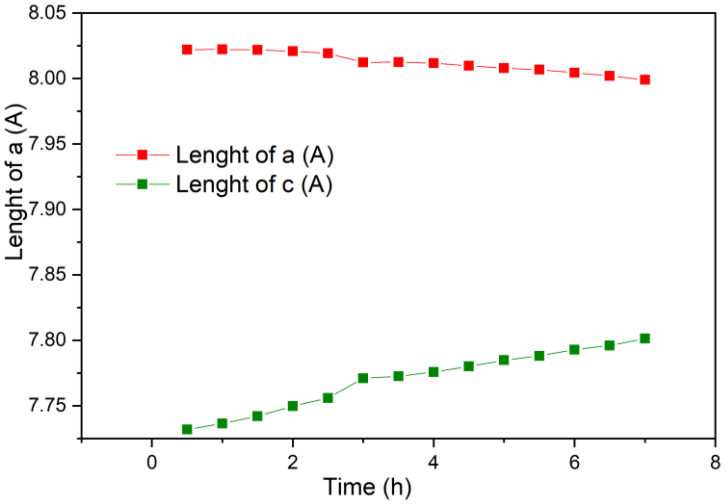

Figure 3.2.1-5: a- and c- cell parameters versus time for the transition from chiral to perovskite polymorphs in $[NH_2NH_3][Mn(HCOO)_3]$. Errors are smaller than the symbol size.

As shown, this transition was not so easy to follow using diffraction techniques, so we tried to follow it taking advantage of the different resistivity value between the two polymorphs. For this measurement we decided to use the $[NH_2NH_3][Fe(HCOO)_3]$ sample due the relative slow transition. In Figure 3.2.1-6 it is possible to observe an increase of the resistance by three orders of magnitude during the 22 hours of measurements. As shown later, the initial value agrees with the data found for the chiral polymorph, and, due to the fact that $[NH_2NH_3][Fe(HCOO)_3]$ transforms in this arc of time, we assume that the increase of the resistance is due to the transformation to the perovskite polymorph.

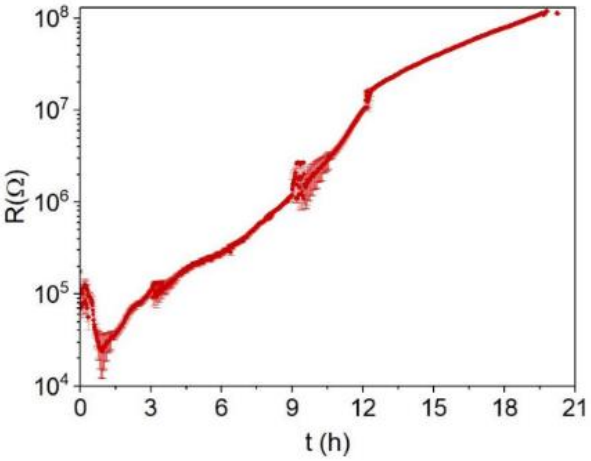

Figure 3.2.1-6: resistance vs time for $[NH_2NH_3][Fe(HCOO)_3]$.

In conclusion, we have demonstrate that the transition from the chiral to the perovskite polymorphs in hydrazine compounds occurs for $[NH_2NH_3][Mn(HCOO)_3]$ and for $[NH_2NH_3][Fe(HCOO)_3]$ even though we have not been able to follow the complete transformation by x-ray diffraction. From our observations this transition occurs both at the solid-state and in solution, with different rate depending on the metal inside the structure and on the level of ambient humidity. The transitions mechanism may involve the presence of water has not been considered in the crystal structures of the hydrazine compounds, even though their sensitivity to the moisture is not negligible. At this point the water-mediated mechanism of the reorganization of the framework could involve the adsorbed water coming from the reagents or from the moisture present in the ambient atmosphere. Despite this difference it interesting to note that we observed this transition only for the compounds with manganese and iron, but not the one with cobalt. The structure is not identical, but the channel structure is maintained. At this point could be hard to describe the real mechanism, also taking into account that the transformation has different rates depending on the metal site, indication that also the crystal structure can promote differently this transformation.

3.3 Transition of the $[NH_2NH_3][Mn(HCOO)_3]$ perovskite phase with temperature

As mentioned before, perovskite polymorph show a temperature induced transition from the *Pna*2_1 space group to *Pnma*. These transitions were investigated for the first time by S. Gao and co-workers [39], who followed the evolution of the crystal structure with PXRD for the perovskite polymorph of

$[NH_2NH_3][M(HCOO)_3]$ with M = Mn^{2+}, Co^{2+}, Zn^{2+}, Mg^{2+}. They reported the PXRD from 290 to 500 K showing the transition at 350-360 K for the structure with manganese. As we were investigating the $[NH_2NH_3][Mn(HCOO)_3]$ compound, we decided to repeat the experiment adding more temperature points to the one present in literature.

Differential scanning calorimetry measurement (DSC) were performed in the 216-413 K range, and the results are shown in Figure 3.3-1. The DSC trace shows a thermal event around 355 K. To understand the nature of the latter event we performed a series of PXRD on the perovskite polymorph of $[NH_2NH_3][Mn(HCOO)_3]$ from 298 to 373 K recording a dataset every 10 degrees with an heating rate of 5 K/min.

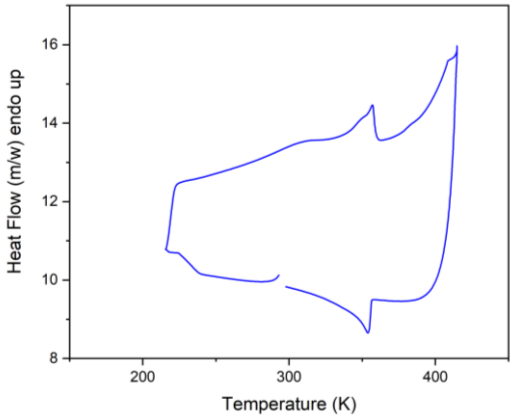

Figure 3.3-1: DSC trace of the perovskite polymorph of $[NH_2NH_3][Mn(HCOO)_3]$.

Figure 3.3-2 shows PXRD data. The only visible change is the decrease with temperature of the 111 reflection at $2\theta \sim 16.85$. From the Le Bail refinement it was possible to obtain the cell parameters of the two structures and estimate the transition temperature of 358.15 K from the slope of those trend. This temperature agrees to the one found in literature. In Figure 3.6-3 are reported the cell parameters trend *versus* temperature which show a decreasing of the *a*- axis length and an increase of

the *b*- and *c*- axis lengths. During the transition the cell volume gradually increases from 821.99 Å^3 to 828.34 Å^3.

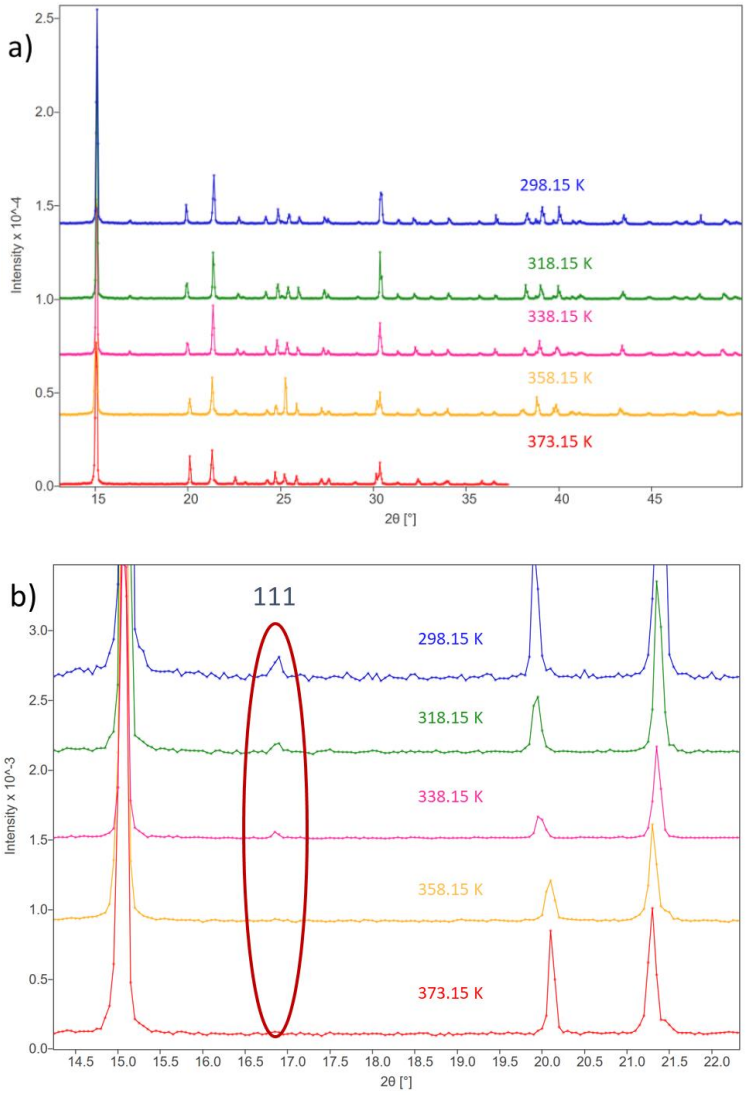

Figure 3.3-2: a) series of PXRD performed at different temperatures on the perovskite polymorph of [NH_2NH_3][$Mn(HCOO)_3$]; b) zoom at 16.9 2θ to evidence the disappearance of the 111 peak with temperature.

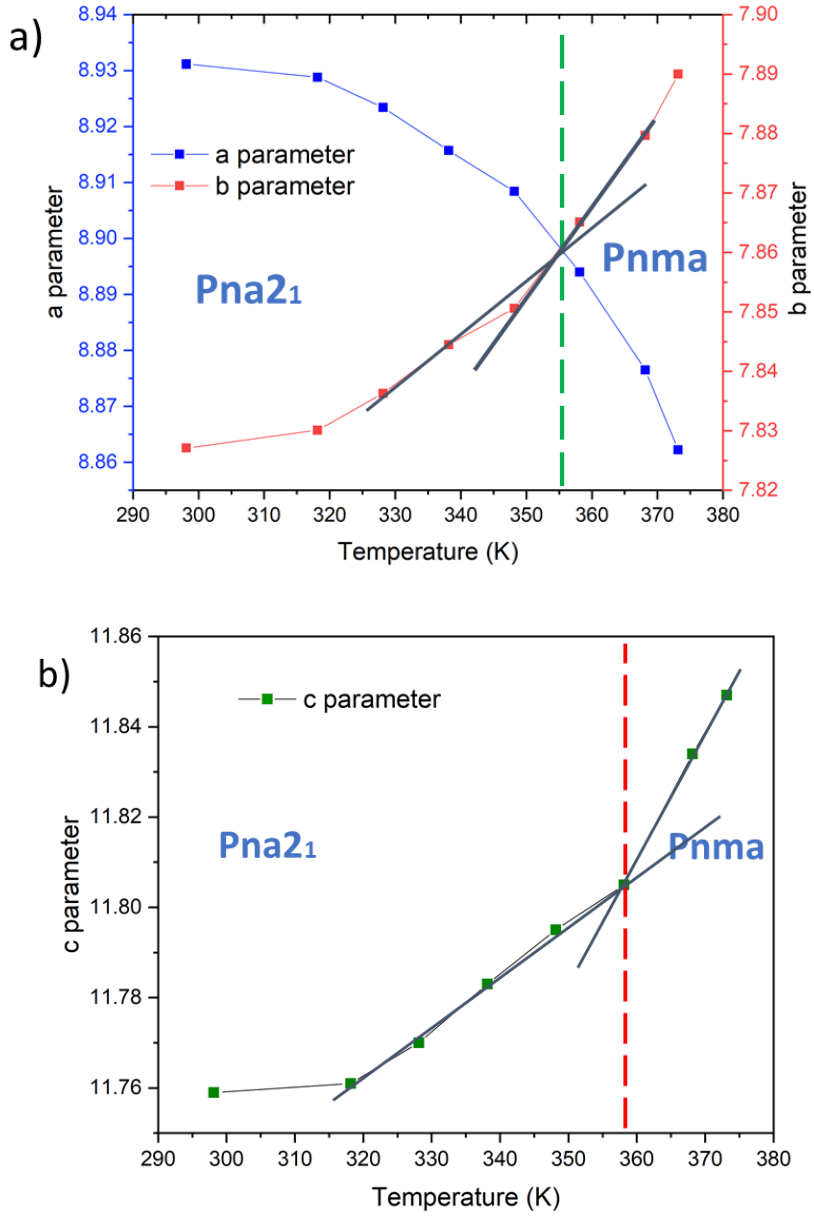

Figure 3.3-3: cell parameters trend for the transition of perovskite $[NH_2NH_3][Mn(HCOO)_3]$.

3.4 Synthesis of the mixed phases of $[NH_2NH_3][Mn/Fe(HCOO)_3]$

In literature are already known hybrid-formate perovskites with general formula ABB'X_3. The B and B' cations can be heterometallic or mixed-valence metals. Only two compounds are known to crystallize in the perovskite polymorph ($[(CH_3)_2NH_2][Na_{0.5}Fe_{0.5}(HCOO)_3]$ and $[(CH_3)_2NH_2][Na_{0.5}Cr_{0.5}(HCOO)_3]$ [101, 28]) together with another family with general formula $[(CH_3)_2NH_2][M^{II}\ Fe^{III}\ (HCOO)_6]$ (M = Fe^{2+}, Co^{2+}, Mn^{2+}, Mg^{2+}, Ni^{2+}, Zn^{2+}, Cu^{2+}) [102, 29, 103, 104, 105]. With the aim to synthesize new hydrazine-formate perovskites, we tried to obtain compounds that contains in the B site both manganese and iron. Moreover, due to the instability of the chiral polymorph for $[NH_2NH_3][Mn(HCOO)_3]$ we tried to investigate if it was possible to stabilize this phase, as the chiral phase of $[NH_2NH_3][Fe(HCOO)_3]$ is more stable.

The first attempt was to obtain the perovskite polymorph; to do that we tried a composition Fe/Mn 70/30. Two methanol solution of $MnCl_2$ x $4H_2O$ and $FeCl_2$ were mixed and then added to another methanol solution containing hydrazine (0.5 ml) and formic acid (0.7 mL), the pH of the solution was around 6. After two days, at the interface of the solution grey/blue little crystals were grown and on the bottom of the vessel a white powder precipitated. The whole product was then filtered and washed with methanol. The PXRD shows the presence of only one perovskite phase and the Le Bail fitting evidence the presence of an orthorhombic phase with *Pna*2_1 space group with the cell parameters that are in between the value of the end-member perovskite compounds (Table 3.4-1).

Table 3.4-1: cell parameters for perovskite $[NH_2NH_3][Mn(HCOO)_3]$ and $[NH_2NH_3][Fe(HCOO)_3]$ compared to the one found for $[NH_2NH_3][Fe_{0.7}Mn_{0.3}(HCOO)_3]$ and $[NH_2NH_3][Fe_{0.6}Mn_{0.4}(HCOO)_3$.

axis	Perovskite Fe (Å)	Mix $Fe_{0.7}Mn_{0.3}$ (Å)	Mix $Fe_{0.6}Mn_{0.4}$ (Å)	Perovskite Mn (Å)
a	8.801764(9)	8.841(4)	8.824001	8.9245(8)
b	7.775250(4)	7.797(5)	7.776388	7.8357(7)
c	11.64720(7)	11.6812(9)	11.64917	11.7588(8)

After this encouraging result, we decided to increase the percentage of manganese e.g.: Fe/Mn 60/40. In this case, we also wanted to investigate if it is possible to obtain the chiral polymorph and if it transforms into the perovskite over time. The adopted experimental procedure was the same as already described, but we used 1.2 mmol of $FeCl_2$ and 0.8 mmol of $MnCl_2$ x $4H_2O$ each of which was

dissolved in 7.5 mL of methanol. The reaction produced a pale-yellow precipitate that was immediately filtrated. The PXRD pattern shows the presence of a chiral polymorph, and the Le Bail fitting shows a trend of cell parameters that follows the Vegard's law (Table 3.4-2).

Table 3.4-2: cell parameters of chiral $[NH_2NH_3][Fe_{0.6}Mn_{0.4}(HCOO)_3]$ compared to the pure chiral $[NH_2NH_3][Fe(HCOO)_3]$ and $[NH_2NH_3][Mn(HCOO)_3]$.

axis	Chiral Fe (Å)	Mix $Fe_{0.6}Mn_{0.4}$ (Å)	Chiral Mn (Å)
a	7.966564(3)	7.988453(4)	8.046561(7)
b	7.966078(0)	7.988448(0)	8.046561(0)
c	7.565904(9)	7.652981(2)	7.779900(2)

We observed that also in this case the transition from the chiral to perovskite polymorph over time. In fact, after four days the PXRD shows the presence of the perovskite polymorph, whose peaks stay between the ones of the pure perovskite phases.

In table 3.7-1 are summarized the cell parameter values found for the perovskite $[NH_2NH_3][Fe_{0.6}Mn_{0.4}(HCOO)_3]$ phase compared to the perovskites end-member and perovskite $[NH_2NH_3][Fe_{0.7}Mn_{0.3}(HCOO)_3]$. As observed previously, the cell parameters of the mixed phases stay between the end members of the pure phases.

3.5 Magnetic measurements and attempts of polarization switching on [NH2NH3][M(HCOO)3], M = Mn2+, Fe2+, Co2+.

3.5.1 Magnetic characterization

SQUID measurements have been performed on $[NH_2NH_3][M(HCOO)_3]$, M = Mn^{2+}, Fe^{2+}, Co^{2+}, in a range between 2 and 200 K and magnetic field between 1 kOe and 20 kOe, whereas the AC susceptibility were performed in a frequency range between 10 and 1000 Hz with an ac magnetic field of 4 Oe.

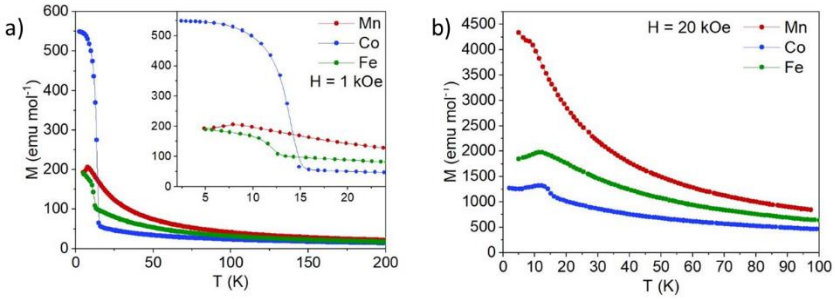

Figure 3.5-1: Temperature dependence of magnetization, measured in an applied magnetic field of 1 kOe (a) 20 kOe (b) following a ZFC (or FC amend) procedure.

Temperature dependences of magnetization M(T) of the three samples are shown in Figures 3.5-1 at 1 kOe (a) and 20 kOe (b). The Co and Fe samples show in a 1kOe an increase of magnetization, with a Brillouin-like shape, below 14 K and 12.5 K, respectively. Instead, the Mn sample shows a cusp at 7.9 K. The magnetization of the Co sample at 5 K is about three times larger than that of Mn and Fe samples. By increasing the applied magnetic field to 20 kOe the M(T) curves of all the samples show a cusp-like variation at the same critical temperatures. At 5 K the Mn sample has a value of magnetization about three times larger than the Co one.

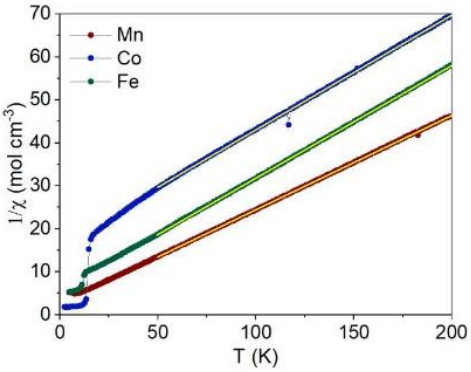

Figure 3.5-2: Temperature dependence of inverse of the susceptibility for the three samples collected with an applied field of 4 Oe.

The high temperature susceptibility of all samples follows the Curie-Weiss law (Figure 3.5.1-2). The linear fit of the $1/\chi$ results in the C and θ parameters. The obtained values are consistent with the ones reported for the same Mn and Co samples in literature [39]. The negative value of θ suggests dominant antiferromagnetic interactions that increase moving from Mn to Co.

Table 3.5-1: Curie-Weiss temperature and μeff for the three compounds obtained from the fit of the inverse susceptibility at high temperature.

Metal	Θ (K)	μ_{eff}
Co	-61.1 ± 0.4	5.47 ± 0.01
Fe	-21.2 ± 0.1	5.52 ± 0.01
Mn	-11.3 ± 0.1	6.03 ± 0.01

From *C* it was possible to estimate the average effective magnetic moment for magnetic ion μ_{eff}. The obtained values follow the same trend of the expected moments for the three ions (Co^{2+}, Fe^{2+} and Mn^{2+}) calculated considering only the spin contribution (μ = 3.87, 4.90 and 5.92 μB). However, all the experimental values are larger than the expected ones (see table 3.5.1-1). The difference increases by moving from Mn to Co, probably because of the increase of the spin-orbit coupling of the magnetic ion.

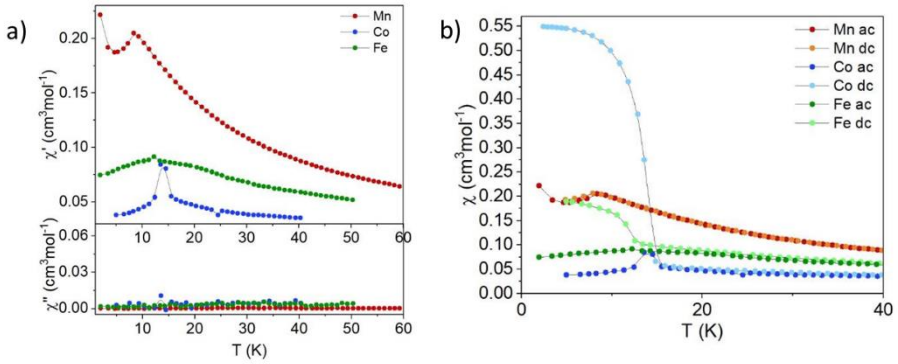

Figure 3.5-3: (a) in-phase and out-of-phase AC magnetic susceptibility of the three samples. (b) Comparison of magnetic susceptibility obtained from AC, measured with a driving field of 4Oe and frequency from 10 Hz to 1kHz and DC measurements at 1 kOe.

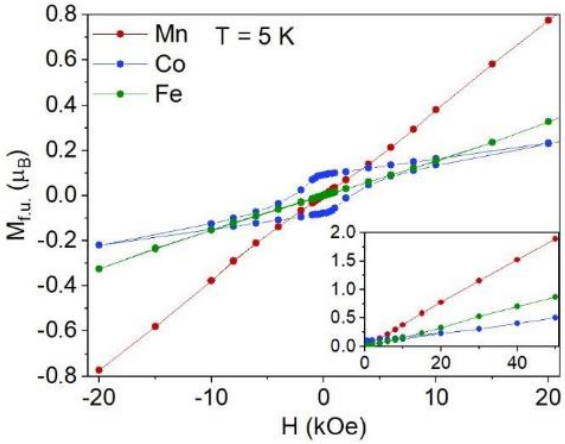

Figure 3.5-5: Field dependence of magnetization for the three samples. Inset: field dependence of magnetization at high field.

Figure 3.5.1-3 shows the AC measurement performed on the three compounds (panel a) and the comparison of the magnetic susceptibility obtained from DC measurements under 1 kOe applied field with the in-phase component of the AC susceptibility measured with an AC driving field of 4 Oe (panel b). Regarding the AC magnetic susceptibility measurements we can observe a variation of the in-phase component of susceptibility at the critical temperatures for all the samples, to which correspond an about zero out-of-phase component. The Mn sample shows the same cusp of DC measurement (the comparison is shown in Figure 3.5.1-3.b). Whereas for Co and Fe sample a peak occurs in correspondence of the increase of magnetization in the DC measurement. The peak of Fe sample is very broadened. The AC measurements were performed with different frequencies (from 10 Hz to 1 kHz): no sample shows a clear frequency dependence of AC susceptibility.

The field dependence of magnetization is reported for the three samples in Figure 3.4-5. The Co sample shows a large hysteresis loop with a coercive field of 2.5 kOe and a remanence of 0.09 μB. Even the Fe sample displays a hysteresis, but much smaller, with a coercive field of 90 Oe and a remanence of 0.001 μB. No hysteresis and a linear variation with the field are shown by the Mn sample. By looking at high fields up to 50 kOe, all the samples show a linear variation with the field. The saturation magnetization is not reached at 50 kOe for any samples. The molar magnetization at 50 kOe is 0.5, 0.87, 1.89 μB respectively for the Co, Fe and Mn sample.

The *M(H)* curves at high fields of the Mn and Co samples display a change of slope at about 9 kOe and 40 kOe, probably suggesting a spin-flop transition [39].

The magnetization measurements we performed on all three samples suggest a main antiferromagnetic character. The small residual in the field dependence magnetization and the Brillouin like shape of the M(T) curves suggest a weak ferromagnetic component in the Fe and Co compound. These observations let us to conclude that the Fe and Co compound are likely canted antiferromagnets. On the contrary the Mn compounds does not show any weak ferromagnetic component suggesting a "pure" antiferromagnetic structure.

3.5.2 Attempts of polarization

Polarization attempts on $[NH_2NH_3][M(HCOO)_3]$ with M = Mn^{2+}, Fe^{2+}, Co^{2+}, were performed on the samples synthesized from solution in their chiral phase. Immediately after the synthesis the powders were dried under N_2 flux for few minutes to avoid the transition into the perovskite phase, then the samples were pressed to make pellets suitable for the ferroelectrics measurements using the new created device (see Appendix chapter), trying to avoid the use of the metallization. In fact, due to the exposure of the sample in air to dry the silver paste, the material could evolve into the perovskite phase. Moreover, the classic metallization for used for the ceramics material could destroy the sample, due to the hard operating conditions.

In Table 3.5.2-1 are reported the resistance value found at RT for each compound.

Table 3.5.2-1: resistance values for chiral and perovskite $[NH_2NH_3][M(HCOO)_3]$ with M = Mn^{2+}, Fe^{2+}, Co^{2+} at RT.

Compound	R @RT (Ω)
$[NH_2NH_3][Mn(HCOO)_3]$ chiral	10^7
$[NH_2NH_3][Fe(HCOO)_3]$ chiral	10^4
$[NH_2NH_3][Co(HCOO)_3]$ chiral	10^3 - 10^6

As observed for the ammonium-formate compounds, all the samples showed a conductive behaviour at RT and generally the resistance increases with the applied tension, this means that the conductive phenomenon is observed at low tension and increases linearly with the tension.

Also, in this case has not been possible to polarize the material, we suspect due the same reason as for the ammonium-formate compounds. As explained in chapter 3, in polycrystalline materials the domains are randomly organized and though the poling process it is not possible to orient these grains, but it is possible to orient the domains in each grain. The polarization of these material is characterized by only two possible polarizable directions, thus, during the poling process on the powder sample not all the domains are polarized, and the resulting macroscopic polarization is very weak and difficult to measure.

4 IONIC CONDUCTIVITY

4.1 Proton conduction in $[NH_4][M(HCOO)_3]$ and $[NH_2NH_3][M(HCOO)_3]$ with $M = Mn^{2+}, Fe^{2+}, Co^{2+}$

4.1.1 Introduction to solid state electrolytes, ionic and proton conduction

Electrolytes are materials in which the electrical conduction is due to the movements of ions instead of electrons, and for this reason they are also called ionic conductors. Usually, electrolytes are employed in battery technology in the liquid state, in which a salt is dissolved in a solvent and produce ions that generates electrical conduction. Despite they are largely used, such materials are very hazardous for the environment, and they are usually air sensitive. For these reasons solid state electrolytes should be employed, but, due to lower ionic conductivity respect to the liquid conductors, they have not yet been commercialized as crystalline solid.

In solids ionic conductors, conductivity is thermically activated and is due to:

- vacancies in the material that allows the hopping of an ion from its site to a near free site
- presence of interstitial sites in which a different ion is present and can move

This mobility follows the Arrhenius's law type, and it is proportional to $Ae^{-\frac{E}{KT}}$ in which E represents the energy barrier required to move the ions, K is the Boltzman constant and T is the temperature expressed in Kelvin. Ionic conductivity (σ, S cm^{-1}) is therefore expressed as (eq. 1):

$$\sigma(T) = \sigma_0 \, e^{-\frac{E}{KT}} \quad (1)$$

where σ_0 represents the saturation conductivity when all the charge carriers are activated and able to hop. From this law, by plotting ln(σ) versus ln(1/KT) it is possible to obtain E, the activation energy of the process.

Solid state electrolytes can be total inorganic materials or polymers. In the inorganic category it is possible to find, for example, the MAH_4 (M = alkali metal, A = Al, B) family which is characterized by a high conductivity up to 10^{-3} S cm^{-1} but only after a phase transition that occurs at relative high temperatures (T > 390 K for $LiBH_4$ [106]), or ceramic ionic conductors like $Li_{1:4}Al_{0:4}Ti_{1:6}(PO_4)_3$ [107] which has a similar ionic conductivity to the previous family of materials but for which is difficult to obtain a good contact between the electrodes [108].

Also, solution of electrolytes in polymers have been studied, but they act like ionic conductor only after a phase transition from the crystalline form to amorphous. For example, polyethylene oxide shows an ionic conductivity above 330 K of 10^{-4} S cm^{-1} [109].

A particular case of ionic conduction is represented by proton conductivity, in which the ion that generates the conduction is H^+. This property in solids has attracted attention due to the potential application in fuel cells [110] and many materials both organic, like Nafion [111], and inorganic like zeolites [112], $BaZrO_3$ [113] and $CsHSO_4$ [114] have been investigated. During the last decades metal organic frameworks (MOFs) and coordination polymers have been discovered as proton conductor, due to the variety of guests that they can accommodate and high chemical variety [107]. Kanda *et al.* [115] reported proton conductivity in MOFs in humidified condition (10^{-6} S cm^{-1}, 27 °C, 100% relative humidity (RH)). Since 2009, other crystalline MOFs have been discovered as proton and super-protonic conductor [116].

An equation to describe ionic conductivity is:

$$\sigma = z\, e\, n\, \mu \qquad (2)$$

where z is the valence of the carrier ion (in the case of proton conductivity z = 1), e represents the elementary charge, n is the concentration of ion carriers and μ is the mobility of the charge carriers. Therefore, increasing the mobility and the concentration of charges increases proton conductivity; these characteristics in MOFs are easily obtainable. In fact, due to the different architectures that can be designed, MOFs can reach very high mobility by constructing efficient proton-conducting pathways. Moreover, the ionic conductivity can be easily increased when MOFs are hydrated, reaching to 10-2 S cm-1 at room temperature (RT) also by introducing acidic species in the structure. Chemically these qualities are related to the hydrogen-bond network inside the pores that favours the hopping of the proton.

Traditionally the proton conductivity mechanisms are classified in two types:

- the vehicle mechanism, in which the conductivity is due to the direct diffusion of H_3O^+ ions or other species [117]
- the Grotthuss mechanism, in which the proton is transferred through hydrogen-bonds to the adjacent conducting media like water molecules (Figure 4.2-1) [118]

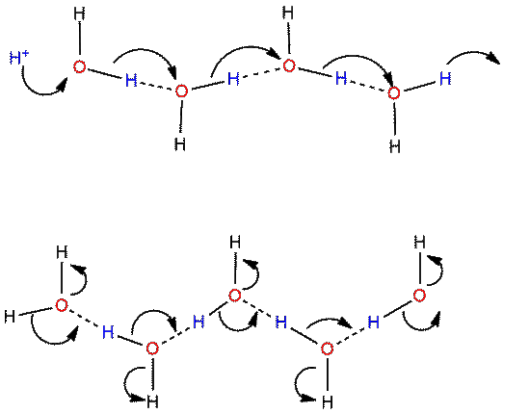

Figure 4.1.1-1: Grotthuss mechanism for proton transfer in water molecules. Top: hopping of hydrogen starting from an H^+ starter. Bottom: mechanism to restore the water molecules.

The Grotthuss mechanism is more efficient than the vehicle one as confirmed also by the diffusions rate of H^+ in water (36.2 x10^{-8} m^2 s^{-1} V^{-1}) compared to Li^+ and Na^+ (respectively 4.0 x 10^{-8} and 5.2 x 10^{-8} m^2 s^{-1} V^{-1}) [23]. Efficient proton-conductivity pathway and acidic species facilitate the migration of protons trough the hydrogen-bond network. Considering eq. 1, due to the efficient long range proton transport *via* hydrogen-bond network, the Grotthuss mechanism requires lower activation energy than the vehicle mechanism. This efficient proton-transport way requires generally less than 0.4 eV instead the vehicle mechanism requires energies higher that 0.4 eV [119].

To reach a high proton conductivity, the addition of acidic species is crucial. From the synthetic point of view this could be achieved in three ways:

- introduction of simple ions (like NH_4^+, HSO_4^- or H_3O^+) in the pores of the structure, that act as counterions (type I)
- insert an acidic group in the structure of the framework that act as a proton-donor (type II)
- inclusion of a charge-neutral acidic molecule in the MOF's voids (type III)

When proton conductivity is achieved through water molecules the conductivity depends on how strong the hydrogen-bond network is. Morover, there should be additional space inside the MOF's structure to host water molecules [116]. The adsorption of water can be also reversible, and it is possible to tailor conduction properties by going from di-hydrated to hemi-hydrated MOF's. Moreover, these three types of ionic conductivity can co-exist in the same structure.

Oxalate(ox)-bridged MOF have been largely studied as hydrated proton-conductive MOF due to their stability in water and high crystallinity. They can provide examples of each design of proton conductor listed above. For example, the 1D compound Fe(oxalate) x $2H_2O$ reported in 2009 (Figure 4.2-2), showed high proton conductivity (1.3 $x10^{-2}$ S cm^{-1}) in humid condition (RH = 98%) [120]. Its activation energy is 0.37 eV, indicative of the Grotthuss mechanism; since the protonic species are located in the framework, it gives an example of type II proton conductivity.

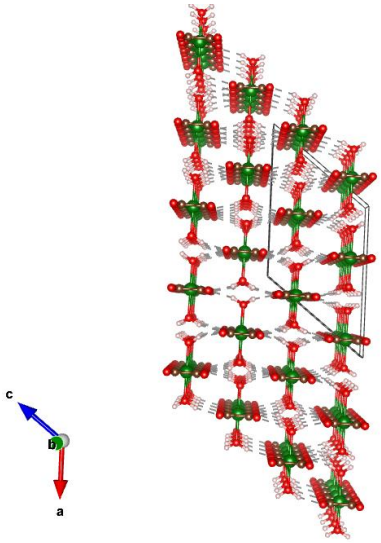

Figure 4.1.1-2: crystal structure of Fe(oxalate)2 x 2H2O. Carbon atoms are in browm, iron in green, oxygens in red and hydrogen in white.

In this case iron bonds in the equatorial position with the oxalate anion, instead the axials positions are occupied by two water molecules (see figure 4.1.1-2). The proton conductivity is observed due to the packed chains that act as proton-conductor pathway. Since acidic species suitable to provide carriers are absent, it is argued that process is related to the self-dissociation of water molecules strongly enhanced by the Lewis acidity of iron.

An example of proton conductor material belonging to both type I and III is given by $(NH_4)_2(H_2adp)[Zn_2(ox)_3]\cdot 3H_2O$ (H_2adp=adipic acid) [121] (Figure 4.1.1-3).

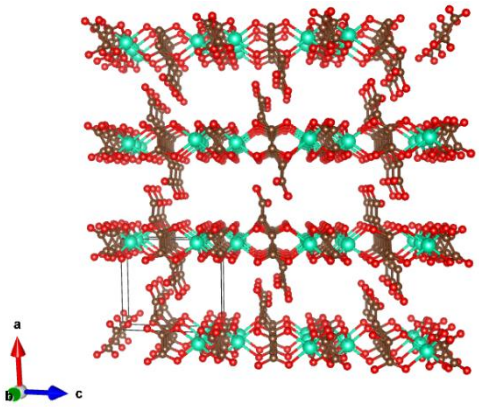

Figure 4.1.1-3: crystal structure of $(NH_4)_2(H_2adp)[Zn_2(ox)_3]\cdot 3H_2O$ viewed along the b axis. Guest molecule and hydrogens are omitted for clarity. Carbons atoms are in brown, oxygens in red, zinc in green.

H_2adp is a charge-neutral acidic molecule that, incorporated in the pores of the structure, promotes a type III ionic conductivity. Further, the structure possesses ammonium cation in the interlayers cavities that generate type I conduction behaviour. The activation energy of this process is 0.63 eV, high for a Grotthuss mechanism, but explainable with the fact that both the Grotthuss and partially the vehicle mechanisms are present.

An example of 3D MOF that shows proton conductivity of type I is $[(Me_2NH_2)_3(SO_4)]_2[Zn_2(ox)_3]$ [122]. In this case the structure is formed by an anionic framework of $[Zn_2(ox)_3]^{2-}$ in which $[(Me_2NH_2)_3SO_4]_n^+$ is interpenetrated. The structure could be seen as a honeycomb-like anionic framework possessing channels filled with dimethyl ammonium cations and sulphate anions; the latter are connected to each other through electrostatic interactions and hydrogen bonds forming a supramolecular network (Figure 4.1.1-4).

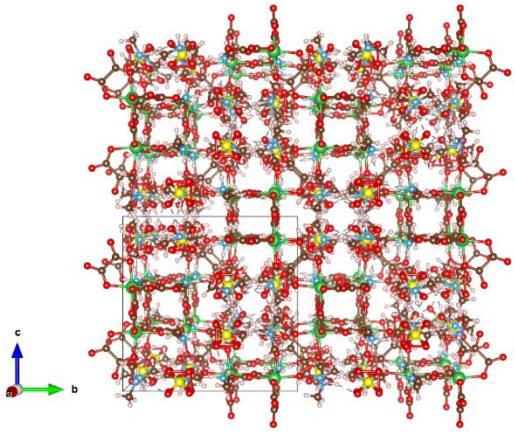

Figure 4.1.1-4: crystal structure of [(Me$_2$NH$_2$)$_3$(SO$_4$)]$_2$[Zn$_2$(ox)$_3$]. Hydrogens are omitted for clarity, zinc atoms are in green, nitrogen blue, sulfurs yellow, carbons brown and oxygens red.

The low conduction activation energy 0.13 eV is a clear indication of a Grotthuss mechanism and exclude the so-called vehicle conduction, also because the compound does not possess species that transport proton in long range distances. Crystallization water is not present in the structure, but adsorption measurements showed that large amount of water can be absorbed in humid conditions. The authors explain the ionic conductivity measured by an acid-base pair units. In fact, the dimethyl ammonium cation is known to provide dissociable proton in presence of water [123] and, due to the Grotthuss mechanism, the absorbed water molecule can mediate the proton transfer to the adjacent dimethyl ammonium cation trough hydrogen-bond or act like vehicle in form of hydronium ions. This mechanism is very similar to the one already reported in 2013 for different MOFs with free carboxylic acid with no water in the crystal structure [124].

Interestingly in 2011 has been reported a study in which different ligand were substituted in a framework which showed proton conductivity of type II [125]. The investigated group were: -COOH, -H, -OH, and -NH_2 for which has been found a correlation between the group acidity and the measured proton conductivity. In this case, the crystal structure of the analysed compound has large pores which could include water molecules, and the framework can be modified by changing the acidic group without significant alterations of the structural scaffold. Under high humid condition (RH = 98%) the compound showed proton conductivity from 10^{-8} to 10^{-5} S cm^{-1} depending on the acid specie. At the same conditions of humidity, the proton conductivity follows the series: -COOH > -OH > -H > -NH_2 which confirms that the proton carriers are released by the framework and the proton conductivity changes in relation to the acidity of the substituted group.

In this scenario, considering the structural analogies with other porous MOF featured by ionic conduction, we attempted a systematic investigation of the metal formates $A[M(HCOO)_3]$ with $A^+=NH_4^+$, $NH_2NH_3^+$ with the aim to test their ionic conduction properties.

4.1.2 Ionic conduction in $[NH_2NH_3][M(HCOO)_3]$ with $M = Mn^{2+}, Fe^{2+}$

The first attempts of ionic conduction measurements were performed on the chiral polymorph of the $[NH_2NH_3][Fe(HCOO)_3]$ compound. Since the hexagonal porous phase is unstable (see Chapter 2 for details), measurements were carried out immediately after the synthesis and for the two following days. In Figure 4.2.1-1 it is shown the Nyquist diagram (see Experimental Section) illustrating the behaviour of the sample over the three days. Measurements were performed in a range between 5 Hz and 13 MHz and each frequency represents a point in the diagram in ascending order from right to left. The measures were carried out on pressed pellets (7 mm diameter) of crystalline powder (experimental details are described in the Experimental Methods).

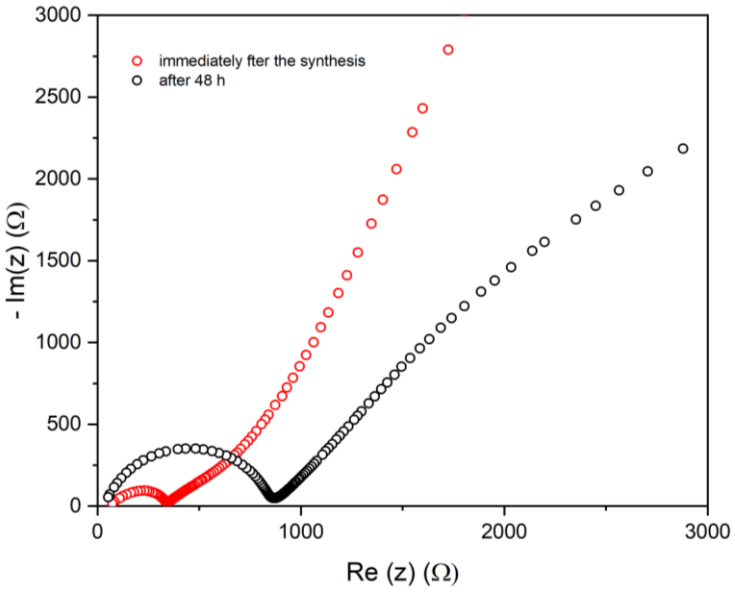

Figure 4.2.1-1: Nyquist plot of the chiral $[NH_2NH_3][Fe(HCOO)_3]$ compound. In the x axis is reported the real part of the impedance, in y the imaginary part changed its sign. Red line represents the ionic conductivity immediately after the synthesis and the black one after 48 h.

From the plot in Figure 4.2.1-1 it is possible to observe the typical behaviour of an ionic conductor: an arc with a Warburg impedance defined by the linear trend

of both the real and imaginary part of the Nyquist plot (explained in detail in the Experimental Methods). The ionic conduction is inversely related to the arc extension of the real part of the impedance. The ionic conduction progressively decreases with time as it is evidenced by the two measurements performed after the synthesis (red curve of Figure 4.1.2-1) and 48h (black curve of Figure 4.1.2-1). Figure 4.1.2-2 shows the ionic conduction measurements repeated every 24h after the synthesis of the hydrazine-based metal formate. The behaviour of the ionic conductivity, which is ruled by diffusion mechanism, is optimized only after a certain time after the synthesis. Further, in the first rounds of measurement the arch is slightly distorted departing from the perfect semi-circular shape. The interpenetration of at least two arcs possibly indicates the occurrence of coexisting processes involving mobile ions. The separation of the different contributions in ionic conductivity cannot be reached by the sole analysis of such plots and further experimental investigations would be necessary. Nonetheless, the regular shape of the arc is reached after one day from the synthesis. It is worth to stress that during the whole cycle of measurements the samples did not undergo a phase transition to the perovskite polymorph, since the colour of the pellets was unaltered (see Chapter 3 for details). The ionic conductivity obtained is 4.3 x 10^{-7} S cm^{-1} and 3.4 x 10^{-6} S cm^{-1} for the first and second day respectively. Therefore, experimental evidence clearly indicate that the compound behaves as an ionic conductor at room temperature.

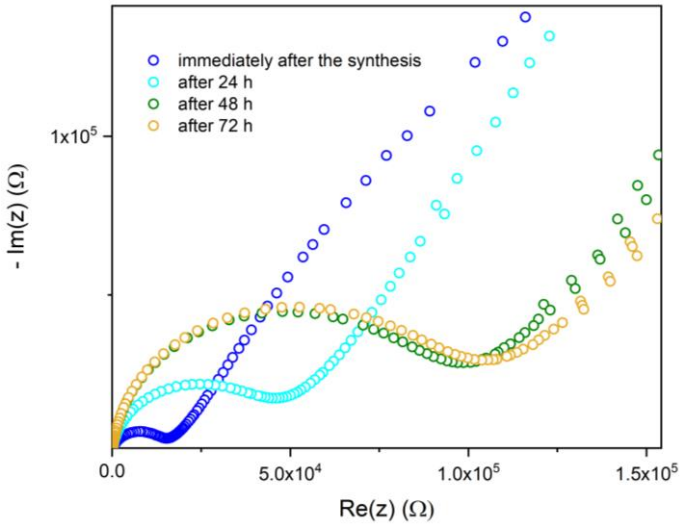

Figure 4.1.2-2: Nyquist plot for perovskite phase of $[NH_2NH_3][Fe(HCOO)_3]$. The plot follows the following sequence: immediately after the synthesis blue line, 24h light blue, 48h green and 72h orange.

Figure 4.1.2-3 reports the conductivity versus time for the $[NH_2NH_3][Fe(HCOO)_3]$ sample recorded during 72 hours in air. The sample shows an ionic conductive behaviour, even if with small values of conductivity, immediately after the synthesis that decreases during the following hours till a stable value at the end of the measures.

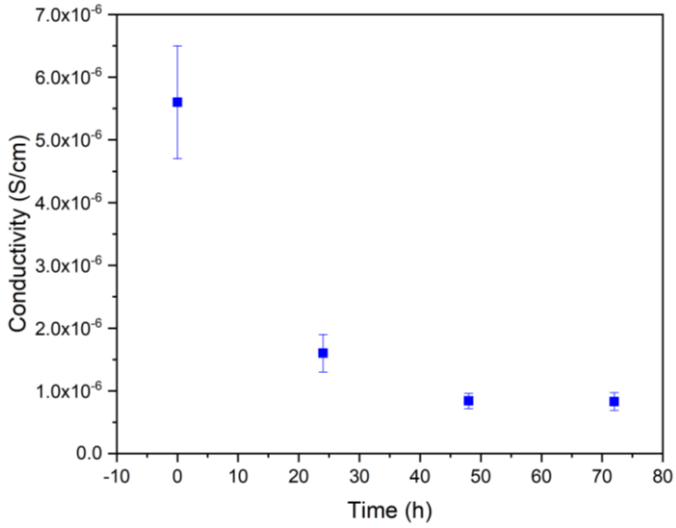

Figure 4.1.2-3: Conductivity versus time for $[NH_2NH_3][Fe(HCOO)_3]$.

So far, the progressive change of conduction property with the exposure to ambient conditions strongly suggests that the high hygroscopicity of the porous material is a key factor. Nevertheless, it is necessary to disclose the nature of the charge carrier and the mechanism of the conduction that it is likely mediated by the adsorbed water.

4.1.3 Ionic conduction in $[NH_4][M(HCOO)_3]$ with M = Mn^{2+}, Fe^{2+}, Co^{2+}

In order to answer to the open question related to the nature of the charge carrier we undertaken ionic conduction experiments on the series of porous metal formates hosting NH_4^+ instead of $NH_3NH_2^+$ due to the fact that ammonium cation is smaller and easy to treat with respect to NH_2NH_3 in terms of interaction with the framework. The first measurements were carried out on samples synthetized by precipitation from methanol using the protocols described for the hydrazine-based compounds.

In Figure 4.1.3-1 the Nyquist plot with the fits for the $[NH_4][Fe(HCOO)_3]$ sample are reported. The fits were made using an equivalent circuit fully explained in the Experimental Methods. The diagram shows the classical ionic conductor behaviour that increasing with the increasing of the time.

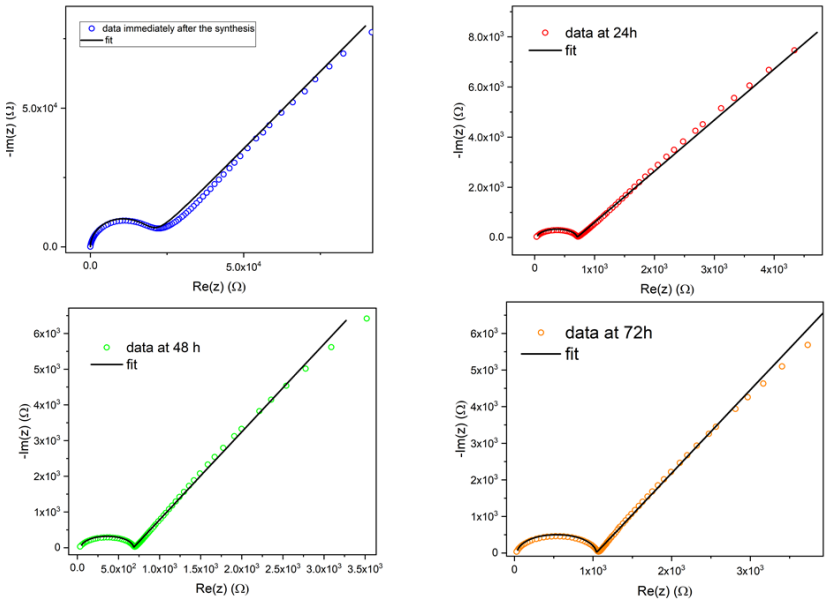

Figure 4.1.3-1: Nyquist plot of $[NH_4][Fe(HCOO)_3]$ recorded immediately after the synthesis and after 24, 48 and 72 hours.

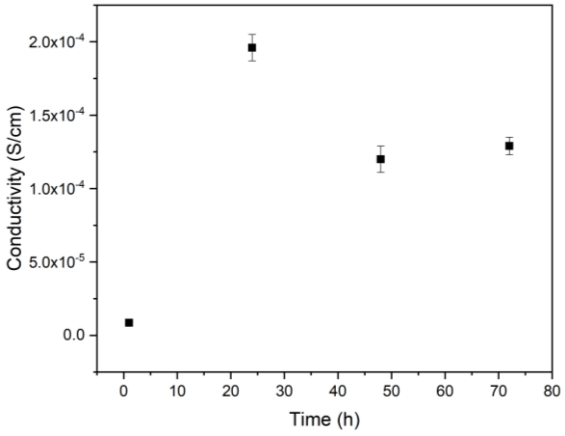

Figure 4.1.3-2: Conductivity versus time of $[NH_4][Fe(HCOO)_3]$.

Figure 4.1.3-2 shows the conductivity trend versus time during the first 72 hours of measurements in which is possible to observe that at the beginning of the process the conductivity is low, after 24 h it reaches its maximum and then it decreases to a constant value.

$[NH_4][Co(HCOO)_3]$ shows a behaviour consistent with the Fe-based counterpart. After a period of three days where the material shows insulating behaviour, the Co-based compound turns into a ion conductor with a continuous improvement of the conduction property over time (Figure 4.1.3-3).

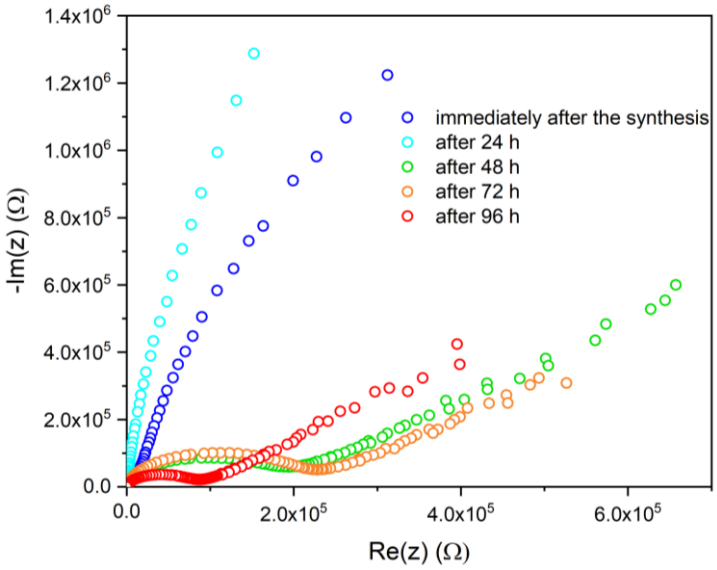

Figure 4.1.3-3: Nyquist plot for $[NH_4][Co(HCOO)_3]$ during five days

As it is possible to observe from Figure 4.1.3-3 the arcs belonging to the measurement performed immediately after the synthesis and after 24 hours are too wide that is impossible to estimate their end. As evidenced in Figure 4.1.3-4, the conductivity values for $[NH_4][Co(HCOO)_3]$ show an overall increment over the course of the time.

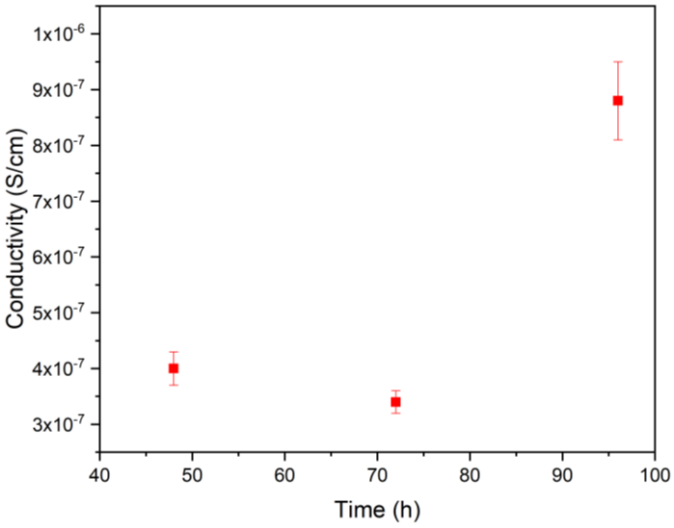

Figure 4.1.3-4: conductivity vs time for $[NH_4][Co(HCOO)_3]$.

$[NH_4][Mn(HCOO)_3]$ shows conductivity in the first 24 h after synthesis. Afterwards the conductivity progressively decreases until the conversion to an insulator state. In Table 4.1.3-1 the ionic conduction values for the first two days are summarized.

Table 4.1.3-1: Conductivity values of $[NH_4][Mn(HCOO)_3]$.

Time (h)	Conductivity (S/cm)	Error
0	$1.12 \cdot 10^{-5}$	$\pm 0.05 \cdot 10^{-5}$
24	$1.13 \cdot 10^{-6}$	$\pm 0.06 \cdot 10^{-6}$

The opposite behaviour of the Mn-based compound could be related to the structural transformation from porous hexagonal to dense orthorhombic framework (see Chapter 2 for details). Nevertheless the $[NH_4][M(HCOO)_3]$ system with M= Fe^{2+},Co^{2+} and Mn^{2+} manifests a robust ionic conductivity at room temperature. In accordance with preliminary results with hydrazine metal formates, humidity conditions alter the conduction behaviour. Apart from the environment conditions, the possible presence of solvent (methanol molecules) partially adsorbed in the porous hexagonal MOFs could be an additional element contributing to the observed conduction behaviour. To further investigate this point, we synthetized a new series

of samples with formula $[NH_4][M(HCOO)_3]$ with M = Mn^{2+}, Co^{2+} via mechanochemistry, to perform a new cycle of ionic conduction measurements. This route of synthesis carried out in dry conditions (no Liquid Assisted Grinding) is useful to figure out the role of the solvent in the ionic conduction behaviour. With this aim, were performed different measurements on two samples of $[NH_4][Mn(HCOO)_3]$: one pellet is exposed to air for several days (Table 4.1.3-2 and Figure 4.1.3-5) whereas the second one is preserved in a glove box under argon-atmosphere. The pellet in dry condition (under Ar) exhibits ionic conduction values three orders of magnitude lower than the sample exposed to ambient condition.

Table 4.1.3-2: Conductivity values of $[NH_4][Mn(HCOO)_3]$ kept in air for four days and synthetized via mechanochemistry.

$[NH_4][Mn(HCOO)_3]$ air	
Time (h)	Conductivity (S/cm)
0	$(6.5 \pm 0.5) \cdot 10^{-5}$
24	$(7.6 \pm 1.4) \cdot 10^{-4}$
48	$(3.3 \pm 0.4) \cdot 10^{-4}$
72	$(2.0 \pm 0.1) \cdot 10^{-4}$

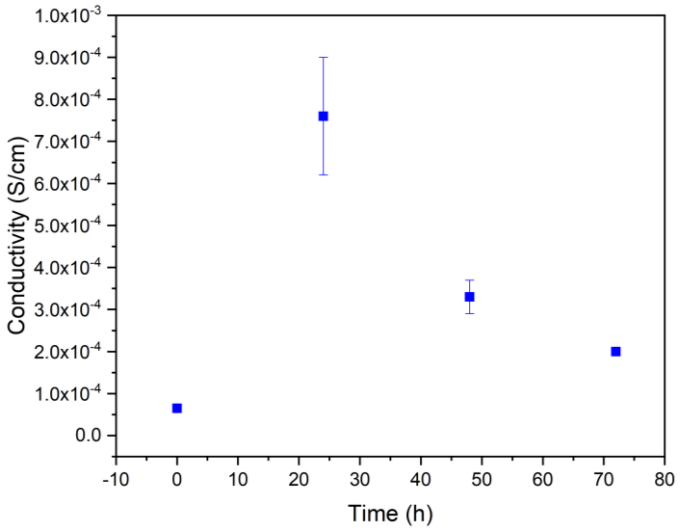

Figure 4.1.3-5: Conductivity vs time of $[NH_4][Mn(HCOO)_3]$ kept in air for four days and synthetized via mechanochemistry.

The same measurements were performed on $[NH_4][Co(HCOO)_3]$. In this case the first measurement was carried out in argon atmosphere and the sample did not show ionic conductivity. After the exposure to air the sample showed ionic conductivity for the next two days of measurements (Figure 4.1.3-6 and Table 4.1.3-3).

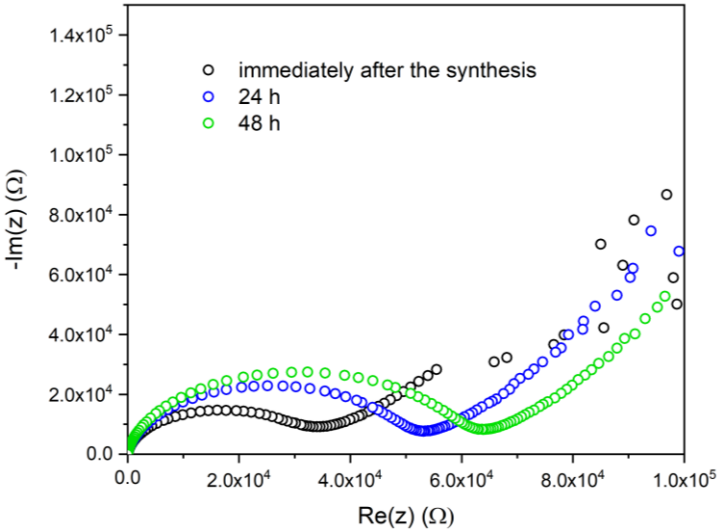

Figure 4.1.3-6: Nyquist plot for $[NH_4][Co(HCOO)_3]$ synthesized via mechanochemistry.

Table 4.1.3-3: Conductivity values of $[NH_4][Co(HCOO)_3]$ synthesized via mechanochemistry.

Time (h)	Conductivity (S/cm)
0	$(1.8 \pm 0.1) \cdot 10^{-6}$
24	$(1.2 \pm 0.7) \cdot 10^{-6}$
48	$(9.9 \pm 0.6) \cdot 10^{-7}$

In Figure 4.1.3-7 is reported the conductivity *versus* time of $[NH_4][Co(HCOO)_3]$; as observed for the previous sample $[NH_4][Mn(HCOO)_3]$, also in this case the ionic conductivity decreases during the 48 hours of measurements, but differently from the last sample, the whole curve does not show any maximum of conductivity value and decrease faster.

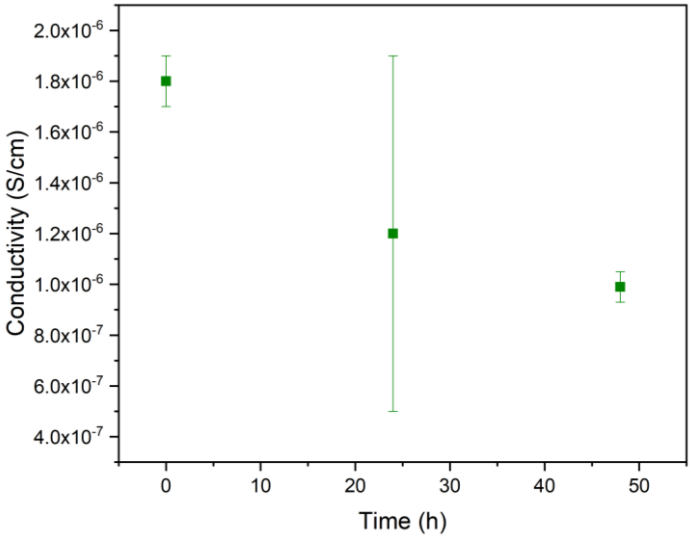

Figure 4.1.3-7: conductivity versus time for $[NH_4][Co(HCOO)_3]$.

Thus, we can conclude that solvent molecules are not responsible for the conduction properties. The observed behaviour is consistent with the previous sessions of measurements performed for the compounds synthesized with the liquid approach. In general, the values of conductivity immediately after the synthesis are low and their increase is observed after leaving the samples exposed to air (with a subsequent decay). It is therefore evident that the exposure to air or the ambient conditions is a mandatory step to trigger the ionic conduction in the whole family.

4.1.4 Humidity-controlled ionic conduction measurements on $[NH_4][M(HCOO)_3]$ and $[NH_2NH_3][M(HCOO)_3]$ with $M = Mn^{2+}, Fe^{2+}, Co^{2+}$

To further investigate the role of the environment humidity in influencing ionic conduction changes, we performed ionic conduction measurements with a controlled fraction of humidity. To this purpose, we prepared a simple experimental set up (Figure 4.2-15a). The level of humidity (RH%) was controlled with an Arduino platform inside a Plexiglas box, the flux of moisture was created insufflating N_2 in water. The sample was located in a plastic box and contacted with nickel foam electrodes held firmly in the plastic support. The nickel contacts were connected to the alligator clip that in turn were directly connected to the instrument (Figure 4.1.4-1b).

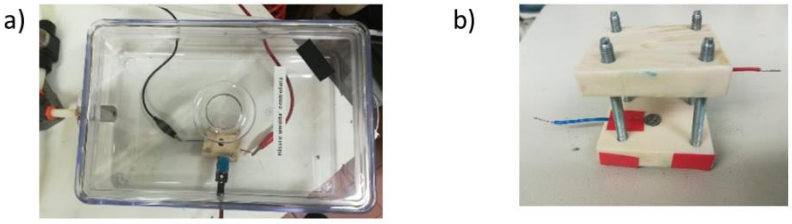

Figure 4.1.4: a) Plexiglas box in which the sample is located together with the electrode and the Arduino; b) plastic box in which the tablets of the samples were located in contact with the nickel foam contacts.

The humidity level in the box was rather stable, and over several hours it varies by a maximum of +/- 3%. A stability problem was, instead, encountered for RH exceeding the 70-75% limit. For each RH value, a different pellet was used coming from the same synthesis batch and stored in argon atmosphere, so that the measurements are not influenced by the sample history. Each pellet was measured at a defined humidity every hour.

The $[NH_4][Mn(HCOO)_3]$ sample were measured at RH=5%, 35%, 50%, 70% and 90%. At RH = 5% and 35% the sample showed a stable insulator behaviour. At RH = 50% the sample started to show conductor behaviour; by reaching the 90% of humidity the sample showed a non-easily understandable behaviour. We suppose that in this case the experimental arc is too small to be measured and this means that we are detecting the water's ionic conductivity (Figure 4.1.4-2). The conductivity value found for RH = 50% was $(7.6\pm0.6)\cdot10^{-5}$ S/cm, instead at RH = 5% and 35% the resistance was too high to be measured and at RH = 90%, prevails the conductivity of the fluid.

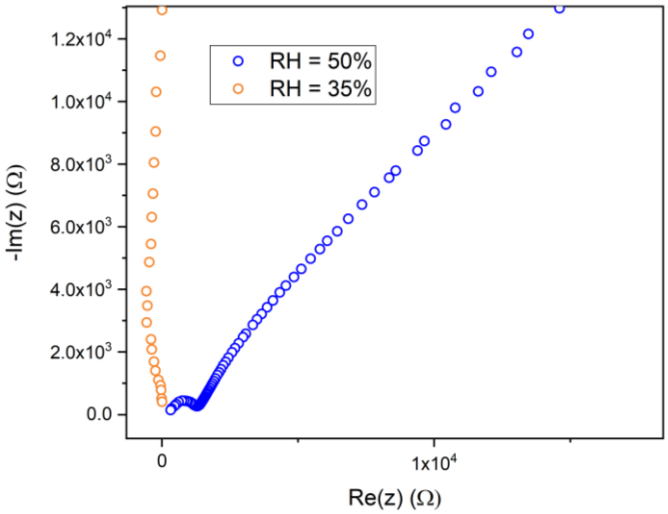

Figure 4.1.4-2: ionic conductive traces for $[NH_4][Mn(HCOO)_3]$ measured at 35% and 50% of humidity.

With RH = 50%, the sample shows an ion conductor behaviour, and it stabilizes after about 1 hour of exposure to humidity (Figure 4.1.4-3). The ionic conductivity values detected at different times graphically reported in Figure 4.1.4-4 the general trend reports a low initial conductivity that reaches a maximum after one hour and then decreases.

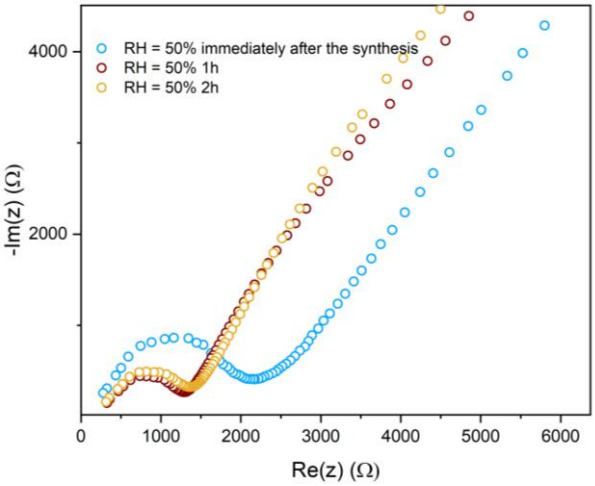

Figure 4.1.4-3: ionic conductor behaviour of $[NH_4][Mn(HCOO)_3]$ at RH = 50% immediately after the synthesis (blue line), 1h (red line) and 2h (yellow line).

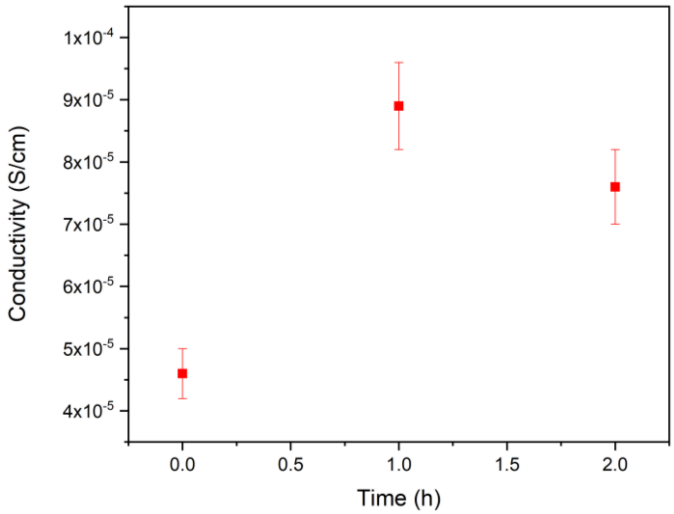

Figure 4.1.4-4: conductivity vs time of $[NH_4][Mn(HCOO)_3]$ at RH = 50%.

For the sample exposed to RH = 70% the behaviour is extremely variable over time. It appears that the sample goes from a state similar to that corresponding to RH = 50% (ionic conductor) to the one observed with RH=90%. Table 4.2-5 reports the ionic conductivity at 70% of humidity during three hours of measurements. The value of conductivity at three hours is missing due to non-measurable data.

Both the samples exposed to RH = 70% and RH = 90% show evident morphological differences with respect to the initial condition. In particular, the sample exposed to RH = 70%, after several hours shows some large semi-transparent crystals on the top of the pellet (Figure 4.1.4-5a). The sample exposed to 90% humidity shows large crystallites on the surface as well. (Figure 4.1.4-5b, 5c).

Figure 4.1.4-5: a) tablet of $[NH_4][Mn(HCOO)_3]$ after exposure at RH = 70%, b) tablet of $[NH_4][Mn(HCOO)_3]$ after exposure at RH = 90% with crystallinities on the surface c) deformation of the tablet of $[NH_4][Mn(HCOO)_3]$ after exposure at RH = 90%.

A stable ionic conductivity characterizes the sample exposed to RH=50%, since below this threshold no ionic conductivity is observed. Exceeding the limit of RH=60% the conduction becomes unstable and recrystallization processes (formate-based compounds are highly soluble in water) seems to occur. The ionic conductivity at RH = 50% is $(7.6 \pm 0.6) \cdot 10^{-5}$ S cm^{-1}.

The same type of measurements were performed on $[NH_4][Co(HCOO)_3]$ at the same values of RH. Figure 4.1.4-6 shows its behaviour at different RH%. As for the ammonium-Mn sample, conductivity is not observable at RH = 5% and, contrary to the Mn sample, the ionic conductivity begins to be detected at RH = 37% ($(9\pm2)\cdot10^{-8}$ S cm^{-1}).

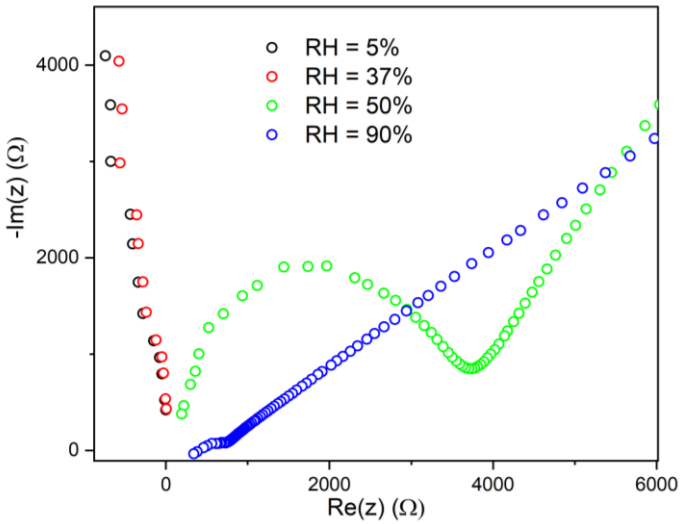

Figure 4.1.4-6: ionic conductive traces for $[NH_4][Co(HCOO)_3]$ at different RH.

As for $[NH_4][Mn(HCOO)_3]$, at RH = 50% the ionic conductivity stabilizes after about 1 hour of exposure to $(2.6\pm0.2)\cdot10^{-5}$ S cm^{-1}. The sample measured at RH = 70% shows unstable behaviour, starting with the typical ionic conduction arc + tail, as already seen for $[NH_4][Mn(HCOO)_3]$ (Figure 4.1.4-7). For the first and the second hour the conductivity was $(3.4\pm0.3)\cdot10^{-5}$ S cm^{-1} and $(1.4\pm0.1)\cdot10^{-5}$ S cm^{-1} respectively, instead for the following two hour it was not possible to measure it.

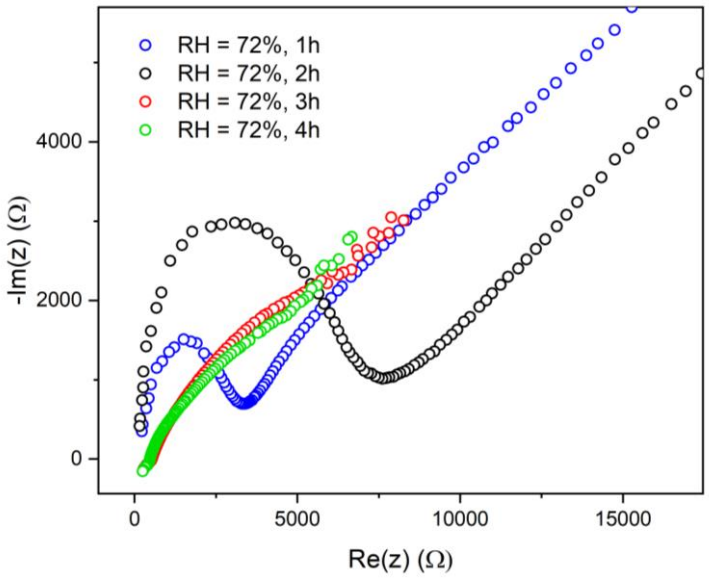

Figure 4.1.4-7: ionic conductive traces for $[NH_4][Co(HCOO)_3]$ at RH = 72% .

Once the measurement with RH=70% is concluded the colour of sample appears to be altered. The PXRD analysis performed on the pellet confirmed the presence of the hexagonal porous formate together with a small quantity of metal formate hydrate $Co(HCOO)_2$ as secondary phase.

As seen, both for $[NH_4][Mn(HCOO)_3]$ and for $[NH_4][Co(HCOO)_3]$, at high values of RH (>80%) the experimental measurements indicate the presence of a fluid ionic conductor and the conductivity value is too high to be measured by the instrument. The almost linear dependence of the imaginary part of impedance versus the real component is not characteristic of an electronic type of conduction. After these measurements, the samples are swollen and the analysis with PXRD diffraction demonstrates the presence of $M(HCOO)_2 \times 2H_2O$ ($M = Co^{2+}, Mn^{2+}$). This compound is well known to be an impurity present in the liquid synthesis especially when abundant quantity of water is present (see Chapter 2). So, as this behaviour occurs when RH exceeds the 80% limit, we conclude that the water absorbed by the samples decompose the framework of $[NH_4][M(HCOO)_3]$ and form the corresponding hydrated formate.

To prove the role of the NH_4^+ cation in the conduction we carried out measurements on samples with formula $CsMn(HCOO)_3$. This compound is isostructural with the hexagonal ammonium-based porous formates, the only

difference is represented by the counter-ion Cs^+ occupying the corresponding sites of the ammonium cation (see Chapter 6 for further details).

The $CsMn(HCOO)_3$ sample was synthesized with the liquid approach and the ionic conduction measurements were performed at RH = 46 and 71% (Figure 4.1.4-8).

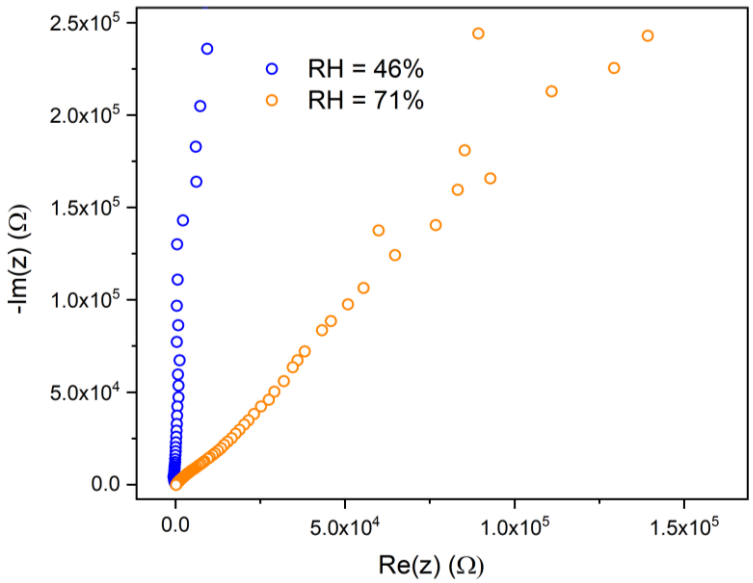

Figure 4.1.4-8: ionic conduction trace for CsMn(HCOO)3 at RH = 46% (blue) and RH =71% (orange).

At RH = 46% the sample shows insulating behaviour, with a resistance higher than 1 MΩ (the maximum resistance values measurable with our set up). For the measurement at RH = 71%, the behaviour of the sample is not easily classifiable. In fact, as it is illustrated in Figure 4.1.4-8, the Nyquist diagram shows a linear dependence of imaginary and real impedance, and no semi-circular curve is detected. This corresponds neither to an electronic conductor, nor to an insulator, nor to an ionic conductor. Typically, an oblique line indicates diffusive behaviour, but it could also indicate a sample with negligible impedance due to ionic conductivity (an arc too small to be observed). The current hypothesis is that the sample at high regimes of RH manifests a limited diffusion of Cs^+ ions likely favoured by the water adsorbed by the pellets.

The effect of the RH on the conduction properties has been measured also on the $[NH_2NH_3][Mn(HCOO)_3]$ compounds in both the chiral and the perovskite polymorphs following the same procedure. In Figure 4.1.4-9 is reported the ionic

conductor behaviour of the chiral phase of $[NH_2NH_3][Mn(HCOO)_3]$ in the range RH = 5 - 50%.

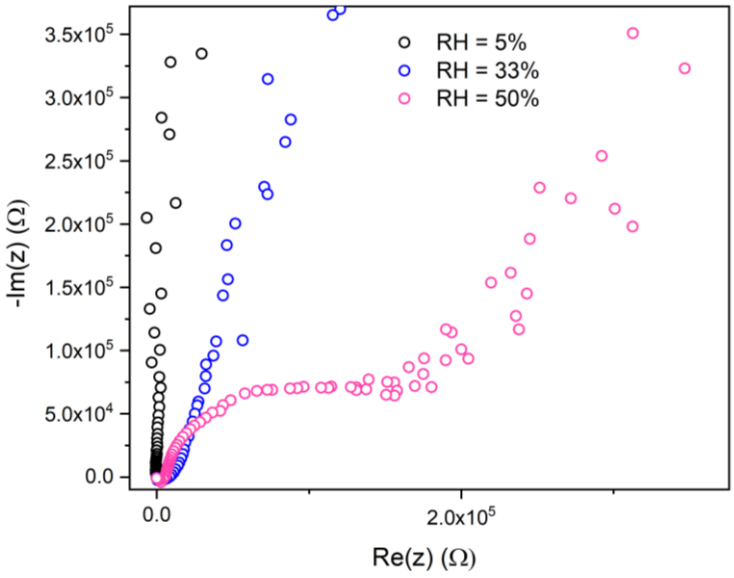

Figure 4.1.4-9: ionic conductor traces for $[NH_2NH_3][Mn(HCOO)_3]$ at RH = 5% (black), 33% (blue) and 50% (purple).

As for $[NH_4][Mn(HCOO)_3]$ also this sample shows ionic conductivity at RH =50% and at lower RH values no ionic conduction is observed. Test were performed also at higher RH, and, exactly as for $[NH_4][Mn(HCOO)_3]$, at RH ~ 77% an ionic conductivity is observed at first, then a signal attributable to the completely wet sample is detected.

For the chiral $[NH_2NH_3][Mn(HCOO)_3]$ polymorph, a measurement was also carried out to verify the reversibility of the process, but with poor results; already at a humidity of about 60%, in fact, the sample showed a typical signal of an excess of water (non-measurable ionic conductivity), and by decreasing the humidity it was notlonger possible to measure ionic conductivity. This is probably due to a degradation of the sample. The ionic conductivity at RH = 50% is equal to $(6 \pm 2) \times 10^{-7}$ S cm^{-1}.

The measurement conducted on the perovskite $[NH_2NH_3][Mn(HCOO)_3]$ sample were carried out to verify whether the channel structure, typical of the chiral phase is fundamental for proton conduction. Tests were performed at RH = 5, 30, 50, 65%. There is an absence of ionic conductivity at RH between 5% and 50%. This

differentiates this sample from those previously measured, since ionic conductivity was already observed at RH = 50%. However, this sample still shows ionic conductivity starting from RH = 65% with an ionic conductivity of (2.6 ± 0.1) x 10^{-7} S cm^{-1} that increases at RH = 78% to (7.0 ± 0.3) x 10^{-6} S cm^{-1}. A very small arc (which corresponds to a high ionic conductivity) is observed at a humidity of 78%, while at 95% the sample shows an atypical signal, attributable to a state in which the sample is completely "wet", and water conduction prevails. Also, in this case the sample differs from the previous ones as in the previous samples already at RH~70% we observed ionic conductivity, while with time it lost the "arc + tail" shape typical of ionic conductors. In the perovskite case this happens at 95%.

The next question we tried to answer is if the process is reversible. The measures, reported in figure 4.1.4-10, were performed using a fresh prepared pellet first testing high level of humidity, then RH is decreased to test the possible reversibility of the conduction mechanism ruled by the humidity level.

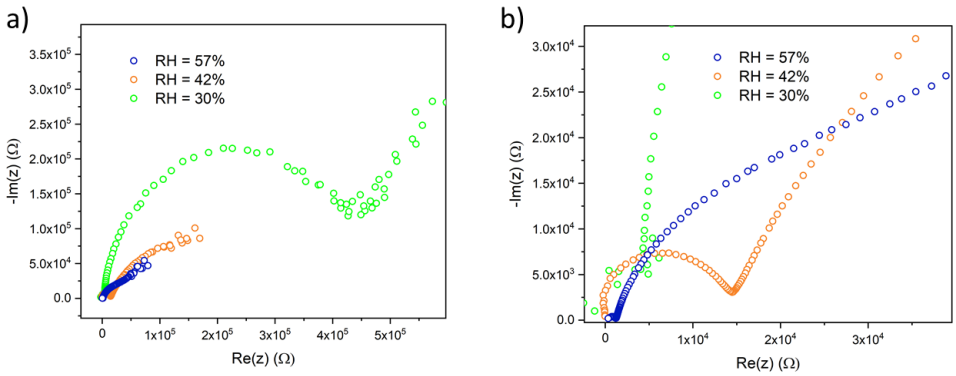

Figure 4.1.4-10: a) Nyquist plot for the ionic conduction reversibility test of $[NH_4][Mn(HCOO)_3]$, b) zoom of the arc area.

The measurements show a certain degree of reversibility of the process, even if not complete. In fact, ionic conductivity is observed (although low) even at RH = 30% value at which it was not observed in the experimental sessions conducted by the progressive increase of the RH level (Figure 4.1.4-11). In any case, it worth to observe that the resistance recorded for the sample at 50% of humidity starting from zero (1500 Ohm) can be placed between the value of resistance measured at 30% and 57% starting from higher level of humidity, demonstrating the partial reversibility of the process.

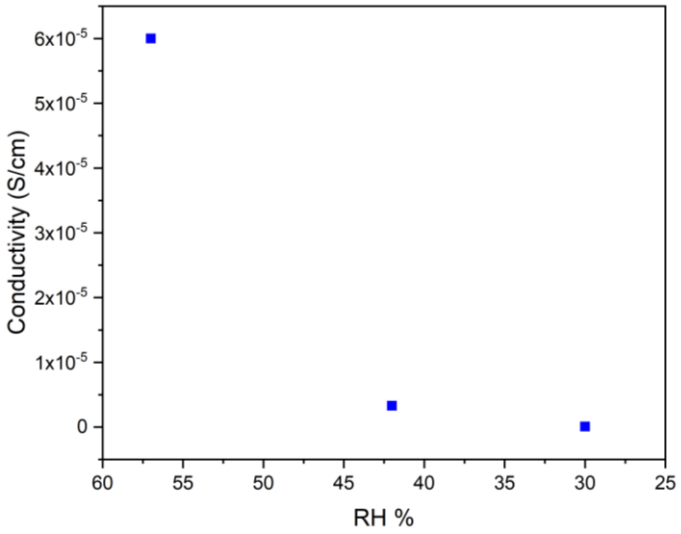

Figure 4.1.4-11: conductivity of [NH4][Mn(HCOO)3] versus RH recorded during the reversibility tests. In these data were not possible to measure the errors.

In conclusion, the $[NH_2NH_3][Mn(HCOO)_3]$ perovskite sample shows ionic conductivity despite the absence of channels in the crystal structure, although it requires higher RH. The reason might be related to the fact that the proton has a certain mobility in the crystalline scaffold even without the channels (as its small size), although probably with a higher activation energy. Unfortunately, to quantify the activation energy, temperature measurements would be necessary, and controlling the temperature and humidity at the same time is almost impossible with the experiment set up at our disposal. The minimum ionic conductivity (at the lower humidity at which ionic conductivity is observed) is much lower than that of ammonium-manganese (2.6×10^{-7} S cm^{-1} against 7.6×10^{-5} S cm^{-1}). The chiral $[NH_2NH_3][Mn(HCOO)_3]$ sample has similar behaviour to chiral ammonium-manganese and chiral ammonium-cobalt, although it does not exhibit reversibility (possibly due to transition to perovskite, or degradation). The ionic conductivity at 50% humidity is much lower than that of ammonium-manganese (6×10^{-7} S cm^{-1} against 7.6×10^{-5} S cm^{-1}).

4.2 Discussion of the results

Our experimental results demonstrate that the ammonium-formate compounds $[NH_4][M(HCOO)_3]$ (M = Mn^{2+}, Co^{2+}) in the chiral polymorph and both the chiral and perovskite polymorphs of the hydrazine-formate compounds $[NH_2NH_3][M(HCOO)_3]$ (M = Mn^{2+}, Fe^{2+}) show ionic conductive behaviour.

This behaviour is already present at ambient conditions and increases with increasing the ambient humidity, thus, we speculate that the material show proton conductive behaviour of the first type. In literature ammonia is already known as a promising conducting media [126] due to its low auto ionization constant (2.2 x 10^{-28} at 25°C). Although, liquid NH_3 possess low ionic conductivity (resistance of 10^{-11} Ω^1) [127, 128, 129h] and when the conductivity of NH_3 is due to the presence of NH_4^+ ion it is still lower than the one of the H_3O^+ (142 S cm^2 mol^{-1} *versus* 350 S cm^2 mol^{-1}), ammonia is advantageous for different reasons, such as the already well-established infrastructures able to manage, storage and transport it. Despite these advantages, its corrosive gas phase represents a clear drawback. To overcome this issue, NH_3 as conducting media has been introduced in materials as host molecule or in its protonated form, NH_4^+, in metal-organic frameworks (MOF) or coordination polymers.

The mobility of NH_4^+, when present together with NH_3 (called degenerate systems), is 0.94 ± 0.35 cm^{-1} s^{-1} V^{-1} which is lower than H^+, Li^+ or OH^- [130], nevertheless thanks to the good H-bond network that it can stablish, the proton conduction is facilitate. The effective role of the NH_4^+ ion in the proton conduction has been studied by Sadakiyo and co-workers [121], who demonstrated that the substitution of the ammonium cation with K^+ in the porous structure of $(NH_4)_2(H_2adp)[Zn_2(ox)_3]\cdot 3H_2O$ (H_2adp=adipic acid), can significantly reduce by two orders of magnitude the proton conduction. These results demonstrate two main points: the importance of the ammonium cation for increasing the proton carrier concentration, and the role of the H-bonds made with the neighbouring molecules during the proton transfer. Another interesting example on how ammonium cation can be encapsulated in chemical frameworks and act as proton conductor is in $(NH_4)_4[MnCr_2(ox)_6]$ x $4H_2O$ [131]. The framework structure is formed by an oxalate-bridged bimetallic chiral 3D anionic network that incorporate ammonium cations and water molecules in the same channel. This arrangement guarantees a high proton conduction at room temperature (2.4 x 10^{-9} S cm^{-1} at RH = 9%) that increases to 1.1 x 10^{-3} S cm^{-1} at RH = 96%. This result reiterates the importance of the H-bond network in the proton conduction in the Grotthuss mechanism. Moreover, the authors suggest that the structure of the cavity, which host the ammonium cation and the water molecule that participate to the H-bond network, together with the oxalate molecule, can open new routes for the proton conduction triggered by humidity.

In the case of the ammonium-formate compounds analysed in this work, the proton conduction is most likely triggered by moisture and follows the Grotthus mechanism, according to which the proton hops between ammonium cations thanks to the hydrogen bond network in the channels. In particular, at a critical relative humidity value, the conductive process is activated by the water molecules present

in the ambient. We propose that NH_4^+ cation donates its proton to the water absorbed by the sample (that act like a base) and this create a vacancy in the H-bond framework which facilitate the hopping of the proton through the channels of the structure. (Figure 4.2-1).

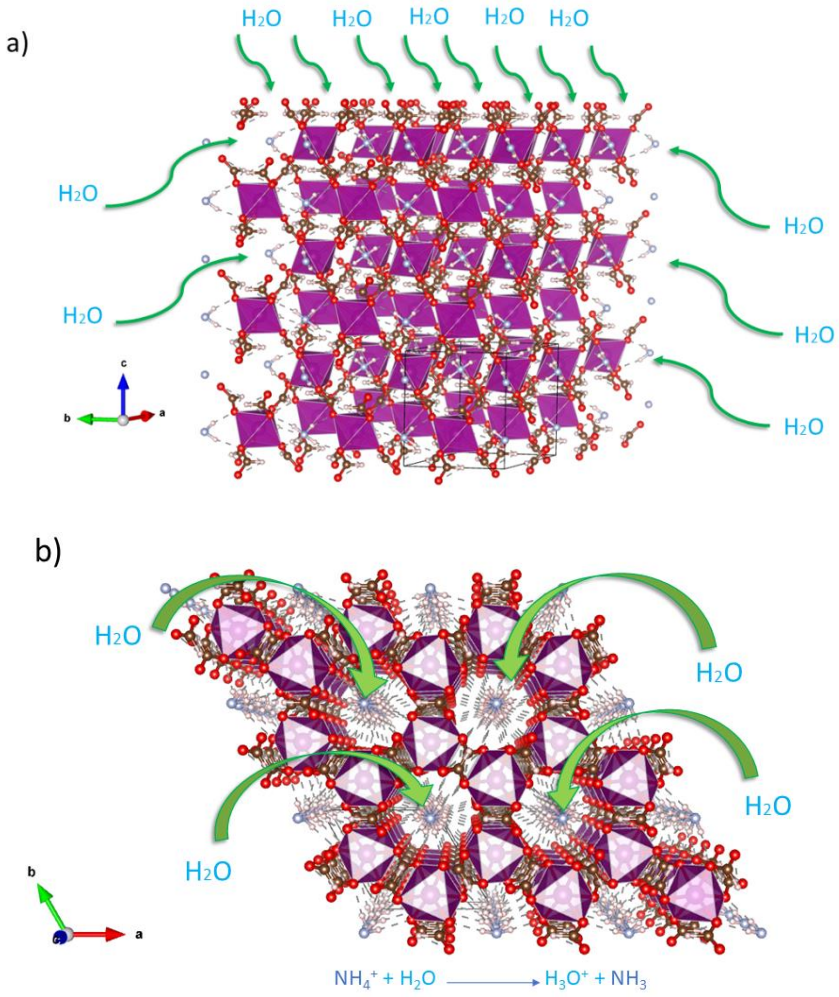

Figure 4.2-1: Steps of the ionic conduction mechanism. a) absorption of water by the framework b) proton transfer from the ammonium cation to the water molecule.

A similar conduction behaviour to the ammonium based formate has been detected also for the $[NH_2NH_3][M(HCOO)_3]$ compounds with M= Fe^{2+}, Mn^{2+} both for the chiral and the perovskite structure. For what concerns the chiral polymorph, as it possesses channel in the structure, it is not surprising a similar behaviour to the ammonium-based samples, but for what concerns the perovskite polymorph it is difficult to explain the real nature of the conductivity. Nevertheless, we speculate that also in this case the proton possesses a certain mobility which allows it to migrate in the perovskite structure through H-bond paths. As the perovskite does not contain channels like the chiral structure, the migration is more difficult and, in fact, the conduction is triggered at higher level of humidity with a lower conductivity compared to the ammonium-based samples.

It is now worth discussing the different conduction behaviours depending on the metallic species present in the framework. For what concerns the ammonium-based samples, it is possible to compare the data of $[NH_4][Mn(HCOO)_3]$ with $[NH_4][Co(HCOO)_3]$. The first notable observation is that the ionic conduction in the Co-based sample activates at a lower level of RH compared to the Mn-compounds (37% *vs* 50%) even if with lower conductivity value ($9 \pm 2 \times 10^{-8}$ S cm^{-1} for Co-based *vs* $7.6 \pm 0.6 \times 10^{-5}$ S cm^{-1} for Mn-based). The conductivity at RH = 50% of $[NH_4][Mn(HCOO)_3]$ is slightly higher than for the Co counterpart, in fact after one hour their values are respectively $7.6 \pm 0.6 \times 10^{-5}$ S cm^{-1} and $2.6 \pm 0.2 \times 10^{-5}$ S cm^{-1}.

Interestingly, at RH ~ 70% it is possible to observe an opposite behaviour in the two compounds. The Mn-based compound increases its conductivity during time of one order of magnitude (but then decreases after two hours), instead the Co-based compound decreases its conductivity, even if maintaining the same order of magnitude. This could be explained keeping in mind that the Mn-based compound is a better ionic conductor (as seen from the previous data) and, as it is more sensitive to moisture, its conductivity increases with the increasing of the RH till 70% where ions conductivity phenomenon take place. On the contrary, the Co-based compound seems to decrease its conductivity in a constant way. In summary, by comparing the results on these two samples, we can conclude that $[NH_4][Mn(HCOO)_3]$ demonstrates an higher conductivity that increases during the first two hour of measurements, even if with a higher level of humidity needed to start the conduction process. On the other hand, $[NH_4][Co(HCOO)_3]$ shows slighter lower conductivity that decreases with time, but the activation of the process require a lower humidity value. The higher conductivity has been detected for the $[NH_4][Mn(HCOO)_3]$ samples, which reaches $2.9 \pm 0.3 \times 10^{-4}$ S cm^{-1} at RH = 50% after two hour of exposure.

It is also interesting to compare the conductivity and the behaviours of the chiral and the perovskite polymorphs of the $[NH_2NH_3][Mn(HCOO)_3]$ samples. By analysing the data, it is possible to observe that for the chiral polymorph the process is activated at a lower level of humidity compared to the perovskite polymorph (50% *vs* 65%), but the conductivity of the chiral polymorph degrades sooner at RH = 77%, instead the perovskite at much larger values around RH = 95%. This behaviour can be attributed to the higher stability of the perovskite structure, moreover its denser structure (compared to the chiral polymorph) requires a higher humidity level to activate the conductivity, indeed, its conductivity increases from RH = 77% to RH = 95%, level of humidity at which the conductivity for the other polymorph was no longer measurable. However, it is worth stressing that the conductivity value reached for the chiral polymorph is $10^{-5}/10^{-4}$ S cm^{-1}, instead the perovskite reaches $10^{-6}/10^{-7}$ S cm^{-1}; that suits with the fact that in the chiral structure the channel can favour the proton transfer, instead in the perovskite this process is partially inhibited by the presence of different paths Reversibility tests performed on these two structures, starting from high level of RH to lower level, showed that the perovskite phase conducts till at RH = 30% (even with low conductivity), instead the chiral phase till 60% confirming the higher stability of the perovskite polymorph. It is worth to observe that comparing the chiral polymorph of $[NH_2NH_3][Mn(HCOO)_3]$ with $[NH_4][Mn(HCOO)_3]$, the hydrazine-based sample at RH = 50% showed a conductivity of 6 ± 2 x10^{-7} S cm^{-1}, two orders of magnitude lower than the ammonium-based sample. Even though both the materials possess channels, it is notable that in the hydrazine compound the cation is anchored in a stronger way compared to the ammonium compound. This is because it possesses more hydrogen atoms, and thus it can make more H-bonds, but also because these bonds are shorter (compared to the one of the ammonium) and thus stronger, making the proton exchange more difficult.

As already remarked, in literature are present many examples of materials that show proton conduction at different level of humidity. The conductivity values obtained in our studies are in agreement to the one reported for other compounds that showed proton conduction behaviour [126] with a conductivity in a range between 10^{-3} and 10^{-8} S cm^{-1}. In particular, most of the material that possess ionic conduction behaviour, show considerable conductivity values at high level of RH, often higher that 90% and/or at temperatures higher than RT [126, 131]. Differently from the known materials, $[NH_4][M(HCOO)_3]$ (with M = Mn^{2+}, Co^{2+}) and partly $[NH_2NH_3][M(HCOO)_3]$ (with M = Fe^{2+}, Mn^{2+}), show ionic conduction at a significant lower RH (50% or 37%) and room temperature. Moreover, the conductivity value reached by the formate samples at these values of humidity is higher by some order of magnitude compared to other materials [126, 120, 131]. In fact

$[NH_4][Mn(HCOO)_3]$ can reach a conductivity of $2.9 \pm 0.3 \times 10^{-4}$ S cm^{-1} at RH = 50%, a level of humidity at which other materials show a conductivity of 10^{-6} S cm^{-1} [131].

In conclusion, the ammonium-formate-based compounds $[NH_4][M(HCOO)_3]$ (with M = Mn^{2+}, Co^{2+}) and partly the hydrazine-formate-based compounds $[NH_2NH_3][M(HCOO)_3]$ (with M = Fe^{2+}, Mn^{2+}) showed proton conductivity. The mechanism by which the conduction occurs is not completely clear and should be investigate deeper in the future. However, we speculate that the proton conductivity is due to the H-bond network in the channel, and it is activated by the water absorbed by the material. The main advantage of the ammonium-based formate with respect to other material present in literature that show similar conduction behaviours is related to the much lower value of RH needed to activate the conduction and to the larger value of proton conduction observed at RT and low RH. These characteristics suggest the ammonium-formate materials as a possible new class of proton conductors and will spur the research and interest of the research community.

5 CESIUM FORMATE COMPOUNDS

5.1 Introduction to alkali formate compounds

Beside the classical metal formate compounds with general formula $[Am^+][M(HCOO)_3]$ (Am^+ = organic ammine), in literature are present examples of other metal formate in which the ammine is replaced with an alkali metal, like for example in $Na_3[Mn_3(HCOO)_9]$ [132] (Figure 5.1-1).

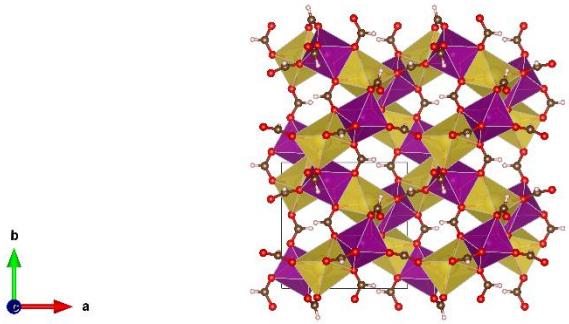

Figure 5.1-1: Crystal structure of $Na_3[Mn_3(HCOO)_9]$ viewed along the c axis. Purple colour indicates the manganese atoms, yellow sodium, brown carbon, red oxygens and white hydrogen.

$Na_3[Mn_3(HCOO)_9]$ is obtained in solvothermal conditions using dimethylformamide (DMF) as solvent. It crystallizes in the chiral cubic space group $P2_13$ and the chirality is originated by the presence of only one enantiomer of $M(HCOO)_6$. In the structure both manganese and sodium atoms are octahedrally coordinated by the formate anions in *syn-anti* mode, and the Manganese atoms form triangular Mn_3 building blocks. Differently from $[NH_4][Mn(HCOO)_3]$, the structure does not present channels and the sodium ions are well blocked and not free to move. The material shows antiferromagnetic character with an interesting behaviour with applied field lower than 1.0 kOe, where the magnetic susceptibility become irreversible with maxima at 22 and 34 K, due to the frustrated structure composed by trigonal arrangements of interacting magnetic moments [132].

Later, in 2014, other alkali-based compounds have been synthesized such as $Na[Mn(HCOO)_3]$,$K[Mn(HCOO)_3]$, $Na_2[Cu_3(HCOO)_8]$ and $K_2[Cu_5(HCOO)_{12}]$ [16] using different methods. $K[Mn(HCOO)_3]$ crystallize in the monoclinic space group *C2/c*. The crystal structure is similar to the already reported for $Na_3[Mn_3(HCOO)_9]$, as the Mn^{2+} atoms are octahedrally coordinated to the formate anion, but in this case four are in *syn-anti mode* and two *via anti-anti* mode. The four adjacent Mn

octahedra, connected to form a twisted square does not lead to spin frustration. The potassium ion is bonded to two manganese atoms through the oxygens of three different formate anions [16].

$Na_2[Cu_3(HCOO)_8]$ crystalize in the triclinic space group *P*-1; it has a paddle-wheel structure with a di-nuclear copper-formate complex, in which two equivalent copper ions are coordinated to four formate anions in *syn-syn,* mode. Each sodium ion is coordinated by seven oxygen atoms. The structure is formed by an infinite chain of mononuclear and a binuclear Cu^{2+} ions coupled by the formate anions, situation rarely seen in Cu(II) formate complexes [133]. The mononuclear Cu^{2+} is located at the inversion centre of the structure and exhibits Jahn-Teller distortion [16].

The structure of $K_2[Cu_5(HCOO)_{12}]$ belongs to the *Pbca* orthorhombic space group. It presents three different Cu(II) sites, two of them as trinuclear chain, instead one as mononuclear. One of them is octahedrally coordinated and located on the inversion centre of the structure. Formate anions are coordinated to the Cu^{2+} ion in both *syn-syn* and *syn-anti* mode, depending on the copper ion.

Another example of these formate compound is $K[Co(HCOO)_3]$ [17] for which the authors report two polymorphs. The first is isostructural to the $[NH_4][M(HCOO)_3$ series (with M = Mn^{2+}, Fe^{2+}, Co^{2+}, Ni^{2+}, Mg^{2+}, Zn^{2+}) with the $P6_322$ space group; this is not surprising, as the potassium ion has both charge and dimension similar to the ammonium, except for the fact that it cannot form H-bonds, thus its templating role is different. In fact, it can form stable connections with the oxygens belonging to the formate anions, consequently the structure is formed by an anionic framework of $[Co(HCOO)_3^-]$ units that forms cavities along the *c* axis in which K^+ in located. As the cell parameters of $K[Co(HCOO)_3]$ are smaller than $[NH_4][M(HCOO)_3$, also the formed channels are smaller (*ca.* 2.1 A *vs ca.* 3.1 A). Co ···Co distance, Co-O bonds and O-Co-O angles are similar to the one reported for $[NH_4][M(HCOO)_3$. Moreover, the K^+ ion, that is coordinated with six $HCOO^-$ (or chelated by three O-Co-O group) form highly distorted and compressed KO_6 octahedra, characterized by small O-K-O angles, and K-O lengths comparable to the ones reported for HCOOK. This particular situation is probably the main reason for the instability of $K[Co(HCOO)_3]$ [17]. This polymorph doesn't show the paraelectric-ferroelectric transition observed for $[NH_4][M(HCOO)_3$ and only an expansion of the *c* axis was observed when cooling, as similarly observed for $[NH_4][M(HCOO)_3$. The second polymorph of $K[Co(HCOO)_3]$ crystallizes in the monoclinic *C2/c* space group (Figure 5.1-2). The anionic framework might be compared to a highly distorted perovskite, in which the K^+ ion is arranged in zig-zag chains [17]. The changing of coordination of the formate anions increases the packing of the structure, giving a denser phase (2.338 cm^{-1} with packing coefficient of 0.836 *vs* 2.157 cm^{-1} and 0.786) [17]. This is consistent with what

found for $Na[Mn(HCOO)_3]$, where the transition metal is large and the alkali metal is small, with consequently *syn-anti* coordination of the formate anions to reach the maximum effective packing [132]. In this polymorph the K^+ ion is coordinated by eight oxygen from the $HCOO^-$ anions, forming a KO_8 moiety with distorted tetragonal antiprism [17].

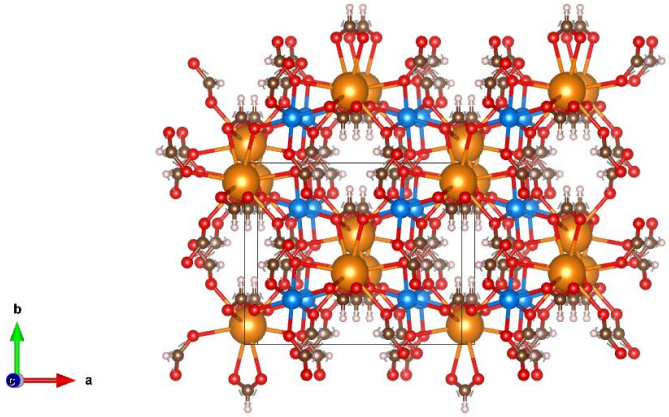

Figure 5.1-2: crystal structure of K[Co(HCOOH)3. K atoms are in orange, Co atoms in blue.

Briefly, the transformation between the two polymorphs has been observed both in solution and at the solid state and occurs spontaneously. The most important differences between the two polymorphs regards the coordination number of K, that passes from six to eight. Even though in the first polymorph the KO_6 octahedra are compressed, the change to a higher, more stable, coordination number for K^+ could play an important role in facilitating the transition [17]. Moreover, the authors observed that the first polymorph is obtained in concentrated solution, instead the second in diluted one. In fact, they observed that when crystals of the first polymorph are already formed, the solution is so diluted to allow the formation of the second polymorph, thus, when solutions are preserved for long time, the first polymorph is re-dissolved and the formation of the second is favoured. This demonstrate that the first polymorph is the kinetic and the second the thermodynamic one [17].

Other examples of alkali metal-formates are those belonging to the series: $AB(HCOO)_3$ with A = Rb^+, Cs^+ and B = Mn^{2+}, Co^{2+}, Ni^{2+} [5]. $RbMn(HCOO)_3$ is the only compound of the series that crystallize in the monoclinic C2/c space group (Figure 5.1-3), while the remaining adopt the chiral hexagonal $P6_322$.

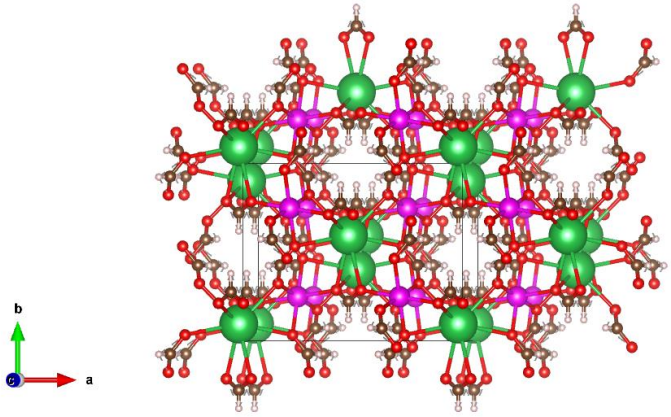

Figure 5.1-3: crystal structure of $RbMn(HCOO)_3$. Green and pink atoms are Rb and Mn respectively.

The $RbMn(HCOO)_3$ structure is formed by highly distorted MnO_6 octahedra in which half of the formed channels, along the *c* axes, are occupied by the Rb^+ cations. The four equatorial formate anions that coordinates the manganese atoms are linked in *syn-anti* mode, instead the two axials in *anti-anti*.

5.2 Cesium formate compounds

With the aim to synthesize new formate we tried to synthesize $CsMn(HCOO)_3$. This sample has also turned out to be a key point to confirm the ionic conductive behaviour of the formate compounds with general formula $[Am^+][M(HCOO)_3]$ with Am = NH_4^+, $NH_2NH_3^+$ and M = Mn^{2+}, Co^{2+}, Fe^{2+} (see Chapter 2 and 3 for details).

The first successful synthesis of formate compound containing caesium, has been reported by Saines and co-workers in 2015 [18]. It belongs to a series of isostructural alkali formate compounds: $RbCo(HCOO)_3$, $RbNi(HCOO)_3$, $CsMn(HCOO)_3$, $CsCo(HCOO)_3$ and $CsNi(HCOO)_3$.

The first attempt of synthesis was performed at the liquid state, using Cs_2CO_3 as source of caesium and $MnCl_2$ x $4H_2O$ as source of manganese. The formate was provided by the formic acid and the solvent was methanol. After two days colourless little crystals were grown at the interface of the two solutions and on the bottom of the tube. The phase was analysed with PXRD diffraction, and the obtained pattern has been compared to the one present in literature with a Le Bail fitting confirming the purity of the phase.

$CsMn(HCOO)_3$ were also synthesized by the mechanochemical approach following the reaction:

$$Mn(HCOO)_2 + Cs(HCOO) \rightarrow CsMn(HCOO)_3$$

The synthesis was performed by pre-treating $Mn(HCOO)_2$ in the oven at 353 K for 45 min, then a stochiometric amount of the powders were mixed in the jar. The starting reagents were grounded for four sessions of machination of five minutes each.

The final powder has been characterized by PXRD diffraction and the fitting confirms the purity of the phase (Figure 5.2-1). The fitting was carried out by using the published crystal structure with $P6_322$ space group. The cell parameters are reported in Table 5.2-1.

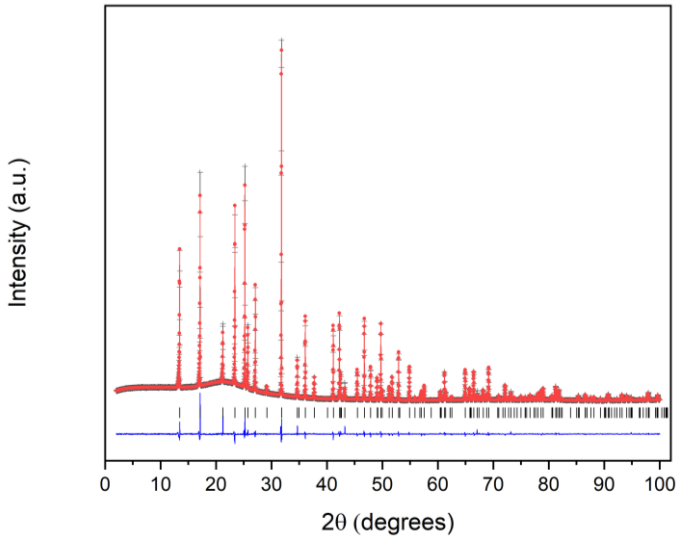

Figure 5.2-1: refinement of the structure of CsMn(HCOO)3 at 298.15 K. Black crosses, red line and blue line indicates the observed, calculated and difference data respectively, whereas the tick marks indicate the Bragg position of the main phase. The reliability factors of the refinement are Rp = 2.21, wRp = 3.60

Table 5.2-1: cell parameter obtained from the fitting of the structure of $CsMn(HCOO)_3$ at 298.15 K.

Axis	Length (Å)
a	7.591981(6)
b	7.591981(0)
c	8.364631(7)
α, β, γ	90 90 120
V(Å^3)	417.5299
Density (g/A^3)	0.77
Source	Cu Kα
Rp, Rwp (%)	2.21, 3.60

The sample has been characterized also by DSC and TGA analysis (Figure 5.2-2).

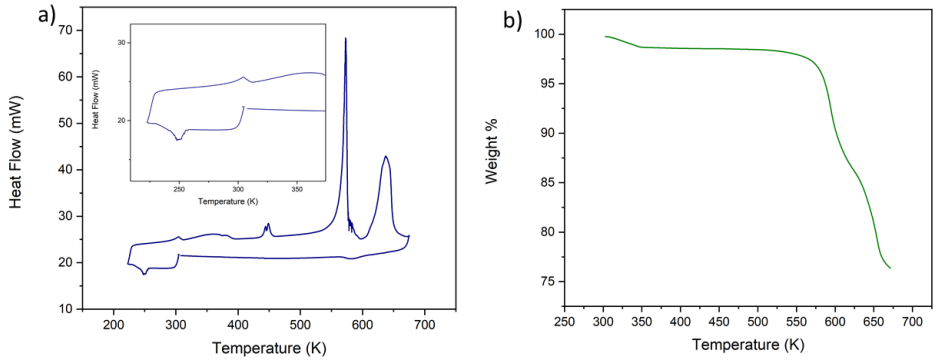

Figure 5.2-2: a) DSC trace of Cs $CsMn(HCOO)_3$, the inset show a zoom at low temperatures b) TGA trace of $CsMn(HCOO)_3$.

The TGA is in agreement with the one reported in literature in nitrogen atmosphere [18]. The first slight loss of weight is detected at about 350 K in the TGA and corresponds to a broader bump in the DSC trace, probably due to the loss of water adsorbed from the ambient. At 550 K the abrupt change of weight is ascribed to the decomposition of the sample in caesium oxalate and MnO, as similarly reported for $K[Co(HCOO)_3]$ [17]. The following two losses of weight at 600 and 675 K are consistent with the beginning of the decomposition of the oxalate [18]. These two events are compatible with the two prominent peaks found in the DSC trace.

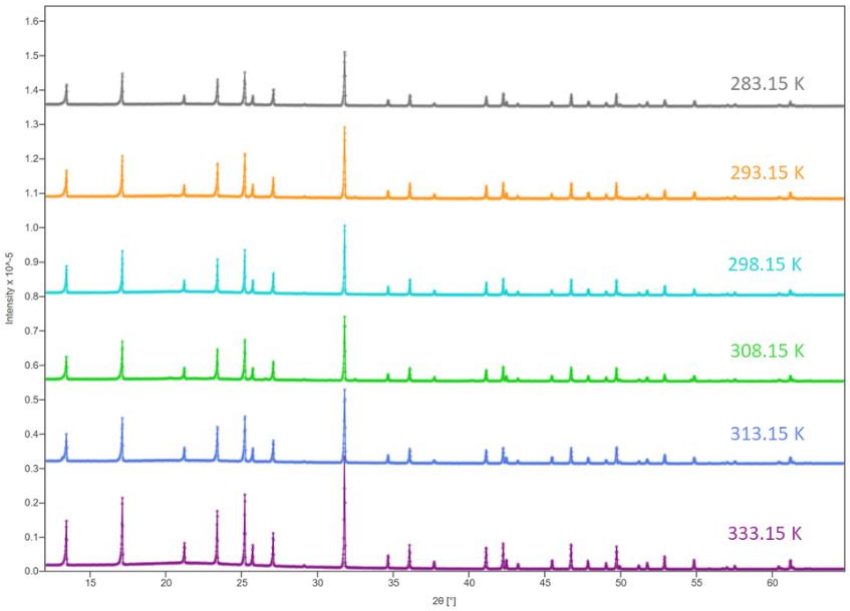

Figure 5.2-3: sequence of PXRD patterns recorded above RT for $CsMn(HCOO)_3$.

The DSC trace also show a thermal event at 233 K on cooling and 303 K on heating. This anomaly has never been reported for $CsMn(HCOO)_3$ and any alkali formate compound, thus we decided to investigate this with PXRD diffraction at different temperature. The diffraction experiments were performed in transmission geometry with a STOE diffractometer equipped with a sample holder for capillaries (see Experimental Methods). The powder has been inserted in a capillary of 0.2 mm. The PXRD data (Figure 5.2-3) were reordered at: 283.15, 295.15, 298.15, 308.15, 313.15, 333.15 K (HT series).

Moreover, we performed XRD experiments from room temperature to 210 K (LT series) and the resulting patterns are reported in Figure 5.2-4.

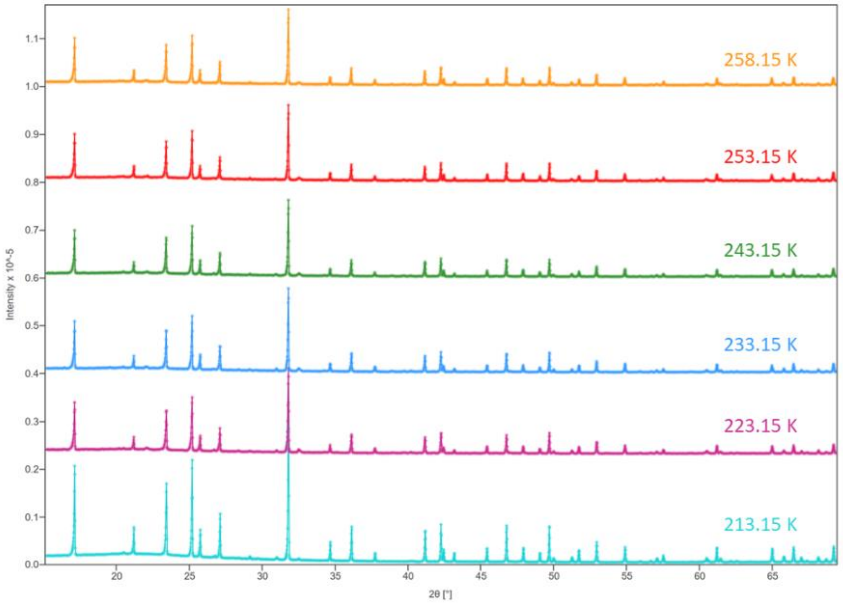

Figure 5.2-4: sequence of PXRD patterns recorded at LT for $CsMn(HCOO)_3$. Extra peaks are in arrange from 20 to 41 2θ and at 53 2θ.

As it is possible to observe, at HT the PXRD patterns are almost unvaried, instead, the LT sequence shows some new peaks. In Figure 5.2-5 it is reported the comparison between the PXRD pattern recorded at 283.15 and 213.15 K.

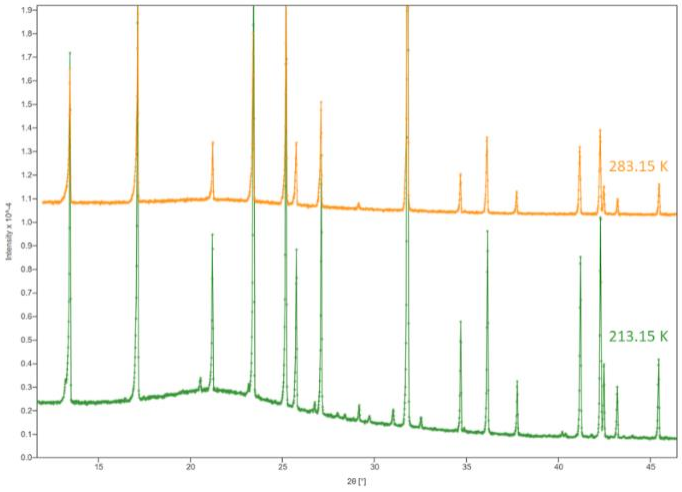

Figure 5.2-5: comparison between PXRD pattern of $CsMn(HCOO)_3$ recorded at 283.15 K and 213.15 K. The extra peaks can be found at 20 2θ, in the range 26-34 2θ and from 40 to 44 2θ.

The comparison clearly shows the presence of new weak peaks in the LT phase of $CsMn(HCOO)_3$. Such peaks seemingly indicate that the thermal event observed in the DSC analysis is associated to a structural distortion of the Cs-based formate. The refinement of the structure both at 298.15 K and 333.15 K are in agreement with the literature (the atomic coordinates are reported in the Experimental Methods on Table 7.9-6). Conversely, the fitting of the diffraction data collected at 213.15 K is more difficult due to presence of the extra peaks (Figure 5.2-6). The cell parameters are reported in Table 7.9-7 of the Experimental Methods.

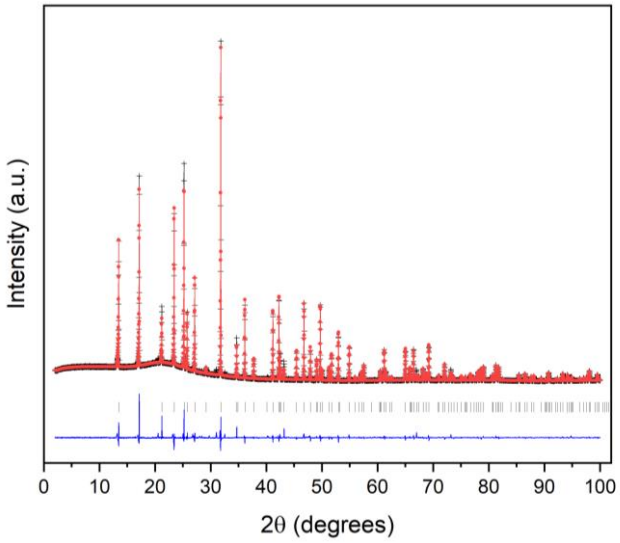

Figure 5.2-6: refinement of the structure of CsMn(HCOO)3 at 213.15 K. Black crosses, red line and blue line indicates the observed, calculated and difference data respectively, whereas the tick marks indicate the Bragg position of the main phase. The reliability factors of the refinement are Rp = 2.75, wRp = 4.45.

Table 5.2-2: cell parameter obtained for $CsMn(HCOO)_3$.

Axis	Length (Å)
a	7.584340(8)
b	7.584340(0)
c	8.372194(1)
α, β γ	90 90 120
V(Å^3)	417.0665
Density (g/A^3)	0.77
Source	Cu Kα
Rp, Rwp (%)	2.75, 4.45

Apart from the presence of extra-peaks, the fitting results difficult for the selective broadening of some reflection associated to the hexagonal phase.

To further investigate the low temperature transition, electron diffraction (TEM) analysis has been performed below 215 K. Precession-assisted 3D ED were performed with the Zeiss Libra 120 transmission electron microscope working at 120 kV and equipped with a LaB_6 thermionic source at the National Enterprise for nanoScience and nano Technology in Pisa. Sequential electron diffraction patterns were collected in nanodiffraction mode with a parallel beam of 150 nm, obtained by selecting a condenser aperture of 5 μm. Data were energy-filtered on the zero-loss peak with an in-column Ω-filter and a slit width of about 20eV [134, 135]. The diffraction patterns of Figure 5.2-7 are characterized by satellites suggesting the occurrence of structural modulation. Attempts to determine the periodicity of such incommensurate distortion has failed due to the limited diffraction data recorded in each session. Unfortunately, the crystals of the Cs-based phase are strongly damaged by the electron beam, even using mild conditions. This is compatible with the fact that TEM studies on the class of hybrid formates are still absent in literature. Therefore DSC, XRD and TEM analysis at low temperature strongly indicate the occurrence, for $CsMn(HCOO)_3$, of a structural transformation from the hexagonal symmetry to an incommensurate modulated structure. This result, never accounted in literature, deserves further investigations for the solution of this new structural distortion stable at low temperature.

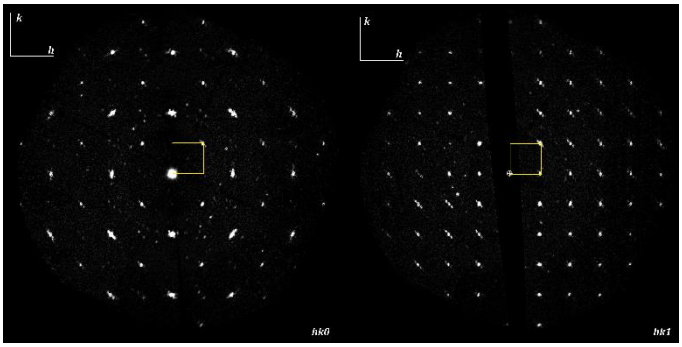

Figure 5.2-7: reciprocal space section of $CsMn(HCOO)_3$ obtained from electron diffraction measurements . The panel show the appearance of of hk0 (left) and hk1(right) direction for the crystal. The weak spots adjacent the main reflections are indicative of incommensurate modulation.

6 CONCLUSIONS AND FUTURE PERSPECTIVES

This thesis has been focused on the study of formate hybrid organic-inorganic materials, in particular on the ammonium and hydrazine formate-perovskites. During our studies we have been able to understand better the behaviour of these materials, both from the chemical and physical point of view.

For what concerns the ammonium compounds with general formula $[NH_4][M(HCOO)_3]$, we discovered a new method of synthesis based on the mechanochemical approach for M = Co^{2+}, Mn^{2+}, Zn^{2+}, Ni^{2+}, Cu^{2+}. This route of synthesis allows to obtain products with a high grade of crystallinity in a very simple way using as regents ammonium formate and the corresponding di-hydrated metal formates. We found a correlation between the milling time and the thermal stability of the di-hydrate metal formates suggesting that the first step of the synthesis is the dehydration of the metal formate salt. This new method to obtain the ammonium-formate compounds can be consider a new solvent-free strategy to obtain other formate-based compounds. The resulting materials have been characterized with different techniques and showed a very good grade of crystallinity, unusual in mechanochemical synthesis, and the physical properties are in agreement with the literature on samples synthesized by the conventional route.

The other family of formate compounds that has been studied in this work is the hydrazine-based formate with general formula $[NH_2NH_3][M(HCOO)_3]$ with M = Mn^{2+}, Fe^{2+}, Co^{2+}. This family of compounds has been largely studied in literature mainly for its interesting physical properties among which the prediction of ferroelectricity [39]. Unfortunately, not much is known about the chemical behaviour of these compounds and all the studies are performed on single crystals of the material. In this work we observed some interesting chemical behaviour by investigating these compound on powder samples and not on single crystals. This process required the adaptation and improvement of the already known synthesis to obtain suitable and pure powders of the samples. This point has been very challenging because of the different impurities that can form during the synthesis. In particular, we have noticed a very frequent tendency to the formation of $M(HCOO)_2 \times 2H_2O$ (M = Mn^{2+}, Fe^{2+}) when in the reaction mixture is present water coming from hydrated reagents or moisture; this impurity can be present in a non-negligible quantity and can significantly affect the whole synthesis, but by controlling these two factors, it is possible to reduce its presence.

Despite these impurities, it is known that these materials possess two polymorphs, the chiral and the perovskite one. In literature these two polymorphs are always treated separately both theoretically and experimentally.

Moreover, the studies performed in literature have been conducted only on the samples with zinc and magnesium, showing the stability of the two phases. In our work we experimentally found a correlation between these two polymorphs; in particular we found that for $[NH_2NH_3][Mn(HCOO)_3]$ and $[NH_2NH_3][Fe(HCOO)_3]$ the chiral polymorph is the first that is formed and then transforms into the perovskite one. We found that this transformation occurs both at the solid state and in solution and the rate of the transformation increases as the level of humidity increases. Moreover, we found a different rate of transformation depending on the metal, indicating that also the different crystal structures can promote the transformation differently. Thus, we suspect that the transition between the chiral and perovskite polymorphs is water-mediated and can occur through a dissolution/reprecipitation process in solution, instead at the solid state it may occur through reciprocal transformation of the neighbour crystal nuclei.

We also focused on the perovskite structure of $[NH_2NH_3][Mn(HCOO)_3]$ and, as this material presents a thermal induced transition when heated, we decided to follow it with PXRD to add more points to the ones already present in literature to identify the transition. The transformation maintains the perovskite architecture and changes it space group from $Pna2_1$ at low temperature to *Pnma* at high temperature. This is mainly due to the position of the hydrazinium cation that goes from ordered at low temperature to disordered over two position ad high temperature.

With the aim to synthesize new hydrazine-formate-based compounds, we tried to obtain samples that contain in the B site both Mn^{2+} and Fe^{2+} and, due to the instability of the chiral phase of $[NH_2NH_3][Mn(HCOO)_3]$, we tried to investigate if it was possible to stabilize it by mixing manganese with iron, since the chiral phase of $[NH_2NH_3][Fe(HCOO)_3]$ is more stable. First we have successfully obtained the perovskite phase of $[NH_2NH_3][Fe_{0.7}Mn_{0.3}(HCOO)_3$ and then, the chiral phase of $[NH_2NH_3][Fe_{0.6}Mn_{0.4}(HCOO)_3]$. Also in this case the chiral phase transform into the perovskite, and the whole transformation occurs in four days, a rate very close to the one of $[NH_2NH_3][Fe(HCOO)_3]$.

Since in literature ionic conduction is reported for various MOFs, we tried to investigate this property also in the formate-based compounds studied in this work. In particular we investigate the ionic conduction of $[NH_4][M(HCOO)_3]$ with M = Mn^{2+}, Co^{2+} and $[NH_2NH_3][M(HCOO)_3]$ with M = Mn^{2+} and Fe^{2+}.

For what concerns the ammonium-based compounds, the tested samples were synthesized *via* mechanosynthesis, to avoid the presence of the solvent that may interfere with the measurements.

Results show that conductivity is observed when the samples are in humid conditions and the activation of the process occur at RH = 37% for $[NH_4][Co(HCOO)_3]$ and 50% for $[NH_4][Mn(HCOO)_3]$. Values of ionic conductivity are in agreement with other known porous materials that exhibit ionic conduction and are in a range between 10^{-4} / 10^{-8} S cm^{-1}. It is interesting to note that these values are reached at a relatively low level of humidity, differently to the most known compounds. $[NH_4][Mn(HCOO)_3]$ reaches the maximum level of conductivity of 2.9 ± 0.3 x 10^{-4} S cm^{-1} at RH = 50% after two hour of exposure to the humid environment.

For what concerns the hydrazine-based materials, also in this case ionic conductivity is observed when the sample is exposed to humid ambient condition both for the chiral and perovskite polymorphs even though the conductivity reached for the chiral structure is higher. Reversibility tests on these samples showed the reversibility of the process. For what concerns the chiral structure the phase was stable till RH = 60%, instead for the perovskite till 30%. This confirms the higher stability of the perovskite phase compared to the chiral.

We propose that the observed ionic conduction is due to proton transfer with the water molecules present in the ambient. We suppose that the process is water-mediated though the ammine cation and, thanks to the well-formed H-bond network, the proton can travel through the structure. For the chiral polymorph this can occur in the channels of the structure, instead for the perovskite the proton can also migrate following other possible paths.

With the aim to synthesize new formate compounds, we have been able to successfully synthesize the $CsMn(HCOO)_3$ formate compound. To obtain this compound the liquid synthesis approach was performed for first, then we successfully applied the mechanochemical method for the first time. This compound has been important to confirm the ionic conduction behaviour of the ammonium and hydrazinium formate-based material discussed before; moreover, its characterization showed a low temperature transition that was not detected before. In particular we detected a transition from the DSC trace at 233 K on cooling and 303 K on heating, and PXRD analysis confirms a thermal structural distortion of the sample. The fitting of the low temperature data shows the presence of extra peaks not present at high temperature. $CsMn(HCOO)_3$ was, thus, analysed by electron diffraction (TEM) to further investigate the low temperature structure; the diffraction patterns are characterized by satellites, suggesting a modulated structure. Unfortunately, due to the damaging of the crystal under the electron beam, it has not been possible to determine the periodicity of that suspect modulation.

Future perspectives

Formate-based compounds have attached interest in the latest years due to their ferroelectric properties, experimentally proved as the case of the $[NH_4][M(HCOO)_3]$ family, or prediction as in the case of $[NH_2NH_3][M(HCOO)_3]$ compounds [61, 62, 39]. The measurements present in literature are performed only on single crystals of the material, but even though it is quite easy to obtain single crystals, for applications it would be interesting to investigate this behaviour on powders. This point might be challenging because of the different problems already found in this work, but it might open new routes to the application of these class of materials.

Future perspectives for the research regarding the mechanosynthesis of the ammonium-formate-based compounds might be to investigate other reaction conditions typical of the mechanochemistry, for example the energy employed and the number of spheres. Moreover, *in situ* PXRD and real time temperature detection might help to understand better the reaction mechanism. For what concerns the mechanosynthesis of the general formate compounds, it might be very interesting to add more compounds to the list of the one that is possible to synthesize with this approach. It would be especially useful for the compounds that require strong reaction conditions. Moreover, the solvent-free approach is more environment friendly.

For what concerns the hydrazine-based formate compounds, it would be interesting to investigate deeply the transformation between the chiral and perovskite phase, in particular with *in situ* analysis, for example Raman analysis or UV-Vis. Moreover, as the reorganization of the chiral framework that leads to the perovskite is not clear, it would be useful to understand in which way the chiral structure rearranges, and in which terms the different metals can influences the rate of transformation.

The proton conduction in the ammonium, and partially in the hydrazine compounds, needs a more detailed investigation. For example, in our experiments, has not been possible to estimate the activation energy of the process. Moreover, other hybrid compounds can be tested even if they do not present a clear channel structure, as suggested by the measurement performed in this work on the perovskite polymorph.

For what concerns the $CsMn(HCOO)_3$ compound, that showed a low temperature transition, will be very interesting to set single crystal analysis to confirm the presence of a modulated structure, which has not already been reported in literature.

7 EXPERIMENTAL METHODS

7.1 Synthesis of compounds

7.1.1 Liquid synthesis

7.1.1.1 Synthesis of hydrazine-formate compounds

To obtain the chiral polymorph of $[NH_2NH_3][Mn(HCOO)_3]$ and $[NH_2NH_3][Fe(HCOO)_3]$ 2 mmol of metal salt ($MnCl_2$ x $2H_2O$, $FeCl_2$) were dissolved in a becher with 15 mL of methanol. Separately, in a tube, 0.5 mL hydrazine (Sigma Aldrich, monohydrate, 98%) were mixed with 0.7 mL of HCOOH (Sigma Aldrich, >98%) in 10 mL of methanol. Successively, the first solution was gently added to the second and instantly it was possible to observe the precipitation of the compounds. The precipitate was pale pink/white for $[NH_2NH_3][Mn(HCOO)_3]$ instead for $[NH_2NH_3][Fe(HCOO)_3]$ it was light blue (Figure 6.1.1-1). To avoid the transformation in the perovskite phase, the products were quickly filtered and washed with methanol, then dried with N_2 flux.

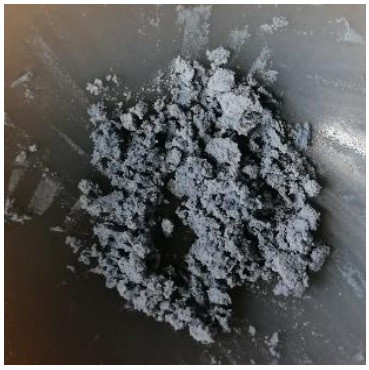

Figure 6.1.1-1: chiral phase of $[NH_2NH_3][Fe(HCOO)_3]$ immediately after the synthesis.

For the synthesis of the perovskite polymorph of $[NH_2NH_3][Fe(HCOO)_3]$ and $[NH_2NH_3][Mn(HCOO)_3]$, the procedure was the same used to obtain the corresponding chiral polymorph, but, in this case, the powders were left in the methanol solution or in air, so that the transition into the perovskite phase could occur. Generally, this process was faster for the compound with manganese and required from half an hour to one day, instead the iron sample required about three days.

The synthesis of chiral $[NH_2NH_3][Co(HCOO)_3]$ was performed following the same procedure, using $Co(NO_3)_2$ x $6H_2O$ as metal salt. In this case the product

was pink and, as the product is stable, could be easily collected and washed with methanol.

7.1.1.2 Synthesis of the ammonium-formate compounds

For the synthesis of $[NH_4][M(HCOO)_3]$ with M = Mn^{2+}, Fe^{2+} 2 mmol of the starting metal salt ($MnCl_2$ x $2H_2O$, $FeCl_2$) were dissolved in a becher with 10 ml of methanol. Separately in a glass tube, 2 mL of formic acid (Sigma Aldrich, >98%) and 2 mL of ammonia 33% were mixed, then the metal solution was gently added. Immediately it was possible to collect the precipitate that was filtered and washed with methanol.

7.1.2 Mechanosynthesis of $[NH_4][M(HCOO)_3]$ with M = Mn^{2+}, Co^{2+}, Ni^{2+}, Zn^{2+}, Cu^{2+}

Mechanosynthesis of $[NH_4][M(HCOO)_3]$ with M = Mn^{2+}, Co^{2+}, Ni^{2+}, Zn^{2+}, Cu^{2+} was performed by mixing the relative metal formate hydrate precursor with NH_4HCOO (Anhydrous, free-flowing, 97%, Sigma Aldrich) following the reaction:

$$NH_4HCOO + M(HCOO)_2 \text{ x } 2H_2O \rightarrow NH_4M(HCOO)_3 + 2H_2O$$

$$\text{with} \quad M=Mn^{2+}, Cu^{2+}, Co^{2+}, Zn^{2+}, Ni^{2+}$$

$Mn(HCOO)_2$ x XH_2O and $Cu(HCOO)_2$ x XH_2O were used as commercial products (Manganese(II) formate hydrate from Sigma Aldrich , Cu(II) formate hydrate from Sigma Aldrich 97%), instead the other metal formates were synthesized in laboratory (detailed are summarized at the end of this paragraph).

Before the milling session the metal formate powders were pre-treated at 353 K for a minimum of 45 min, then a stoichiometric amount of the reagents was grounded with a vertical vibration milling *(*FRITSCH Mini-Mill PULVERISETTE 23, steel jar) using one 10 mm steel ball. The mixing energy was maintained at 40 Hz for several steps of 5/10 minutes.

The hydrated formates for Co, Zn and Ni have been obtained following the general chemical reaction:

$$MCO_3 + 2HCOOH \rightarrow M(HCOO)_2 \text{ x} 2H_2O + H_2O + CO_2$$

$$\text{with M= } Co^{2+}, Ni^{2+} Zn^{2+}$$

$Co(HCOO)_2 \times 2H_2O$

200 mg of $CoCO_3$ are weighted in a flask with 5 mL di H_2O + 2 mL HCOOH (Sigma Aldrich, purity > 98%). Successively the flask is heated at 80°C in a water bath for 10 minutes, till the reaction is completed and then for two hours in ice. At the end it is possible to collect the violet product that is filtered, washed with ethanol, and dried first in air and then in the oven. From the evaporation of the water coming from the filtration it is possible to collect more product. Final yield = 85%.

$Zn(HCOO)_2 \times 2H_2O$

For the synthesis of $Zn(HCOO)_2$ x$2H_2O$, 800 mg of $ZnCO_3$ are mixed in a flask with 7 mL of water and 7 mL of HCOOH (sigma Aldrich, purity > 98%). The flask is heated in a water bath at 80°C till the reaction is completed (about 15 min) and then 2 mL of water are added. When the reaction is completed, the flask is cooled in ice for about 1 h at the end of which it is possible to collect a white precipitate. The solid is filtered with ethanol and dried first in air and then in oven. From the filtered water it is possible to collect more product. Total yield: 66%.

$Ni(HCOO)_2 \times 2H_2O$

200 mg of nickel carbonate are mixed with 10 mL of water and 2 mL of HCOOH (Sigma Aldrich, purity > 98%). The flask is heated in a water bath at 80°C till the reaction is completed and then cooled in ice for 2 hours. At the end it is possible to collect a green precipitate that is filtered with ethanol, dried first in air and then in oven. From the evaporation of the filtration water, it is possible to obtain more product. Final yield = 68%.

7.2 Ferroelectric tests

Due to the particular nature of the analysed materials, has not been possible to apply the usual procedure to perform ferroelectric test on powder samples. In fact, usually the pressed powders are metallized with gold with a process that require a high vacuumIn alternative the metallization can be made by the application of a silver paste which, however, must dry in air. In the case of the hybrid-formate compounds both ways can damage the sample due to the high vacuum or the too long exposure in air.

With the purpose to perform ferroelectric test on the powders of our samples, some of the polarization attempts were made using the silver paste trying to reduce the exposure time of the sample to air, whereas other samples were tested using a new device capable to avoid the classical metallization methods. In Figure 6.2.1 is shown the cell created to perform the measurements at room temperature.

The sample tablet is located in a Teflon ring and the metallization is made by the mechanical contact with two copper plates (7 mm), the lower is the one in which the tablet is leaning, the upper can be moved and positioned on the tablet. The two copper plates are connected with two wires to the ferroelectrometer.

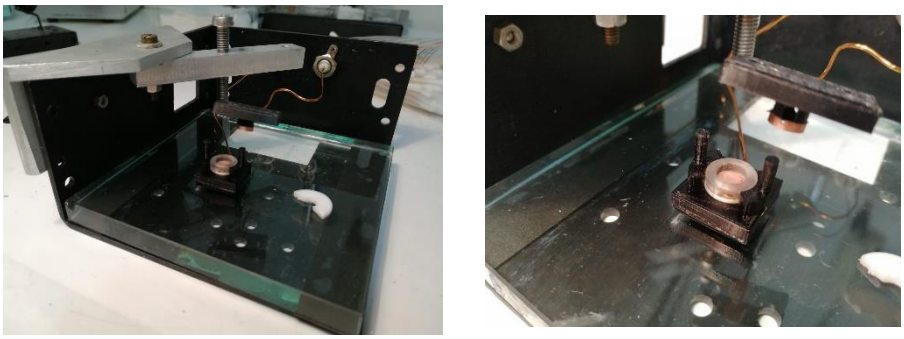

Figure 6.2-1: experiment set up for the ferroelectric measurements.

The attempts were performed using a TF analyzer 2000E ferroelectrometer.

7.3 Ionic conduction measurements

In this work to perform ionic conductivity measurements were performed using the Electrochemical Impedance Spectroscopy (ESI) technique This method is particularly effective to study ionic conduction phenomena and discriminate between electronic and ionic contribution to the total conductivity.

Generally, the resistance is a property of conductive materials and represents how easily the electron can flow along the material. The resistance can be expressed with the Ohm's law:

$$R = \frac{V}{I}$$

It follows that conductive material, for example metals, that possess many free charges show a low value of resistance, instead insulants, for example plastics, show high resistance values. In ionic conduction phenomena the current is due to the flow of ions instead of electrons and this behaviour merits a particular treatment.

Generally, in a conductive material, for example a metal, the recorded current is due to the flow of the electron through the material; this behaviour does not happen in ionic conductor material, in fact, the ions that are in the material cannot migrate; in fact when a continuous current is applied in presence of blocking

electrodes the ions are hindered in their movement. However, to allow the movements of the ion, it is possible to use an alternate potential difference by applying a sine wave potential:

$$V(t) = V_{max} \sin(wt)$$

with frequency $\nu = \frac{w}{2\pi}$. The application of an alternate current (ac) allows the movements of the ions in the material (Figure 6.3-1) [1].

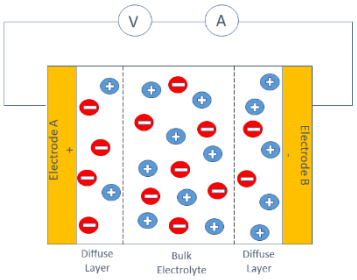

Figure 6.3-1: different diffuse regions of mobile ions with two inert and identical electrodes. The application of the A.C. current allows the movement of the charges and generates an accumulation on opposite charge electrode.

In this case the measured current will also have a sine form but due to the fact that ions do not move instantaneously, the new I expression contains a θ term:

$$I(t) = I_{max} \sin(wt + \theta)$$

that becomes

$$I(t) = \frac{V_0}{R} \sin(wt + \theta)$$

where θ is the phase difference between the applied potential and the measured current. Impedance measurements allows to obtain R and θ.

However, to treat the obtained data, is worth to consider that in general treating the system's response in the time domain is complex and requires the solution of a system of differential equations both for the capacitive $I(t) = \frac{dV(t)}{dt} C$ and inductive $V(t) = \frac{dI(t)}{dt} L$ responses (where C is the capacity and L the inductance). By applying the Fourier's transform to the previous equations, and changing domain from time to frequency, the Ohm's law become:

$$V = I \cdot Z$$

specific for alternate current. In this case R is replaced with Z, the impedance, that englobes both R and other effect due to the phase shift or simply other effect due to the ions' resistance. The impedance can be divided in two contributes:

$$Z_R = R \qquad \text{and} \qquad Z_c = -\frac{1}{C_i w}$$

where Z_c includes the capacitive effects due to the polarization delay of the charges on the electrode. C_i, which is defined as a complex number, is introduced as a parallelism with a capacitor since the charges on the plates have a similar behaviour. In particular, C_i summarized two different contributes due to: i) the capacity at the interfaces between the electrode and the material and ii) the capacity due to the electrodes.

It is interesting to note that Z_c is an ideal contribute assuming an electrical isolation and no exchange of electrons or ions. Nevertheless, some electrons can flow by tunnel effect, so Z_c is corrected as follow:

$$Z_{CPE} = -\frac{1}{C(i\Omega)^{\Psi}}$$

where CPE means "constant phase element" and $0<\Psi<1$. So, if $\Psi \sim 0$ $Z_R = R$ [1].

Graphical representation

The expression of the impedance as sum of a real and imaginary part can also facilitate the graphical representation; in particular in this work has been used the Nyquist representation, or Cole-Cole or Argand plot. In this representation the imaginary part of the impedance ($-I_m(Z)$) is reported on the ordinate axes, instead the real part ($Re(Z)$) on the abscissa. In this way, the imaginary part refers to Z_c and the real one to R allowing to easily understand the behaviour of the system by the shape of the Nyquist plot.

The extrapolation of the electrical transport properties of a material is quite hard when done directly from the response to an alternate potential, but the modelling of this behaviour with an equivalent circuit can make it easier. The equivalent circuit is made of basic elements taken from the macroscopic circuits, for example capacitors and resistors; in this way the capacitors can model process like local polarizabilities, instead resistors represent conductivities of different natures [1]. As we are interested in obtaining the ionic conduction of solid electrolytes, this model has to be created on purpose as the experimental setting is made. Our system consists of a solid electrolyte between two blocking (impermeable to the ions of the ionic conductor) and stainless-steel electrodes. This model can be represented with

the equivalent circuit illustrated in Figure 6.3-2, in which the resistance R_i represents the ions crossing the electrolytes and R_e represents the electronic resistance of the experimental system, like the way the contact are made, the cables or the instrumentation. For what concerns the interface between a solid electrolyte and a purely electronic conductor, it has been demonstrated [2], both experimentally and theoretically, that this behaviour can be modelled as a simple series of capacitors (C_{int}) and a ionic resistance (R_i); this is possible because it consists of accumulation of ions at the metal/electrolyte interface. In this non-ideal case, C_{int} is represented by the constant phase element (CPE). To this model need to be added a geometry capacitor, and, as the system consist of two metal electrodes separated by a dielectric, it behaves like a parallel plates capacitor. This contribution is generally small, but not negligible, and it is modelled introducing a C_{geom} capacity parallel to the series of resistance and capacitor.

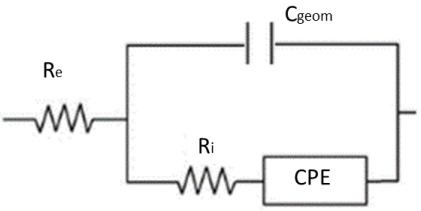

Figure 6.3-2: Debye equivalent circuit used to model the ionic conduction behaviour in this work. R_e represents the resistance of the contacts, C_{geom} the geometry capacitor, R_i the ionic resistance and CPE the constant phase element.

As mentioned before, the plot of imaginary part of the impedance, -Im(Z) vs real part of the impedance, Re(Z), collected at different frequencies is called the Nyquist plot and it is represented in Figure 6.3-3. At low frequencies (low Re(Z) values) the impedance of the capacitors (C_{geom}, C_{int}) is high, and the flowing of the current is more difficult. As the frequency increases, C_{geom} is predominant on Cint and consequently the current start to flow along Ri and Cint. This process can be seen in the Nyquist plot as the vertical straight line typical of the ionic conductors called "tail". At high frequency C_{int} decreases and after a frequency threshold the capacitor behaves like a closed circuit, so that, the imaginary part of the impedance is zero and, due to the resistance, all the impedance belongs to the real part. C_{geom} decreases at high frequency and when its value is equal to the resistance, the current is equally divided between the two branches of the circuit; this process is reached at the maximum point of the semicircle in the Nyquist plot [3].

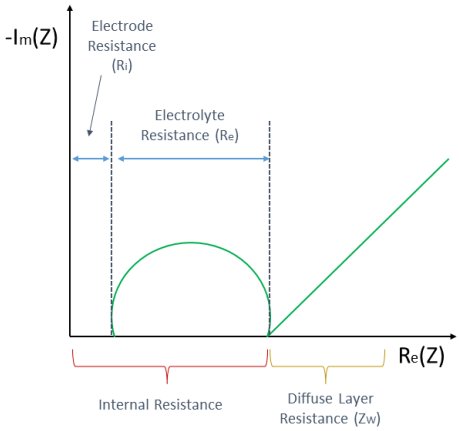

Figure 6.3-3: ideal representation of the Nyquist plot obtained by impedance spectroscopy measurements.

In simpler words, the semi-circular region corresponds to the resistance of the bulk electrolyte, instead the linear part of the impedance (that is ideally at 45° with respect the real axis) is related to the diffusion phenomena typical of charge carrier conduction. When the linear part of the Nyquist plot is at 45°, the region is known as the *Warburg impedanc*e, and represents the diffusion effect that is active at lower frequencies of the potential perturbation. At high frequencies, the Warburg impedance is small because diffusing reactants don't have time to move very far. On the contrary at high frequencies the fast processes (electrolytic side of conduction phenomena) are responsible of the impedance values describing the semi-circular curve.

It is interesting to note that the name of the technique "Impedance spectroscopy" just comes because of the variation of the frequency during the experiments, even though frequency is not present in the plot, and, because of this, it is classified as a spectroscopy technique.

Experimental procedures

Pellets of the samples were used to perform ionic conduction measurements. In particular the powders were pressed (max 2 tons) and pellets of 7 mm of diameter were used for the measurements. Electrochemical impedance spectroscopy (EIS measurements were performed with a HP 4192A impedance analyser in the frequency range 5 Hz-13 MHz, by applying a sine wave with amplitude of 0.1 V).

7.4 Synchroton diffraction

In this work synchrotron radiation has been used to analyse the samples; in particular the experiments were performed at the Elettra synchrotron in Trieste. Synchrotron radiation is a powerful analysis technique and possess several advantages compared to conventional X-rays sources. It has a very high intensity, and, due to the fact that the beams are accurately parallel, the data possess high resolution and has many applications in different fields.

The generation of the synchrotron radiation (Figure 6.4-1) starts in the booster, which shoots electrons and accelerates them at extremely high energy. An electron source is located in the first part of the booster, here charged particles are emitted by a metal electrode; the electrons are guided inside a thin circular high vacuum steel tube of a 1200 m conference through intense magnetic fields. They are then accelerated to 2.5 x 10^{12} eV. The electrons are shot from the booster into the transfer line and finally injected into the storage ring long 260 m. Here they will circle for 24 h without interruption almost at the speed of light and their energy will remain constant.

Synchrotron light is generated in the storage ring, in fact the ring is an alternation of straight and curved sections and in each curved section a powerful magnet guides the electrons forcing them to deviate from their path; each time they deviate the electrons emit energy in the form of light. The beams of lights tangent to the storage ring are conveyed into the beam lines where the experiments are performed.

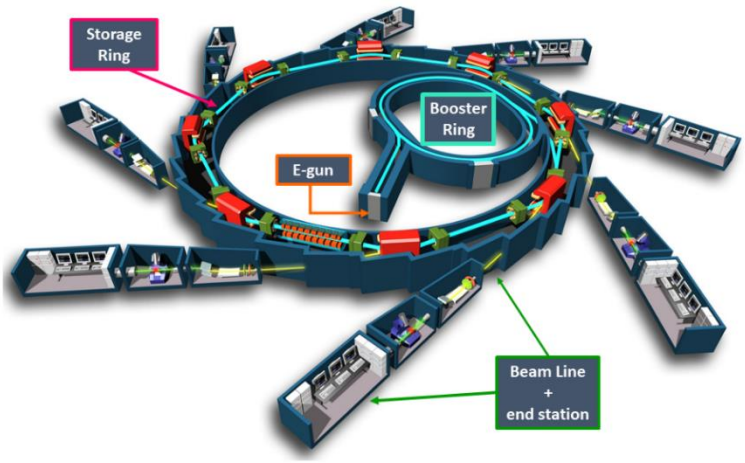

Figure 6.4-1: schematic representation of synchrotron. (Image taken fromEPSIM 3D/JF Santarelli, Synchrotron Soleil.

Today Elettra has 23 operating beams lines each specialized for a different type of measurements; this allows to perform experiments in the various fields from chemistry to biology, electronics, environmental sciences, materials engineering, medicine, nanotechnology, and archaeology. The experiments presented in this work were performed at the MCX beam line, which allows to perform a wide range of non-single crystal diffraction experiments: grazing angle diffraction and reflectivity, residual stress and texture analysis, phase identification, structural studies and kinetic studies.

Beam line description

In order to fulfil the required flexibility in terms of beam characteristics, ranging from spot focus to line focus and to parallel beam, the optics of the beamline consist of two mirrors and one monochromator: a first Pt-coated cylindrical mirror collimates the beam on the horizontally focusing Si (111) double crystal monochomator in 1:1 configuration. The second - vertical focusing - platinum coated mirror is flat and bendable, with a radius adjustable from 6 km to flat [136].

The double crystal monochromator (DCM) consists of two Si crystals (active area 50×50 mm^2), cut along the [111] direction, which can be precisely positioned and oriented in the X-ray beam.

Experimental procedures

The samples were synthesized at Electra following the previous described procedures. Immediately after the synthesis the sample was placed in the capillary (0.5 mm diameter) and then the data were collectedwith $\lambda = 1.0332$. Rietveld and Le Bail refinements were performed with the help of the Jana2006 software [137].

7.5 *Laborato*ry powder x-ray diffraction (PXRD)

PXRD measurement were performed using a Thermo X'TRA diffractometer working with a Cu K_α radiation and equipped with a Si(Li) solid state detector suited to suppress the Cu K_β radiation.

The high resolution x-ray diffraction measurements were performed with a STOE Stadi P (equipped with Mo-$K_{\alpha1}$ source, Ge111 monochromator produced by STOE & CIE, detector MYTHEN2 1 K produced by Dectris). The powders were placed in a capillary of 0.3 mm of diameter to avoid preferred orientations. Rietveld and Le Bail refinements were performed with the help of the Jana2006 software [137].

7.6 Raman spectroscopy measurements

Raman measurements were performed few hours after the mechanosynthesis of the samples. The measurements were performed using a Horiba LabRAM HR Evolution confocal spectrometer (focal 800 mm), using a configuration with a holographic grating (1800 lines/mm), a set of Bragg ultra-low frequency filters for the rejection of the Rayleigh scattering and a liquid nitrogen cooled CCD detector. The system is equipped with four different lasers (532, 632.8, 785 and 1064 nm): the 632.8 nm line of a He–Ne laser was used for excitation. Neutral density filters were used to keep the laser power on the sample under 1 mW. An Ultra-Long Workind Distance (ULWD) 50X objective was used for excitation and signal collection. The spectrometer is equipped with XYZ motorized stage and autofocus. The autocalibration procedure was performed before each measurement session. Spatial resolution was about 2 µm, and the spectral resolution was 0.5 cm^{-1}. The investigated spectral range was from 10 to 4000 cm^{-1}. Typical collection time of the spectra ranged from 30 to 60 s for each acquisition, with 2 repetitions.

7.7 Thermal analysis

Thermal analyses were performed using a Perkin Elmer DSC 6000 and TGA 8000 instruments. For the sample obtained with the mechanochemical approach, TGA measurements were performed under N_2 atmosphere from 298 to 700 K with a rate of 10 K/min. The DSC measurement performed on the perovskite phase of $[NH_2NH_3][Mn(HCOO)_3]$ sample was performed from 216 to 413 K with a rate of 10 K/min.

7.8 Scanning electron micrographs (SEM) analysis

SEM analyses were performed by FieldEmission Gun Scanning Electron Microscope (Zeiss Auriga FEG-SEM), equipped with an In-Lens detector, at 10 kV accelerating voltage. Samples analysed in SEM were previously coated with a thin 2–3 nm Au layer by means of a low-energy sputtering system (Edwards Scancoat Six), in order to remove electrostatic charge accumulation on the surface during electron-beam illumination.

7.9 Supplementary information

Table 7.9-1: Atomic coordination for $[NH_4][Cu(HCOO)_3]$.

Atom	**x**	**y**	**z**	**U_{iso}**
C1	0.4779	0.2903	0.4911	0.044496
C2	0.0134	0.2753	0.9916	0.034284
C3	0.3299	0.0116	0.5182	0.042754
Cu1	0.2446	0.1679	0.7621	0.025114
H1	0.5402	0.2274	0.498	0.053
H2	-0.0471	0.2118	0.9962	0.041
H3	0.203	0.0131	0.4966	0.4966
H11	0.277	0.4612	0.6724	0.066
H12	0.22	0.4503	0.8431	0.066
H13	0.3518	0.5308	0.796	0.066
H14	0.1578	0.5385	0.747	0.066
N1	0.2519	0.4954	0.7658	0.055286
O1	0.3613	0.3079	0.598	0.04676
O2	0.5211	0.3478	0.3746	0.034468
O3	0.142	0.285	0.89	0.031111
O4	-0.0396	0.3439	1.0867	0.034957
O5	0.3858	0.0669	0.6327	0.036732
O6	0.4242	-0.0447	0.4307	0.042188

Table 7.9-2: Atomic coordination for $[NH_4][Co(HCOO)_3]$.

Atom	**x**	**y**	**z**	**U_{iso}**
Co1	0.3333	0.6667	0.25	0.0187(4)
O1	0.3067(3)	0.8891(3)	0.1066(3)	0.0242(14)
C	0.4356(6)	1	0	0.040(3)
H1c	0.567	1	0	0.048405
N	0	0	0.25	0.054(3)
H1n	0.1206(10)	0.003(2)	0.1886(3)	0.065089
H2n	0	0	0.3722(6);	0.065089

Table 7.9-3: Atomic coordination for $[NH_4][Zn(HCOO)_3]$.

Atom	**x**	**y**	**z**	**U_{iso}**
Ni1	0.3333	0.6667	0.25	0.0216(3)
O1	0.3055(4);	0.8874(3)	0.1070(3)	0.0270(16)
C	0.4341(6)	1	0	0.036(4)
H1c	0.5652	1	0	0.043775
N	0	0	0.25	0.066(4)
H1n	0.098(8)	-0.036(11)	0.1881(5)	0.079212
H2n	0	0	0.3725(10)	0.079212

Table 7.9-4: Atomic coordination for $[NH_4][Ni(HCOO)_3]$.

Atom	**x**	**y**	**z**	**U_{iso}**
Ni1	0.3333	0.6667	0.25	0.0131(3)
O1	0.3093(3)	0.8880(3)	0.1068(2)	0.0191(11)
C	0.4400(5)	1	0	0.029(2)
H1c	0.572	1	0	0.034627
N	0	0	0.25	0.052(3)
H1n	0.093(7)	-0.045(9)	0.1867(5)	0.06231
H2n	0;	0	0.3738(10);	0.06231

Table 7.9-5: Atomic coordination for perovskites polymorph of $[NH_2NH_3][Co(HCOO)_3]$.

Atom	**x**	**y**	**z**	**U_{iso}**
Co1	0.2586	0.2754	0.6655	0.017148
N1	0.2681	0.7052	0.4736	0.124093
H4	0.2103	0.7019	0.4116	0.148912
H5	0.3868;	0.7547	0.4675	0.148912
H6	0.2795	0.5929	0.4983	0.148912
N2	0.1683	0.7965	0.5336	0.088536
H1n2	0.106	0.7302	0.571	0.106243
H2n2	0.2392	0.8597	0.5684	0.106243
O1	0.4235	0.5504	0.3167	0.014763
O2	0.6162	0.3729	0.3831	0.019924
C1	0.5462	0.4418	0.3111	0.030785
H1c1	0.5888	0.4097	0.2483	0.036942

Table 7.9-6: Atomic coordination for $CsMn(HCOO)_3$ at 298.15 K.

Atom	**x**	**y**	**z**	**U_{iso}**
Cs1	0	0	0.25	0.0238(3)
Mn1	0.6667	0.3333	0.25	0.0067(5)
O	0.6922(5)	0.5809(5)	0.1026(4)	0.023(2)
C	0.5669(11)	0.5669(11)	0	0.025(5)
H1c	0.4405	0.4405	0	0.029937

Table 7.9-7: Atomic coordination for $CsMn(HCOO)_3$ at 213.15 K.

Atom	**x**	**y**	**z**	**U_{iso}**
Cs1	0	0	0.25	0.0056(3)
Mn1	0.6667	0.3333	0.25	-0.0067(5)
O	0.6934(5)	0.5821(5)	0.1028(4)	0.0030(14)
C	0.5643(11)	0.5643(11)	0	0.016(3)
H1c	0.4377	0.4377;	0	0.019528

8 BIBLIOGRAPHY

1. Wenk, H.-R. & B. Minerals. Their Constitution and Origin. *Cambridge Univerisy Press* (2004) doi:10.1017/s0016756805210774.
2. Ruyan, A. S. B. & Rustum, G. Plugin-Fulltext-2. 3–26 (2000).
3. Assirey, E. A. R. Perovskite synthesis, properties and their related biochemical and industrial application. *Saudi Pharm. J.* **27**, 817–829 (2019).
4. Von Hippel, A. Ferroelectricity, domain structure, and phase transitions of barium titanate. *Rev. Mod. Phys.* **22**, 221–237 (1950).
5. Mabud, S. A. & Glazer, A. M. Lattice parameters and birefringence in PbTiO 3 single crystals . *J. Appl. Crystallogr.* **12**, 49–53 (1979).
6. Kubel, F. & Schmid, H. Structure of a ferroelectric and ferroelastic monodomain crystal of the perovskite BiFeO3. *Acta Crystallogr. Sect. B* **46**, 698–702 (1990).
7. Li, W. *et al.* Chemically diverse and multifunctional hybrid organic-inorganic perovskites. *Nat. Rev. Mater.* **2**, (2017).
8. Weller, M. T., Weber, O. J., Henry, P. F., Di Pumpo, A. M. & Hansen, T. C. Complete structure and cation orientation in the perovskite photovoltaic methylammonium lead iodide between 100 and 352 K. *Chem. Commun.* **51**, 4180–4183 (2015).
9. Wang, Z. *et al.* Anionic NaCl-type frameworks of [Mn. 2209–2216 (2004).
10. Tong, M. L. *et al.* Cation-templated construction of three-dimensional α-Po cubic-type [M(dca)3]- networks. Syntheses, structures and magnetic properties of A[M(dca)3] (dca = dicyanamide; for A = benzyltributylammonium, M = Mn2+, Co2+; for A = benzyltriethylammonium, M = Mn2. *New J. Chem.* **27**, 779–782 (2003).
11. Golschmidt. . *Naturwissenschaften* vol. 21 (1926).
12. Kieslich, G., Sun, S. & Cheetham, A. K. Solid-state principles applied to organic–inorganic perovskites: New tricks for an old dog. *Chem. Sci.* **5**, 4712–4715 (2014).
13. Wei, F. *et al.* The synthesis, structure and electronic properties of a lead-free hybrid inorganic-organic double perovskite (MA)2KBiCl6 (MA = methylammonium). *Mater. Horizons* **3**, 328–332 (2016).

14. Wang, Z. *et al.* Synthesis and characterization of a porous magnetic diamond framework, Co3(HCOO)6, and its N2 sorption characteristic. *Inorg. Chem.* **44**, 1230–1237 (2005).

15. Wang, Z., Hu, K., Gao, S. & Kobayashi, H. Formate-based magnetic metal-organic frameworks templated by protonated amines. *Adv. Mater.* **22**, 1526–1533 (2010).

16. Eikeland, E. *et al.* Alkali Metal Ion Templated Transition Metal Formate Framework Materials: Synthesis, Crystal Structures, Ion Migration, and Magnetism. *Inorg. Chem.* **53**, 10178–10188 (2014).

17. Duan, Z., Wang, Z. & Gao, S. Irreversible transformation of chiral to achiral polymorph of K[Co(HCOO)3]: synthesis, structures, and magnetic properties. *Dalt. Trans.* **40**, 4465–4473 (2011).

18. Bovill, S. M. & Saines, P. J. Structure and magnetic properties of the AB(HCO2)3 (A = Rb+ or Cs+, B = Mn2+, Co2+ or Ni2+) frameworks: Probing the effect of size on the phase evolution of the ternary formates. *CrystEngComm* **17**, 8319–8326 (2015).

19. Collings, I. E. *et al.* Compositional dependence of anomalous thermal expansion in perovskite-like ABX3 formates. *Dalt. Trans.* **45**, 4169–4178 (2016).

20. Shang, R., Sun, X., Wang, Z. M. & Gao, S. Zinc-diluted magnetic metal formate perovskites: Synthesis, structures, and magnetism of [CH 3NH 3][Mn xZn 1-x(HCOO) 3] (x=0-1). *Chem. - An Asian J.* **7**, 1697–1707 (2012).

21. Canadillas-Delgado, L., Mazzuca, L., Fabelo, O., Rodriguez-Velamazan, J. A. & Rodriguez-Carvajal, J. Incommensurate structures of the [CH3NH3][Co(COOH)3] compound. *IUCrJ* **6**, 105–115 (2019).

22. Shang, R., Chen, S., Wang, B.-W., Wang, Z.-M. & Gao, S. Temperature-Induced Irreversible Phase Transition From Perovskite to Diamond But Pressure-Driven Back-Transition in an Ammonium Copper Formate. *Angew. Chemie* **128**, 2137–2140 (2016).

23. Shang, R., Xu, G. C., Wang, Z. M. & Gao, S. Phase transitions, prominent dielectric anomalies, and negative thermal expansion in three high thermally stable ammonium magnesium-formate frameworks. *Chem. - A Eur. J.* **20**, 1146–1158 (2014).

24. Mączka, M. *et al.* Perovskite metal formate framework of [NH2-CH +-NH2]Mn(HCOO)3]: Phase transition, magnetic, dielectric, and phonon properties. *Inorg. Chem.* **53**, 5260–5268 (2014).

25. Rossin, A., Chierotti, M. R., Giambastiani, G., Gobetto, R. & Peruzzini, M. Amine-templated polymeric Mg formates: Crystalline scaffolds exhibiting extensive hydrogen bonding. *CrystEngComm* **14**, 4454–4460 (2012).

26. Luo, C. *et al.* Synthesis, Structure and Properties of Formamidine-templated Metal Formate Crystals. *Cryst. Res. Technol.* **52**, 1–6 (2017).

27. Mączka, M. *et al.* Phase Transitions and Coexistence of Magnetic and Electric Orders in the Methylhydrazinium Metal Formate Frameworks. *Chem. Mater.* **29**, 2264–2275 (2017).

28. Mączka, M. *et al.* Synthesis and characterization of [(CH3)2NH2][Na0.5Cr0.5(HCOO)3]: A rare example of luminescent metal-organic frameworks based on Cr(iii) ions. *Dalt. Trans.* **44**, 6871–6879 (2015).

29. Ciupa, A., Mączka, M., Gągor, A., Pikul, A. & Ptak, M. Synthesis and characterization of novel niccolites [(CH3)2NH2][FeIIIMII(HCOO)6] (MII = Zn, Ni, Cu)†. *Dalt. Trans.* **44**, 13234–13241 (2015).

30. Jain, P. *et al.* Multiferroic Behavior Associated with an Order - Disorder Hydrogen Bonding Transition in Metal - Organic Frameworks (MOFs) with the Perovskite ABX 3 Architecture. *J. AM. CHEM. So* **131**, 13625–13627 (2009).

31. Hu, K. L., Kurmoo, M., Wang, Z. & Gao, S. Metal-organic perovskites: Synthesis, structures, and magnetic properties of [C(NH2)3][MII(HCOO)3] (M=Mn, Fe, Co, Ni, Cu, and Zn; C(NH2)3=guanidinium). *Chem. - A Eur. J.* **15**, 12050–12064 (2009).

32. Imai, Y., Zhou, B., ito, Y. et al. Perovskite Compound. *Chem. Asian* **7**, 2786 (2012).

33. Asaji, T. *et al.* Phase transition and ring-puckering motion in a metal-organic perovskite [(CH2)3NH2][Zn(HCOO)3]. *J. Phys. Chem. A* **116**, 12422–12428 (2012).

34. Pato-Doldán, B. *et al.* Coexistence of magnetic and electrical order in the new perovskite-like (C3N2H5)[Mn(HCOO)3] formate. *RSC Adv.* **3**, 22404–22411 (2013).

35. Mączka, M. *et al.* Structural, thermal, dielectric and phonon properties of perovskite-like imidazolium magnesium formate. *Phys. Chem. Chem. Phys.* **18**, 13993–14000 (2016).

36. Chen, S., Shang, R., Wang, B. W., Wang, Z. M. & Gao, S. An A-Site Mixed-Ammonium Solid Solution Perovskite Series of

[(NH2NH3)x(CH3NH3)1−x][Mn(HCOO)3] (x=1.00–0.67). *Angew. Chemie - Int. Ed.* **54**, 11093–11096 (2015).

37. Kieslich, G. *et al.* Tuneable mechanical and dynamical properties in the ferroelectric perovskite solid solution [NH3NH2]1-x[NH3OH]xZn(HCOO)3. *Chem. Sci.* **7**, 5108–5112 (2016).

38. Liu, J. Q. *et al.* Temperature identification on two 3D Mn(ii) metal-organic frameworks: Syntheses, adsorption and magnetism. *RSC Adv.* **4**, 20605–20611 (2014).

39. Chen, S., Shang, R., Hu, K. L., Wang, Z. M. & Gao, S. [NH2NH3][M(HCOO)3] (M = Mn2+, Zn2+, Co2+ and Mg2+): structural phase transitions, prominent dielectric anomalies and negative thermal expansion, and magnetic ordering. *Inorg. Chem. Front.* **1**, 83–98 (2014).

40. Boström, H. L. B., Hill, J. A. & Goodwin, A. L. Columnar shifts as symmetry-breaking degrees of freedom in molecular perovskites. *Phys. Chem. Chem. Phys.* **18**, 31881–31894 (2016).

41. Hill, J. A., Thompson, A. L. & Goodwin, A. L. Dicyanometallates as Model Extended Frameworks. *J. Am. Chem. Soc.* **138**, 5886–5896 (2016).

42. Duyker, S. G., Hill, J. A., Howard, C. J. & Goodwin, A. L. Guest-Activated Forbidden Tilts in a Molecular Perovskite Analogue. *J. Am. Chem. Soc.* **138**, 11121–11123 (2016).

43. Zhang, W., Cai, Y., Xiong, R. G., Yoshikawa, H. & Awaga, K. Exceptional dielectric phase transitions in a perovskite-type cage compound. *Angew. Chemie - Int. Ed.* **49**, 6608–6610 (2010).

44. Evans, N. L. *et al.* Control of Multipolar and Orbital Order in Perovskite-like [C(NH2)3]CuxCd1-x(HCOO)3 Metal-Organic Frameworks. *J. Am. Chem. Soc.* **138**, 9393–9396 (2016).

45. Goodwin, A. L. Rigid unit modes and intrinsic flexibility in linearly bridged framework structures. *Phys. Rev. B - Condens. Matter Mater. Phys.* **74**, 1–10 (2006).

46. Hammonds, K. D., Dove, M. T., Giddy, A. P., Heine, V. & Winkler, B. Rigid-unit phonon modes and structural phase transitions in framework silicates. *Am. Mineral.* **81**, 1057–1079 (1996).

47. Dove, M. T., Heine, V. & Hammonds, K. D. Rigid unit modes in framework silicates. *Mineral. Mag.* **59**, 629–639 (1995).

48. Boström, H. L. B., Senn, M. S. & Goodwin, A. L. Recipes for improper

ferroelectricity in molecular perovskites. *Nat. Commun.* **9**, 1–7 (2018).

49. Jain, P., Dalal, N. S., Toby, B. H., Kroto, H. W. & Cheetham, A. K. Order - Disorder Antiferroelectric Phase Transition in a Hybrid Inorganic - Organic Framework with the Perovskite Architecture. *J. AM. CHEM. So* **130**, 10450–10451 (2008).

50. Xu, W. J., Du, Z. Y., Zhang, W. X. & Chen, X. M. Structural phase transitions in perovskite compounds based on diatomic or multiatomic bridges. *CrystEngComm* **18**, 7915–7928 (2016).

51. Moriya, T. Anisotropic superexchange interaction and weak ferromagnetism. *Phys. Rev.* **120**, 91–98 (1960).

52. Zhou, B., Imai, Y., Kobayashi, A., Wang, Z.-M. & Kobayashi, H. Giant Dielectric Anomaly of a Metal-Organic Perovskite with Four-Membered Ring Ammonium Cations. *Angew. Chemie* **123**, 11643–11647 (2011).

53. Śanchez-Andújar, M. *et al.* Characterization of the order-disorder dielectric transition in the hybrid organic-inorganic perovskite-like formate Mn(HCOO)3[(CH 3)2NH2]. *Inorg. Chem.* **49**, 1510–1516 (2010).

54. Fu, D. W. *et al.* A multiferroic perdeutero metal-organic framework. *Angew. Chemie - Int. Ed.* **50**, 11947–11951 (2011).

55. Stroppa, A. *et al.* Electric control of magnetization and interplay between orbital ordering and ferroelectricity in a multiferroic metal-organic framework. *Angew. Chemie - Int. Ed.* **50**, 5847–5850 (2011).

56. Stroppa, A., Barone, P., Jain, P., Perez-Mato, J. M. & Picozzi, S. Hybrid improper ferroelectricity in a multiferroic and magnetoelectric metal-organic framework. *Adv. Mater.* **25**, 2284–2290 (2013).

57. Di Sante, D., Stroppa, A., Jain, P. & Picozzi, S. Tuning the ferroelectric polarization in a multiferroic metal-organic framework. *J. Am. Chem. Soc.* **135**, 18126–18130 (2013).

58. Ghosh, S., Di Sante, D. & Stroppa, A. Strain Tuning of Ferroelectric Polarization in Hybrid Organic Inorganic Perovskite Compounds. *J. Phys. Chem. Lett.* **6**, 4553–4559 (2015).

59. Pato-Doldán, B. *et al.* Near room temperature dielectric transition in the perovskite formate framework [(CH3)2NH2][Mg(HCOO)3]. *Phys. Chem. Chem. Phys.* **14**, 8498–8501 (2012).

60. Mączka, M. *et al.* Effect of solvent, temperature and pressure on the stability of chiral and perovskite metal formate frameworks of [NH 2 NH 3

][M(HCOO) 3] (M = Mn, Fe, Zn) . *Phys. Chem. Chem. Phys.* **18**, 31653–31663 (2016).

61. Xu, G. C., Ma, X. M., Zhang, L., Wang, Z. M. & Gao, S. Disorder-order ferroelectric transition in the metal formate framework of [NH4][Zn(HCOO)3]. *J. Am. Chem. Soc.* **132**, 9588–9590 (2010).

62. Xu, G. *et al.* Coexistence of Magnetic and Electric Orderings in the MetalÀFormate. *J. Am. Chem. Soc.* **133**, 14948–14951 (2011).

63. Mączka, M., Szymborska-Małek, K., Ciupa, A. & Hanuza, J. Comparative studies of vibrational properties and phase transitions in metal-organic frameworks of [NH4][M(HCOO)3] with M = Mg, Zn, Ni, Fe, Mn. *Vib. Spectrosc.* **77**, 17–24 (2015).

64. Lawler, J. M. M., Manuel, P., Thompson, A. L. & Saines, P. J. Probing ferroic transitions in a multiferroic framework family: a neutron diffraction study of the ammonium transition metal formates. *Dalt. Trans.* **44**, 11613–11620 (2015).

65. Tanaka, S., Nagaoka, T., Yasuyoshi, A., Hasegawa, Y. & Denayer, J. F. M. Hierarchical Pore Development of ZIF-8 MOF by Simple Salt-Assisted Mechanosynthesis. *Cryst. Growth Des.* **18**, 274–279 (2018).

66. Park, K. S. *et al.* Exceptional chemical and thermal stability of zeolitic imidazolate frameworks. *Proc. Natl. Acad. Sci.* **103**, 10186–10191 (2006).

67. Prochowicz, D. *et al.* Mechanosynthesis of the hybrid perovskite CH3NH3PbI3: Characterization and the corresponding solar cell efficiency. *J. Mater. Chem. A* **3**, 20772–20777 (2015).

68. Maczka, M. *et al.* Temperature-and pressure-induced phase transitions in the metal formate framework of [ND4][Zn(DCOO)3] and [NH4][Zn(HCOO)3]. *Inorg. Chem.* **53**, 9615–9624 (2014).

69. Wang, Z. *et al.* Occurrence of a rare 49·66 structural topology, chirality, and weak ferromagnetism in the [NH4][M II(HCOO)3] (M = Mn, Co, Ni) frameworks. *Inorg. Chem.* **46**, 437–445 (2007).

70. Peksa, P., Zare, J. K., Pawlus, S. & Sieradzki, A. Revisiting a Perovskite-like Copper-Formate Framework NH 4 [Cu(HCOO) 3]: Order − Disorder Transition In fl uenced by Jahn- Teller Distortion and above Room-Temperature Switching of the Nonlinear Optical Response between Two SHG-Active States. 2–11 (2020) doi:10.1021/acs.jpcc.0c06141.

71. Shevchenko, V. G., Krasil'nikov, V. N., Yeselevich, D. A. & Konyukova, A. V. Oxidation of Powdered Aluminum after Surface Modification with Mn,

Fe, Co, and Ni Formates. *Prot. Met. Phys. Chem. Surfaces* **55**, 21–27 (2019).

72. K. Ravaglia, V. Vit, L. R. Sintesi e caratterizzazione di perovskiti ibride organiche-inorganiche. *Master Thesis* (2020).

73. Takacs, L. The historical development of mechanochemistry. *Chem. Soc. Rev.* **42**, 7649–7659 (2013).

74. Patil, A. O., Curtin, D. Y. & Paul, I. C. Solid-State Formation of Quinhydrones from Their Components. Use of Solid-Solid Reactions To Prepare Compounds Not Accessible from Solution. *J. Am. Chem. Soc.* **106**, 348–353 (1984).

75. Caira, M. R., Nassimbeni, L. R. & Wildervanck, A. F. Selective formation of hydrogen bonded cocrystals between a sulfonamide and aromatic carboxylic acids in the solid state. *J. Chem. Soc. Perkin Trans. 2* 2213–2216 (1995) doi:10.1039/p29950002213.

76. Etter, M. C., Zia-Ebrahimi, M., Urbañczyk-Lipkowska, Z. & Panunto, T. W. Hydrogen Bond Directed Cocrystallization and Molecular Recognition Properties of Diarylureas. *J. Am. Chem. Soc.* **112**, 8415–8426 (1990).

77. Garay, A. L., Pichon, A. & James, S. L. Solvent-free synthesis of metal complexes. *Chem. Soc. Rev.* **36**, 846–855 (2007).

78. Friščič, T. & Jones, W. Recent advances in understanding the mechanism of cocrystal formation via grinding. *Cryst. Growth Des.* **9**, 1621–1637 (2009).

79. Friić, T. & Fábián, L. Mechanochemical conversion of a metal oxide into coordination polymers and porous frameworks using liquid-assisted grinding (LAG). *CrystEngComm* **11**, 743–745 (2009).

80. Wang, K., Liu, C., Du, P., Zhang, H. L. & Gong, X. Efficient Perovskite Hybrid Solar Cells Through a Homogeneous High-Quality Organolead Iodide Layer. *Small* **11**, 3369–3376 (2015).

81. Tsvetkov, D. *et al.* Crucial Role of Water in the Mechanosynthesis of CsPbI3 and Other ABX3 Halides. *Chem. - A Eur. J.* **26**, 12549–12552 (2020).

82. Baikie, T. *et al.* Synthesis and crystal chemistry of the hybrid perovskite (CH 3NH3)PbI3 for solid-state sensitised solar cell applications. *J. Mater. Chem. A* **1**, 5628–5641 (2013).

83. Stoumpos, C. C., Malliakas, C. D. & Kanatzidis, M. G. Semiconducting tin and lead iodide perovskites with organic cations: Phase transitions, high mobilities, and near-infrared photoluminescent properties. *Inorg. Chem.* **52**, 9019–9038 (2013).

84. Arii, T. & Kishi, A. Thermal dehydration of cobalt and zinc formate dihydrates by controlled-rate thermogravimetry (CRTG) and simultaneous X-ray diffractometry-differential scanning calorimetry (XRD-DSC). *Thermochim. Acta* **325**, 157–165 (1999).

85. Lipton, A. S., Smith, M. D., Adams, R. D. & Ellis, P. D. Zn solid-state and single-crystal NMR spectroscopy and X-ray crystal structure of zinc formate dihydrate. *J. Am. Chem. Soc.* **124**, 410–414 (2002).

86. Varadwaj, P. R., Varadwaj, A. & Jin, B. Y. Ligand(s)-to-metal charge transfer as a factor controlling the equilibrium constants of late first-row transition metal complexes: Revealing the Irving-Williams thermodynamical series. *Phys. Chem. Chem. Phys.* **17**, 805–811 (2015).

87. Howard, J. L., Cao, Q. & Browne, D. L. Mechanochemistry as an emerging tool for molecular synthesis: What can it offer? *Chem. Sci.* **9**, 3080–3094 (2018).

88. Braga, D., Giaffreda, S. L., Grepioni, F. & Polito, M. Mechanochemical and solution preparation of the coordination polymers Ag[N(CH2CH2)3N]2[CH 3 COO]·5H2O and Zn[N(CH2CH 2)3N]Cl2. *CrystEngComm* **6**, 458–462 (2004).

89. Wang, P. *et al.* Mechanochemical interconversion between discrete complexes and coordination networks - Formal hydration/dehydration by LAG. *CrystEngComm* **14**, 1994–1997 (2012).

90. Shannon, R. D. Shannon-Prewitt Crystal Radii*. *Acta Cryst.* **A32**, 751 (1976).

91. Hadjiivanov, K. I. *et al.* Power of Infrared and Raman Spectroscopies to Characterize Metal-Organic Frameworks and Investigate Their Interaction with Guest Molecules. *Chem. Rev.* **121**, 1286–1424 (2021).

92. Seyferth, D. Infrared and raman spectra of inorganic and coordination compounds. *J. Organomet. Chem.* **156**, C47–C48 (1978).

93. Dualeh, A., Gao, P., Seok, S. Il, Nazeeruddin, M. K. & Grätzel, M. Thermal behavior of methylammonium lead-trihalide perovskite photovoltaic light harvesters. *Chem. Mater.* **26**, 6160–6164 (2014).

94. Xie, W. *et al.* Thermal degradation chemistry of alkyl quaternary ammonium Montmorillonite. *Chem. Mater.* **13**, 2979–2990 (2001).

95. Feriante, C. H. *et al.* Rapid Synthesis of High Surface Area Imine-Linked 2D Covalent Organic Frameworks by Avoiding Pore Collapse During Isolation. *Adv. Mater.* **32**, 1–5 (2020).

96. Pan, Q., Xiong, Y. A., Sha, T. T. & You, Y. M. Recent progress in the piezoelectricity of molecular ferroelectrics. *Mater. Chem. Front.* **5**, 44–59 (2021).

97. Damjanovic, D. Ferroelectric, dielectric and piezoelectric properties of ferroelectric thin films and ceramics. *Reports Prog. Phys.* **61**, 1267–1324 (1998).

98. Fu, D. *et al.* Supramolecular Bola-Like Ferroelectric : 4-Methoxyanilinium. **6**, 12780–12786 (2011).

99. Kieslich, G., Sun, S. & Cheetham, A. K. An extended Tolerance Factor approach for organic-inorganic perovskites. *Chem. Sci.* **6**, 3430–3433 (2015).

100. Kieslich, G. *et al.* Role of entropic effects in controlling the polymorphism in formate ABX3 metal-organic frameworks. *Chem. Commun.* **51**, 15538–15541 (2015).

101. Mączka, M. *et al.* Synthesis and order-disorder transition in a novel metal formate framework of [(CH3)2NH2]Na0.5Fe0.5(HCOO)3]. *Dalt. Trans.* **43**, 17075–17084 (2014).

102. Ciupa, A. *et al.* Temperature-dependent studies of [(CH3)2NH2][FeIIIMII(HCOO)6] frameworks (MII = Fe and Mg): Structural, magnetic, dielectric and phonon properties. *Dalt. Trans.* **44**, 8846–8854 (2015).

103. Sieradzki, A. *et al.* Dielectric relaxation behavior in antiferroelectric metal organic framework [(CH3)2NH2][FeIIIFeII(HCOO)6] single crystals. *Phys. Chem. Chem. Phys.* **18**, 8462–8467 (2016).

104. Zhao, J. P. *et al.* Magnetic behavior control in niccolite structural metal formate frameworks [NH2(CH3)2][FeIIIM II(HCOO)6] (M = Fe, Mn, and Co) by varying the divalent metal ions. *Inorg. Chem.* **49**, 10390–10399 (2010).

105. Hagen, K. S., Naik, S. G., Boi, H. H., Masello, A. & Christou, G. Intensely colored mixed-valence iron(II) iron(III) formate analogue of Prussian Blue exhibits Néel N-type ferrimagnetism. *J. Am. Chem. Soc.* **131**, 7516–7517 (2009).

106. Matsuo, M., Nakamori, Y., Orimo, S. I., Maekawa, H. & Takamura, H. Lithium superionic conduction in lithium borohydride accompanied by structural transition. *Appl. Phys. Lett.* **91**, 2–5 (2007).

107. Wen, Z., Xu, X. & Li, J. Preparation, microstructure and electrical properties of Li 1.4Al0.4Ti1.6(PO4)3 nanoceramics. *J. Electroceramics* **22**, 342–345

(2009).

108. Luo, R., Li, Q., Du, B., Zhou, S. & Chen, Y. Preparation and characterization of solid electrolyte doped with carbon nanotubes and its preliminary application in NO2 gas sensors. *Front. Mater.* **6**, 1–9 (2019).

109. Manuel Stephan, A. Nanocomposite polymer electrolytes for lithium batteries. *Recent Adv. Polym. Nanocomposites* **394**, 455–482 (2009).

110. Kreuer, K. D., Paddison, S. J., Spohr, E. & Schuster, M. Transport in proton conductors for fuel-cell applications: Simulations, elementary reactions, and phenomenology. *Chem. Rev.* **104**, 4637–4678 (2004).

111. Slade, R. C. T., Hardwick, A. & Dickens, P. G. Investigation of H+ motion in NAFION film by pulsed 1H NMR and A.C. conductivity measurements. *Solid State Ionics* **9**–**10**, 1093–1098 (1983).

112. Kreuer, K. D., Weppner, W. & Rabenau, A. Proton conduction in zeolites. *Mater. Res. Bull.* **17**, 501–509 (1982).

113. Kreuer, K. D. Aspects of the formation and mobility of protonic charge carriers.pdf. *Solid State Ionics* **125**, 285–302 (1999).

114. Wood, B. C. & Marzari, N. Proton dynamics in superprotonic CsHS O4. *Phys. Rev. B - Condens. Matter Mater. Phys.* **76**, 1–13 (2007).

115. Kanda Seiichi, Yamashita Kenichi, O. K. A Proton Conductive Coordination Polymer. I. [N,N′-Bis(2-hydroxyethyl)dithiooxamido]copper(II). 3296–3301 (1979).

116. Sadakiyo, M., Yamada, T. & Kitagawa, H. Hydrated Proton-Conductive Metal–Organic Frameworks. *Chempluschem* **81**, 691–701 (2016).

117. Röschenthaler, G. -V & Storzer, W. A Stable Tetraalkoxy(hydroxy)phosphorane and Phosphorane Oxide Anion by Hydrolysis of Tetraalkoxy(halogen)phosphoranes. *Angew. Chemie Int. Ed. English* **21**, 208–208 (1982).

118. Agmon, N. The Grotthuss mechanism. *Chem. Phys. Lett.* **244**, 456–462 (1995).

119. Ramaswamy, P., Wong, N. E. & Shimizu, G. K. H. MOFs as proton conductors-challenges and opportunities. *Chem. Soc. Rev.* **43**, 5913–5932 (2014).

120. Yamada, T., Sadakiyo, M. & Kitagawa, H. High proton conductivity of one-dimensional ferrous oxalate dihydrate. *J. Am. Chem. Soc.* **131**, 3144–3145 (2009).

121. Sadakiyo, M., Yamada, T. & Kitagawa, H. Rational designs for highly proton-conductive metal-organic frameworks. *J. Am. Chem. Soc.* **131**, 9906–9907 (2009).

122. Nagarkar, S. S., Unni, S. M., Sharma, A., Kurungot, S. & Ghosh, S. K. Two-in-one: Inherent anhydrous and water-assisted high proton conduction in a 3D metal-organic framework. *Angew. Chemie - Int. Ed.* **53**, 2638–2642 (2014).

123. Panda, T., Kundu, T. & Banerjee, R. Structural isomerism leading to variable proton conductivity in indium(iii) isophthalic acid based frameworks. *Chem. Commun.* **49**, 6197–6199 (2013).

124. Okawa, H. *et al.* Proton-conductive magnetic metal-organic frameworks, {NR 3(CH2COOH)}[MaIIMbIII(ox)3]: Effect of carboxyl residue upon proton conduction. *J. Am. Chem. Soc.* **135**, 2256–2262 (2013).

125. Shigematsu, A., Yamada, T. & Kitagawa, H. Wide control of proton conductivity in porous coordination polymers. *J. Am. Chem. Soc.* **133**, 2034–2036 (2011).

126. Lim, D. W., Sadakiyo, M. & Kitagawa, H. Proton transfer in hydrogen-bonded degenerate systems of water and ammonia in metal-organic frameworks. *Chem. Sci.* **10**, 16–33 (2019).

127. Marvel, C. S. & Caesar, P. D. The Reduction of Sulfonyl Chlorides to Mercaptans with Lithium Aluminum Hydride. *J. Am. Chem. Soc.* **72**, 1033 (1950).

128. Uribe, F. A. & Bard, A. J. Electrochemistry in Liquid Ammonia. 5. Electroreduction of Oxygen. *Inorg. Chem.* **21**, 3160–3163 (1982).

129. Hoekstra, H. R. & Katz, J. J. The Preparation and Properties of the Group IV-B Metal Borohydrides. *J. Am. Chem. Soc.* **71**, 2488–2492 (1949).

130. Krishnamurthy, M., De Gouw, J. A., Ding, L. N., Bierbaum, V. M. & Leone, S. R. Mobility and formation kinetics of NH4+(NH3)n cluster ions (n=0-3) in helium and helium/ammonia mixtures. *J. Chem. Phys.* **106**, 530–538 (1997).

131. Pardo, E. *et al.* High proton conduction in a chiral ferromagnetic metal-organic quartz-like framework. *J. Am. Chem. Soc.* **133**, 15328–15331 (2011).

132. Paredes-García, V. *et al.* Crystal structure and magnetic properties of a new chiral manganese(II) three-dimensional framework: Na3[Mn3(HCOO)9]. *Inorg. Chem.* **48**, 4737–4742 (2009).

133. Golobič, A., Malekovič, M. & Šegedin, P. Catena-Poly[disodium [[diformato-tricopper(II)]-di-μ3- formato-tetra-μ2-formato]]: A new mode of bridging between binuclear and mononuclear formate-copper(II) units. *Acta Crystallogr. Sect. C Cryst. Struct. Commun.* **62**, 102–104 (2006).

134. Gemmi, M. & Lanza, A. E. 3D electron diffraction techniques. *Acta Crystallogr. Sect. B Struct. Sci. Cryst. Eng. Mater.* **75**, 495–504 (2019).

135. Mugnaioli, E. *et al.* Ab initio structure determination of vaterite by automated electron diffraction. *Angew. Chemie - Int. Ed.* **51**, 7041–7045 (2012).

136. Elettra website.pdf.

137. Petříček, V., Dušek, M. & Plášil, J. Crystallographic computing system Jana2006: Solution and refinement of twinned structures. *Zeitschrift fur Krist. - Cryst. Mater.* **231**, 583–599 (2016).

ACKNOWLEDGEMENTS E RINGRAZIAMENTI

At the conclusion of this work, I would like to thank the people that helped me during these three years.

First of all, I would like to thank my supervisors, Prof. Lara Righi and Dr. Fabio Orlandi, who helped me and followed my work during the past three years and for introducing me into the word of the inorganic and hybrid materials and, most importantly, to the world of the research.

I also want to thank the entire research group of Prof. Mauro Gemmi of the IIT of Pisa, in particular Andrea Griesi and Dr. Arianna Lanza, who performed the high resolution PXRD diffraction and TEM analysis. Moreover, their support has been fundamental during these three years.

For what concerns the characterization of the materials, I would like to express my gratitude to Prof. Massimo Solzi and Dr. Francesco Cugini of the Physical Department of the University of Parma who performed both the magnetic and the ferroelectric measurements together with Dr. Davide Delmonte of CNR IMEM of Parma, who also contributed with his help for the measurements.

I also would like to thank the entire research group of Prof. Mauro Riccò from the Physical Department of University of Parma who gave us the possibility to collaborate. In particular I thank Dr. Silvio Scaravonati for the time he spent doing the ionic conduction measurements and the precious hints he gave me. Moreover, I thank all the other members of the research group: Prof. Daniele Pontiroli, Dr. Giacomo Magnani, Michele Sidoli and Alberto Morenghi, for the hospitality in their laboratory during the measurements.

Moreover, my thanks go to Prof. Danilo Bersani of the Physical Department of The University of Parma for the Raman measurements, and Dr. Davide Calestani of the CNR IMEM of Parma, for the SEM analysis and for the thermal treatment performed on ceramics materials. I also would like to thank Prof. Alessio Bosio for the availability demonstrated for the metallization of the sample.

Last, but not least, I would like to thank Roberta Magnani for having performed the thermal analysis on my sample.